Università degli Studi di Palermo

AREA RICERCA E TRASFERIMENTO TECNOLOGICO
SETTORE DOTTORATI E CONTRATTI PER LA RICERCA
U. O. DOTTORATI DI RICERCA

PhD Mechanical, Manufacturing, Management and Aerospace Innovation (M3AI)
Department of Engineering (DI)
ING-IND/34

PATIENT-SPECIFIC SIMULATION AND MODEL CREDIBILITY FOR TRANSCATHETER AORTIC VALVE IMPLANTATION

IL DOTTORE

ROBERTA SCUOPPO

IL COORDINATORE

GIOVANNA LO NIGRO

IL TUTOR

SALVATORE PASTA

CICLO XXXVIII

ANNO CONSEGUIMENTO TITOLO 2024 - 2025

Abstract

Transcatheter aortic valve implantation, known as TAVI, is a minimally invasive procedure for the treatment of severe aortic stenosis. Its expanding use in patients with complex anatomies and longer life expectancy underscores the need for reliable tools capable of predicting device performance and procedural outcomes. This thesis develops a comprehensive patient-specific computational framework for the analysis of TAVI, integrating anatomical variability, device mechanics, and blood flow dynamics within a unified modeling approach. Statistical shape modeling was employed to characterize interpatient anatomical variability of the aortic root and to generate virtual cohort representative of real clinical populations. Shape-derived features were further combined with machine learning techniques to predict functional indicators and support prosthesis sizing.

High-fidelity finite element analysis was implemented to reproduce TAVI deployment using clinically accurate device models, while post-implantation hemodynamics were evaluated through Smoothed particle hydrodynamics. Model credibility was addressed through a rigorous Verification, Validation, and Uncertainty Quantification strategy in accordance with the ASME V&V40 standard. The framework was subsequently applied to investigate redo-TAVI interventions, enabling parametric assessment of implantation depth, valve size, and device–device interactions, with particular attention to coronary flow impairment. Finally, a novel transcatheter leaflet resection approach prior to redo-TAVI was explored in silico, demonstrating its potential to enhance valve expansion and improve hemodynamic performance.

Overall, this work establishes a validated in-silico platform that supports device design, procedural optimization, and the development of predictive tools for personalized TAVI planning.

Acknowledgments

This project has received funding from the European Union's Horizon 2020 research and innovation program under grant agreement No 101017523.

Summary

Abbreviations

AS – Aortic Stenosis
AVA – Aortic Valve Area
ASME – American Society of Mechanical Engineers
BAV – Bicuspid Aortic Valve
BSA – Body Surface Area
CAD – Computer-Aided Design
CDF – Cumulative Distribution Function
CFD – Computational Fluid Dynamics
CMR – Cardiac Magnetic Resonance
CoU – Context of Use
CT – Computed Tomography
DD – Device Diameter
DOF – Degrees of Freedom
ECG – Electrocardiogram
EOA – Effective Orifice Area
FDA – Food and Drug Administration
FEA – Finite Element Analysis
FSI – Fluid–Structure Interaction
GPR – Gaussian Process Regression
HU – Hounsfield Unit
ICP – Iterative Closest Point
IoU – Intersection over Union
ISO – International Organization for Standardization
KNN – k-Nearest Neighbors
LCA – Left Coronary Artery
LHS – Latin Hypercube Sampling
LOO – Leave-One-Out (cross-validation)
LVOT – Left Ventricular Outflow Tract
ML – Machine Learning
MLP – Multilayer Perceptron
MRE – Mean Relative Error
MCS – Monte Carlo Simulation
PCA – Principal Component Analysis
PET – Polyethylene Terephthalate
PPG / AS-PPG – Peak Pressure Gradient / Aortic Stenosis Peak Pressure Gradient
RE – Relative Error
RCA – Right Coronary Artery
RMSE – Root Mean Square Error
ROI – Region of Interest
R-R interval – Cardiac cycle interval between two R waves
S3 – SAPIEN 3 Transcatheter Heart Valve
SPH – Smoothed Particle Hydrodynamics

SSM – Statistical Shape Model
STJ – Sinotubular Junction
SV – Stroke Volume
SVM – Support Vector Machine
TAVI – Transcatheter Aortic Valve Implantation
TEI – Total Effect Index
THV – Transcatheter Heart Valve
TPG – Transvalvular Pressure Gradient
UQ – Uncertainty Quantification
VTC – Valve-to-Coronary distance
VVUQ – Verification, Validation and Uncertainty Quantification

Chapter 1

1. Introduction

Aortic stenosis (AS) represents the most common valvular disease in Western populations, with its prevalence increasing with age, from approximately 0.2% among individuals aged 50 - 59 years to nearly 10% in those aged 80 - 89 years [1]. This condition is associated with considerable morbidity and mortality, as well as a growing economic impact on healthcare systems due to the increasing number of patients requiring valve intervention. The disease is characterized by progressive calcification and stiffening of the aortic valve leaflets, which leads to narrowing of the valve orifice, increased left ventricular afterload, and, if untreated, eventual heart failure and death.

For decades, surgical aortic valve replacement (SAVR) represented the gold standard for treatment, providing durable hemodynamic correction but at the cost of considerable surgical trauma and perioperative risk. The advent of transcatheter aortic valve implantation (TAVI) has transformed the therapeutic landscape, offering a minimally invasive alternative for elderly and high-risk patients. Over the last two decades, continuous advancements in device design and procedural technique have progressively expanded TAVI indications to intermediate- and even low-risk populations.

Conventional pre-procedural planning, based mainly on two-dimensional imaging and linear anatomical measurements, cannot fully capture the three-dimensional geometry and biomechanical heterogeneity of the aortic root and valve structures. As a result, the ability to predict post-procedural complications, such as paravalvular leakage, coronary obstruction, conduction abnormalities, or suboptimal device expansion, remains limited.

In this context, computational modeling provides powerful tools to complement clinical and experimental research by simulating the mechanical and hemodynamic behavior of TAVI systems in realistic conditions [2-4]. Through finite element analysis (FEA), it is possible to reproduce device deployment within patient-specific anatomies, evaluate frame expansion, stress distribution, and tissue interaction, and identify configurations associated with procedural risk. Computational fluid dynamics (CFD), and more broadly fluid–structure interaction (FSI) simulations, enable the analysis of post-implantation blood flow, quantifying effective orifice area, pressure gradients, and potential flow disturbances that may affect valve performance or durability.

The research presented in this thesis aims to develop and validate an integrated computational modeling platform for TAVI and redo-TAVI procedures, encompassing structural, hemodynamic, and credibility assessment components. The thesis specifically aims to:

- Develop and apply FEA to simulate the deployment of transcatheter valves in both native and previously implanted (redo-TAVI) configurations, quantifying device expansion, stress distribution, and mechanical interaction with the aortic root.
- Employ CFD with smoothed particle hydrodynamics (SPH) approach to evaluate post-procedural blood flow and hemodynamic performance, including effective orifice area, transvalvular gradients, and coronary perfusion.
- Establish a framework for model credibility based on Verification, Validation, and Uncertainty Quantification (VVUQ) in accordance with the ASME V&V40 standard, ensuring that computational predictions are accurate, reproducible, and aligned with their intended clinical context of use.

Together, these activities contribute to the creation of a credible, patient-specific simulation environment for TAVI, enabling predictive analyses of procedural outcomes, supporting device optimization, and advancing the integration of computational modeling into the clinical decision-making process.

Chapter 2

2. Clinical context

2.1 Anatomy and physiology of aortic valve

The human heart is a muscular organ responsible for ensuring continuous circulation of blood throughout the body. Its rhythmic contractions generate pressure differences that drive blood flow, but the unidirectionality of this flow is guaranteed by the cardiac valves. Valves act as mechanical gates that open and close in synchrony with the cardiac cycle, preventing retrograde flow and optimizing cardiac efficiency. Their structural integrity and coordinated function are essential for maintaining hemodynamic stability.

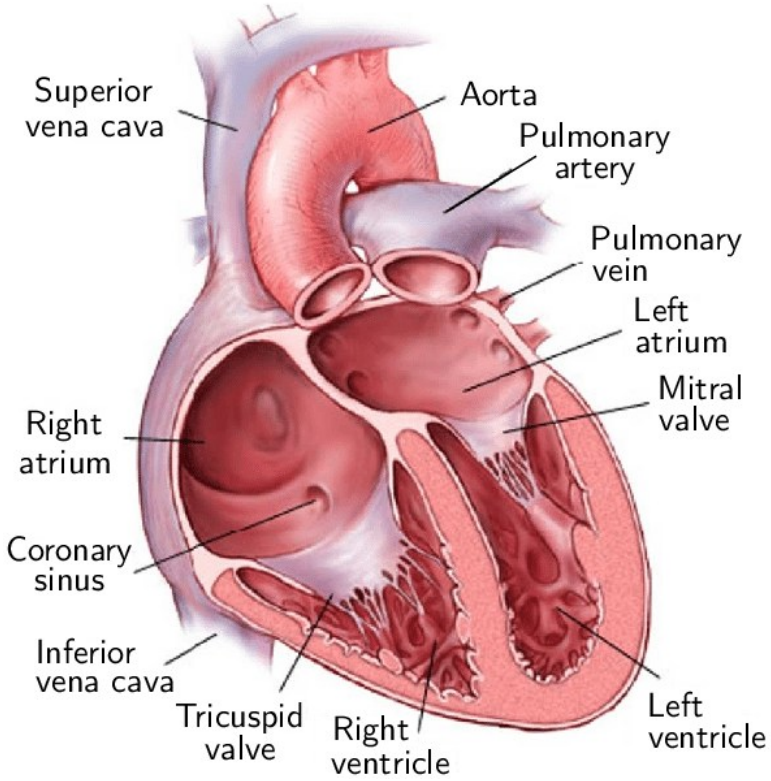

***Figure 2.1**: Anatomy of the Heart. With permission of Hintermüller [5].*

The heart contains four valves: the atrioventricular valves (mitral and tricuspid) and the semilunar valves (aortic and pulmonary).

- The *mitral valve* regulates blood flow between the left atrium and left ventricle.
- The *tricuspid valve* serves a similar function between the right atrium and right ventricle.

- The *pulmonary valve* controls ejection of blood from the right ventricle to the pulmonary artery.
- The *aortic valve* ensures proper outflow from the left ventricle to the systemic circulation.

Each valve's design reflects its specific functional demands, with thin and flexible leaflets supported by fibrous structures that endure millions of openings and closing cycles.

The aortic valve is a tricuspid semilunar valve located at the junction between the left ventricle and the ascending aorta. Structurally, it comprises three cusps, the right, left, and non-coronary cusps, anchored to the fibrous annulus and supported by the sinuses of Valsalva, small outpouchings of the aortic root that extend between the valve leaflets and the sinotubular junction (STJ). These sinuses play a fundamental role in the valve's dynamics, generating vortices during systole that assist leaflet opening and preventing leaflet adhesion to the aortic wall during diastole. The region extending from the annulus to the STJ constitutes the aortic root, which acts as both a structural and functional interface between the left ventricle and the ascending aorta.

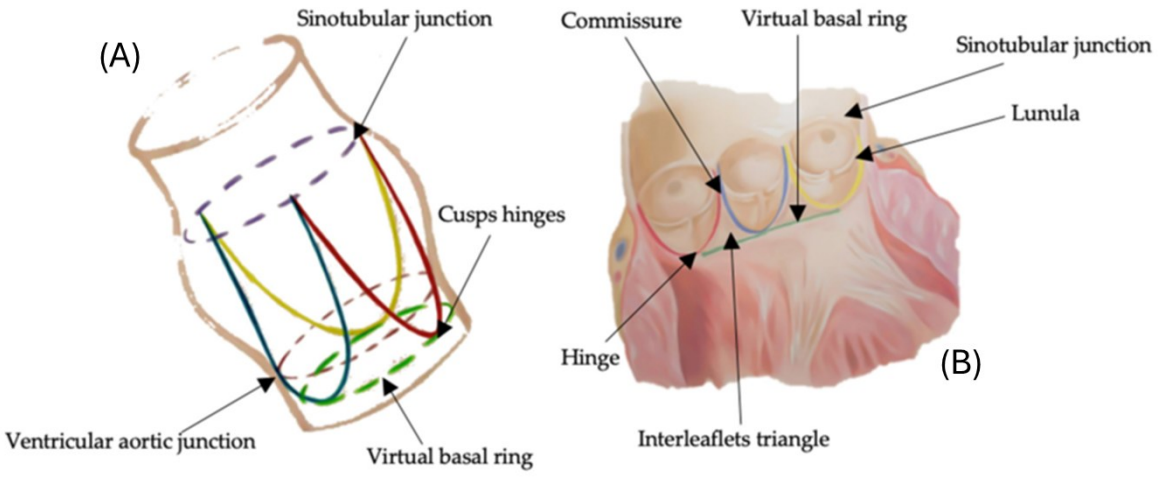

***Figure 2.2**: (A) Schematic representation of aortic valve anatomy. The dotted blue line indicates the sinotubular junction, the dotted green one depicts the virtual basal ring, and the dotted red one shows the ventricular aortic junction. (B) Graphic representation of an opened aortic root with its anatomical components. With permission from Circhetta et al.*[6].

Histologically, the valve leaflets consist of three layers: the fibrosa, the spongiosa, and the ventricularis. The fibrosa, located on the aortic side, is a dense collagenous layer that provides tensile strength. The spongiosa, found in the central portion, contains proteoglycans and glycosaminoglycans that confer flexibility and shock absorption. The ventricularis, on the ventricular side, contains elastin fibers that contribute to leaflet recoil and motion. This trilaminar configuration allows the valve to withstand the repetitive hemodynamic loads of the cardiac cycle, estimated at nearly 100,000 opening and closing cycles per day.

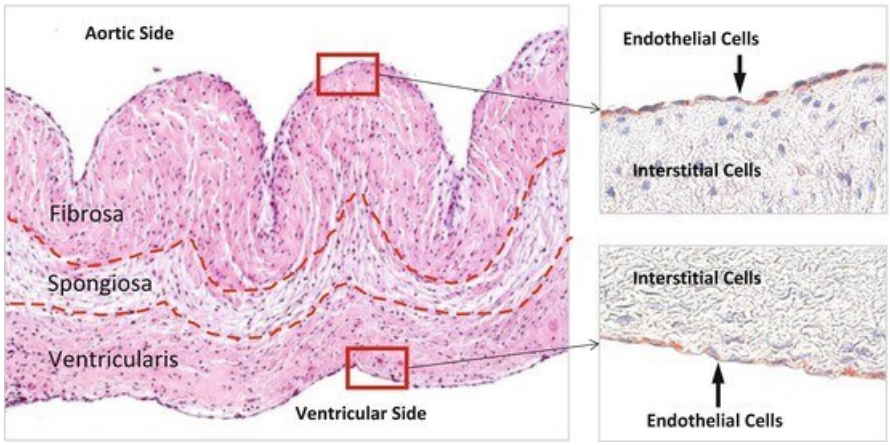

***Figure 2.3**: Histologic section of an aortic valve leaflet. With permission from Zhong et al.*[7].

During systole, left ventricular pressure exceeds that of the aorta, forcing the valve leaflets to open and allowing ejection of blood into the systemic circulation. The cusps are displaced toward the aortic wall, forming a smooth, central laminar jet through the ascending aorta. During diastole, the pressure gradient reverses, and blood partially refluxes into the sinuses of Valsalva, generating vortices that facilitate leaflet closure. The lunulae, or coaptation zones, overlap slightly to ensure a tight seal and prevent regurgitation. Under physiological conditions, transvalvular pressure gradients remain below 10 mmHg, ensuring efficient flow with minimal energy loss. Any alteration in cusp mobility, annular geometry, or root compliance can disrupt these flow dynamics, leading to increased gradients and mechanical stress on the valve.

While the normal aortic valve has three leaflets, congenital malformations can lead to variants such as the bicuspid aortic valve (BAV), present in approximately 1–2% of the general population. In this condition, two of the cusps are fused, resulting in asymmetric leaflet configuration and altered flow patterns.

2.2 Aortic Stenosis: Pathophysiology and Diagnosis

AS is the most common valvular disease in industrialized countries and the third most frequent cardiovascular disorder after hypertension and coronary artery disease. The condition is typically caused by degenerative calcification of a tricuspid valve. The degenerative process involves chronic inflammation, lipid deposition, and active calcification of the leaflets, leading to their thickening, stiffening, and restricted mobility. Risk factors for calcific AS mirror those for atherosclerosis, including hypertension, diabetes mellitus, smoking, and elevated lipoprotein levels [8].

Over time, obstruction of the left ventricular outflow tract increases systolic pressure load on the ventricle, triggering concentric hypertrophy as a compensatory mechanism to maintain wall stress and cardiac output. Although initially beneficial, this adaptation reduces ventricular compliance, leading to elevated diastolic filling pressures and eventual heart failure [9].

Clinically, patients with severe AS often present with the classical triad of angina, syncope, and dyspnea, reflecting impaired coronary perfusion, fixed cardiac output, and elevated pulmonary pressures, respectively. Once symptoms develop, prognosis worsens dramatically, with an average survival of only two to three years without valve replacement. Severe AS is defined by an aortic valve area < 1.0 cm², a mean gradient > 40 mmHg, or a peak velocity > 4.0 m/s, as established by echocardiographic criteria [10].

Diagnosis relies primarily on transthoracic echocardiography, which allows direct visualization of valve morphology and quantification of transvalvular flow. Doppler echocardiography measures jet velocity and calculates gradients and valve area, providing the basis for grading severity. Additional imaging modalities such as computed tomography (CT) and cardiac magnetic resonance (CMR) offer valuable information about valve calcification and aortic root geometry [11].

2.3 Transcatheter Aortic Valve Implantation

For decades, the gold standard treatment for severe AS has been *surgical aortic valve replacement (SAVR)*. This open-heart procedure requires a median sternotomy, cardiopulmonary bypass, and excision of the diseased valve, followed by implantation of a mechanical or bioprosthetic valve. SAVR has demonstrated excellent long-term durability,

especially with mechanical prostheses, but it is associated with substantial surgical trauma, prolonged recovery, and risks of perioperative complications. Elderly patients or individuals with significant comorbidities may face prohibitive surgical risks, limiting the applicability of SAVR in these populations. In the context of SAVR, several types of prosthetic valves are available, broadly classified into mechanical and biological valves. Mechanical valves, typically composed of durable materials such as pyrolytic carbon, offer excellent long-term durability but require lifelong anticoagulation therapy. In contrast, biological valves, derived from porcine or bovine pericardial tissues, provide more physiological flow characteristics and reduce anticoagulation requirements (Figure 2.4).

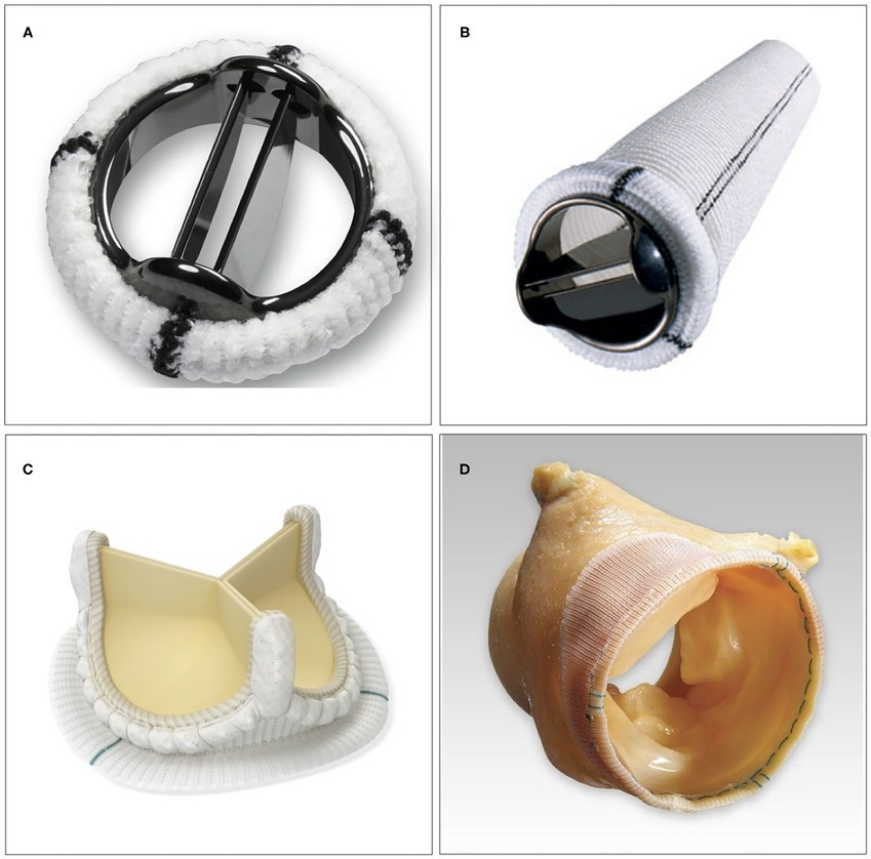

Figure 2.4*: Examples of surgical aortic valve interventions. (A) Bi-leaflet mechanical prosthesis. (B) Mechanical composite graft used in aortic root replacement. (C) Stented bioprosthetic valve (AvalusTM, Medtronic, MN, USA). (D) Stentless bioprosthetic valve (FreestyleTM, Medtronic, MN, USA). With permission from De Backer et al. [12].*

Introduced in 2002, *transcatheter aortic valve implantation (TAVI)* represented a paradigm shift in the management of aortic stenosis [13]. TAVI is a catheter-based, minimally invasive alternative to surgical aortic valve replacement. Since its first successful case in 2002, TAVI has rapidly evolved into a mainstream therapy for severe aortic stenosis, initially targeting

patients deemed inoperable or at high surgical risk, and now progressively offered to intermediate- and low-risk populations. Its principle is straightforward yet revolutionary: instead of removing the diseased valve, a bioprosthetic valve is deployed within the calcified native valve, restoring forward flow while minimizing the trauma associated with open-heart surgery. Initially reserved for patients with inoperable or high surgical risk, TAVI has progressively expanded its indications to intermediate- and even low-risk patients, supported by robust evidence from randomized controlled trials. TAVI offers multiple advantages, especially for elderly and fragile patients:

- Reduced procedural invasiveness with no need for sternotomy or extracorporeal circulation.
- Lower rates of perioperative mortality in high-risk cohorts.
- Faster recovery times and improved early quality of life.
- Broader applicability in patients previously excluded from surgical intervention.
- Increasing evidence of comparable or superior outcomes to SAVR in selected intermediate- and low-risk patients.

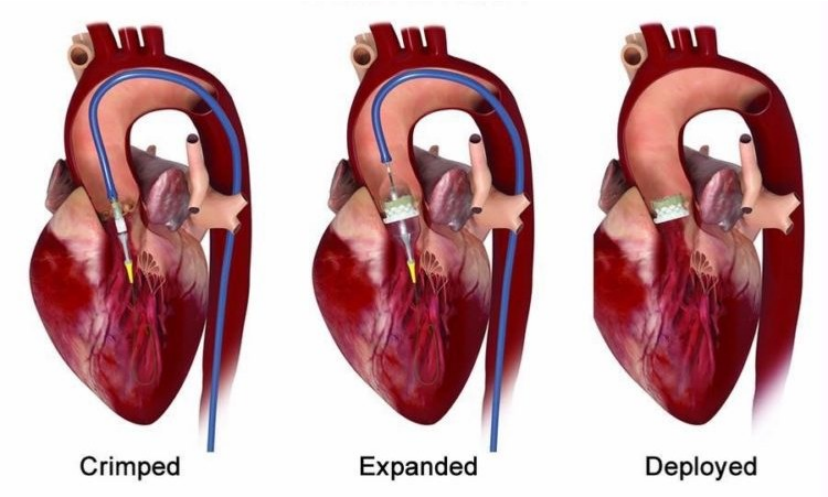

Figure 2.5 *Key steps of TAVI procedure.*

In summary, while SAVR remains an established and durable treatment, TAVI has emerged as a transformative alternative that expands therapeutic options for patients across risk categories. Its continuous evolution in device design, patient selection, and procedural techniques promises to further consolidate its role in the treatment of aortic stenosis.

Transcatheter heart valves (THVs) share a common configuration designed to mimic the function of the native aortic valve while being deliverable through a catheter. They consist of three main components:

- A *metallic stent frame* (typically cobalt–chromium or nitinol) that anchors the device within the calcified native valve.
- *Bioprosthetic leaflets*, usually made from bovine or porcine pericardium, mounted inside the frame to ensure unidirectional blood flow.
- An *outer skirt*, made of fabric or polymer, which minimizes paravalvular leakage by filling the gaps between the stent and the native anatomy.

Despite this common design, current THVs differ significantly in their expansion mechanism, frame design, and hemodynamic profile.

THVs can be broadly categorized into balloon-expandable and self-expanding systems, which differ in both their deployment mechanisms and their biomechanical interaction with the aortic root. Balloon-expandable valves rely on balloon inflation to achieve rapid and complete stent expansion. This design provides high radial force and immediate fixation within the calcified annulus, enabling precise positioning and predictable geometry after release. In contrast, self-expanding valves use a nitinol frame that deploys gradually in response to temperature and mechanical release. The self-expanding property offers continuous outward pressure, which allows the device to adapt to variations in annular shape and size over time. Consequently, balloon-expandable valves generally achieve superior circularity and anchoring stability, whereas self-expanding valves demonstrate greater anatomical adaptability and may yield larger effective orifice areas owing to their supra-annular leaflet positioning.

Clinically, several comparative studies have demonstrated differences in procedural and long-term outcomes between the two valve families. Mack et al. reported that balloon-expandable valves were associated with lower rates of paravalvular leak and fewer pacemaker implantations, while self-expanding valves achieved lower residual gradients and larger effective orifice areas at follow-up [14]. These differences reflect the distinct mechanical behavior of each design and underscore the importance of tailoring valve selection to patient-specific anatomical and clinical characteristics.

Among the wide range of transcatheter valve systems currently available, two devices were selected as the primary focus of this doctoral research: the Edwards SAPIEN 3 and the Medtronic Evolut PRO. Their contrasting structural configurations and deployment behaviors provide an ideal framework for investigating the mechanical and hemodynamic performance of TAVI through computational modeling.

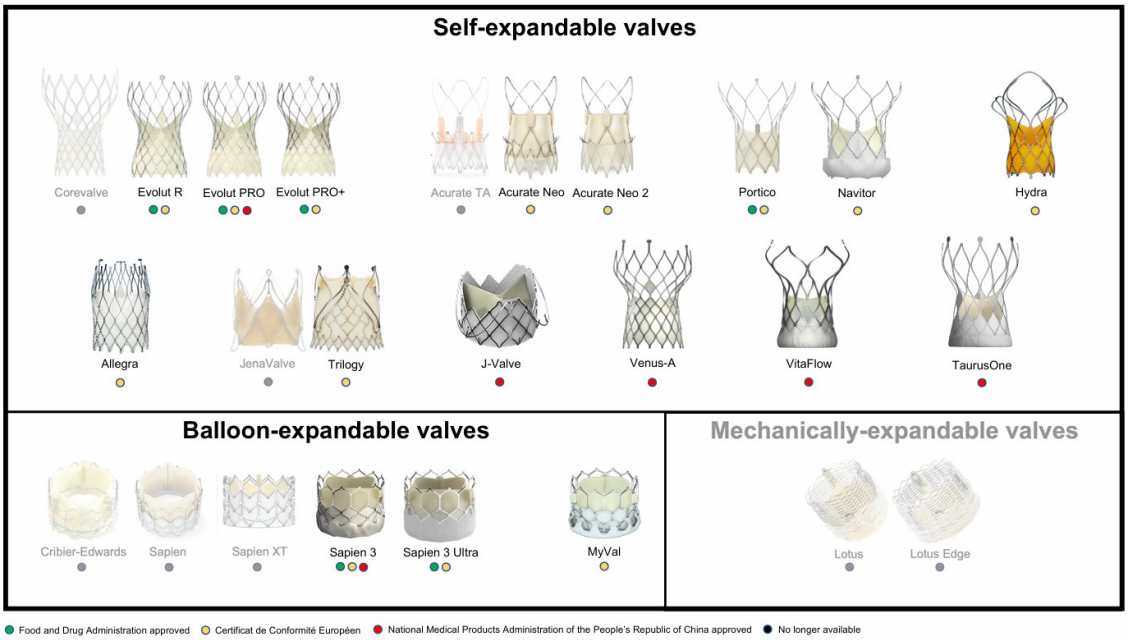

Figure 2.6 *Commercially available THVs. With permission from Vinayak et al. [15].*

The Edwards SAPIEN 3 (S3) is the most widely used balloon-expandable valve and is characterized by a cobalt–chromium alloy frame combined with bovine pericardial leaflets and an external polyethylene terephthalate (PET) skirt designed to minimize paravalvular leakage. Balloon inflation ensures high radial force and accurate positioning, leading to excellent circularity and anchoring stability within the aortic annulus. These properties make the SAPIEN 3 particularly suitable for patients with calcified or regular annuli, where complete circular expansion can be achieved. However, its rigid deployment mechanism increases the risk of annular rupture in severely calcified anatomies and offers limited adaptability to asymmetric or elliptical geometries [16].

The Medtronic Evolut PRO, on the other hand, exemplifies the self-expanding valve category. It is constructed from a nitinol frame that allows gradual, temperature-dependent expansion and provides continuous outward force after implantation. The porcine pericardial leaflets are mounted in a supra-annular position, enhancing the effective orifice area and reducing post-procedural pressure gradients. The Evolut PRO recapturable and

repositionable delivery system offers greater procedural flexibility and safety, particularly in anatomically complex cases. Nevertheless, its sustained contact with the interventricular septum and conduction pathways has been linked to higher rates of conduction abnormalities and permanent pacemaker implantation [17].

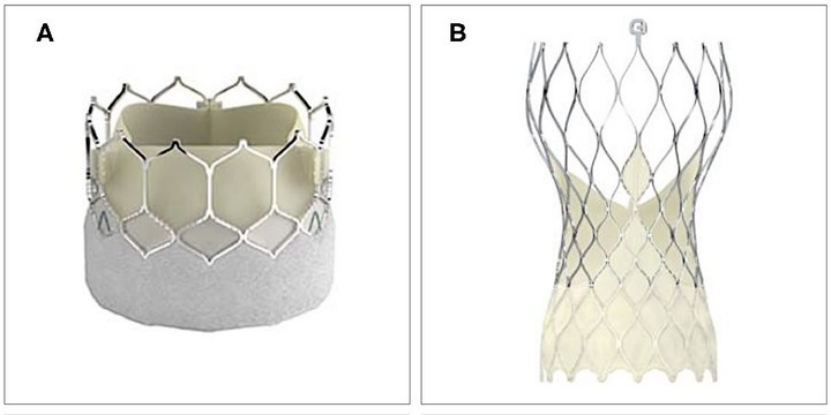

Figure 2.7: *THVs valve; (A) SAPIEN 3 (Ultra), (B) Evolut R/PRO. With permission from De Backer et al. [12].*

From a regulatory standpoint the U.S. Food and Drug Administration (FDA) emphasizes that valve selection should be patient-specific, guided by anatomical, clinical, and procedural considerations [18]. Regulatory guidance recommends that valve choice be made within a multidisciplinary Heart Team framework, balancing the benefits of radial force and circularity in balloon-expandable designs with the adaptability and lower gradients offered by self-expanding systems.

Chapter 3

3. Background

In the context of TAVI computational models have shown potential to predict the deployment of self-expandable and balloon-expandable THVs to enhance patient outcomes and inform device design [19-24]. These methods allow researchers and clinicians to simulate device deployment, blood flow, and valve–anatomy interactions in a controlled and reproducible way, generating insights that complement both experimental testing and clinical trials.

3.1 Methods for computational modeling

FEA is used to model the mechanical behavior of devices and tissues under stress. In TAVI, FEA can simulate stent expansion within a calcified aortic root, predict stresses on leaflets, and evaluate the risk of annular rupture or paravalvular leakage. Balloon-expandable and self-expanding valve frames can be virtually deployed in patient-specific anatomies to assess anchoring stability, radial forces, and potential device mismatch. FEA is particularly valuable for optimizing device design, reducing the risk of complications, and exploring scenarios that would be difficult to test clinically [3, 19-21, 25-27].

CFD focuses on blood flow patterns across the valve and in the ascending aorta. By solving the Navier–Stokes equations in three dimensions, CFD models capture velocity fields, shear stresses, and turbulence caused by valve obstruction or improper deployment. In the context of TAVI, CFD can quantify post-procedural hemodynamics, evaluate residual gradients, and assess risks of complications such as leaflet thrombosis or coronary obstruction [28]. These models help explain how valve geometry and patient anatomy influence functional outcomes [29-31]. FSI represents the integration of FEA and CFD, allowing the simulation of both solid mechanics and fluid dynamics simultaneously. In TAVI, FSI can reproduce the interaction between the moving valve leaflets and pulsatile blood flow, capturing realistic pressure–volume relationships and leaflet kinematics [30, 32, 33]. FSI is also applied to evaluate long-term durability by estimating repetitive leaflet stresses and flow-induced fatigue. Although computationally demanding, FSI provides the most comprehensive representation of the TAVI system and its physiological environment [32, 34-38]. Catalano *et al.* introduced a fully coupled FSI framework that integrates SPH with nonlinear finite

element models to simulate realistic TAVI deployment. This methodology improves the understanding of post-TAVI hemodynamics and supports the development of a validate in silico platforms for device testing [39].

3.2 Patient-Specific Anatomical Features

In the context of TAVI inter-patient variability in aortic root geometry, annular size, and calcification pattern plays a decisive role in determining procedural success and post-implantation hemodynamics. The accurate representation of this variability through patient-specific modeling is therefore essential to understand how anatomical differences influence valve expansion, sealing, and pressure gradients.

SSM provides a quantitative framework to capture and reproduce such variability across populations. Starting from ECG-gated CT imaging, the aortic root and calcifications are segmented, aligned, and analyzed using Principal Component Analysis (PCA), which decomposes the anatomy into a mean shape and principal modes of variation. By varying these modes within physiological ranges, virtual anatomies can be generated that reflect realistic morphological diversity. These virtual cohorts can then serve as the foundation for predictive modeling, where anatomical descriptors derived from SSM are correlated with functional parameters such as transvalvular pressure gradient or device expansion indices [40].

When combined with machine learning (ML) approaches, shape-derived features can be used to develop data-driven predictive models capable of estimating hemodynamic outcomes or suggesting optimal valve sizing based solely on patient morphology.

3.3 Model credibility and regulatory standards

As computational models become increasingly central to cardiovascular research and medical device evaluation, establishing their credibility is essential. Unlike experimental studies, where results are directly observable, simulations rely on assumptions, numerical methods, and input data that must be rigorously verified and validated before they can inform clinical or regulatory decisions [41, 42].

- *Verification* ensures that the computational model has been implemented correctly and that the equations are solved accurately.

- *Validation* assesses whether the model reliably represents the physical or clinical system of interest, typically through comparison with experimental or clinical data.

The American Society of Mechanical Engineers (ASME) has developed the V&V40 standard specifically for computational modeling in medical device applications. This framework introduces a *risk-informed approach* to model credibility, meaning that the level of evidence required to support a model depends on its intended *context of use* and the potential consequences of incorrect predictions.

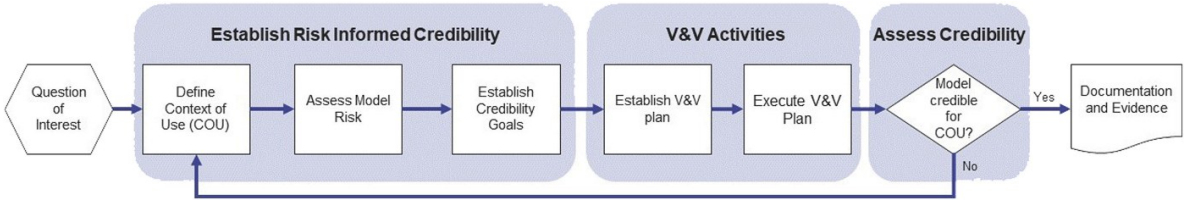

***Figure 3.1**: Framework of ASME V&V40.*

Key components of the framework include:

1. **Defining the context of use** – clarifying how the model will be applied (e.g., device design optimization, pre-procedural planning, regulatory submission).
2. **Identifying sources of uncertainty** – input variability, model simplifications, or numerical errors.
3. **Quantifying and propagating uncertainty** – using probabilistic methods or sensitivity analyses.
4. **Assessing model credibility** – balancing the risks of relying on the model against the strength of the available verification, validation, and uncertainty quantification evidence.

For TAVI, applying ASME V&V40 ensures that computational predictions, whether about valve deployment mechanics, flow dynamics, or virtual cohort outcomes, are robust, transparent, and reproducible [39, 43]. This is particularly important as *in silico* trials begin to complement clinical evidence in regulatory pathways. Demonstrating model credibility not only strengthens scientific conclusions but also supports the safe translation of computational methods into real - world clinical and industrial settings [44, 45].

Chapter 4

4. Generation of Patient-Specific models

Patient variability, defined as the natural anatomical, physiological, and pathological heterogeneity observed across individuals, represents one of the primary challenges in the development of reliable computational models for structural heart interventions. In the context of aortic stenosis and TAVI, variability manifests in multiple dimensions, including differences in aortic root geometry, leaflet morphology, calcification burden, ventricular function, and hemodynamic conditions. These inter-patient differences directly influence device behavior, procedural outcomes, and the risk of complications.

As TAVI expands into younger, lower-risk, and more heterogeneous populations, capturing this variability becomes essential for generating accurate predictions of device performance. Computational models that neglect or oversimplify patient variability risk losing clinical relevance, particularly in borderline anatomies or complex redo-TAVI scenarios.

Patient-specific modeling has emerged as a cornerstone of contemporary in silico cardiovascular research. Patient-specific models allow the reconstruction of anatomical features directly from medical images, thereby preserving the unique geometric characteristics that determine device - human host interactions.

In the TAVI context, accurate patient-specific models enable:

- Realistic simulation of device deployment and assessment of expansion quality
- Prediction of hemodynamics, including pressure gradients and coronary perfusion
- Evaluation of complications, such as paravalvular leakage or coronary obstruction
- Treatment planning, including device sizing and identification of high-risk anatomies

However, the fidelity of a patient-specific computational model depends critically on the accuracy of the segmentation process, which defines the boundaries of the anatomy used as the numerical domain.

Because the success of TAVI depends strongly on the geometric and mechanical interaction between the device and the patient's anatomy, the computational domain must reproduce as

faithfully as possible the structural complexity of the aortic root, the diseased valve leaflets, and the calcific deposits.

4.1 Patient study group and imaging

A prospective, single-center cohort of patients with severe symptomatic aortic stenosis referred for TAVI at IRCCS–ISMETT was selected. To obtain a simulation-ready dataset representative of the anatomical variability encountered clinically, the population was balanced across S3 device sizes (23 mm and 26 mm; the 29 mm size was excluded due to limited use) and encompassed a broad range of annular diameters, sinus morphologies, and calcification patterns.

All patients underwent standardized transthoracic echocardiography and contrast-enhanced electrocardiogram-gated computed tomography (ECG-gated CT) using a 64-detector-row scanner (LightSpeed VCT, GE Healthcare, WI, USA) for procedural planning. CT acquisition followed a uniform protocol: spatial resolution 0.488 × 0.488 × 0.625 mm, 512 × 512 matrix, slice thickness 0.625 mm, tube voltage 120 kV, tube current 250 - 350 mAs, pitch 0.984, gantry rotation time 0.5 s, and field of view between 38 and 50 cm. Approximately 1.8 mL/kg of contrast agent was administered, and the SmartPrep tracking technique was used to optimize bolus timing. Retrospective gating yielded ten cardiac-phase datasets covering the entire cycle, allowing accurate reconstruction of the aortic root and its pathology.

TAVI procedures were carried out transfemorally under general anesthesia, following manufacturer recommendations for optimal implantation depth, with the S3 frame positioned approximately one-third of its height below the annulus toward the left ventricle.

To document post-procedural device configuration, each patient underwent a follow-up ECG-gated CT scan one month after TAVI using the same acquisition parameters. These datasets provided the geometric ground truth for evaluating device expansion and validating the corresponding computational simulations.

The database is composed of a total of 130 patients. Demographic, clinical, and imaging data were collected to provide both morphological and functional reference parameters.

4.2 Segmentation process

The Mimics medical imaging software (v21, Materialise, Belgium) was adopted to reconstruct the aortic wall including the aortic root, valve leaflets and calcifications [46]. Segmentation process begins with pre-TAVI diastolic imaging acquired from ECG-gated CT. This imaging modality enables the reconstruction of aortic root anatomy at specific cardiac phases, including early diastole (70 - 80% of the R-R interval) and systole (20% of the R-R interval), which are essential for assessing the aortic root wall and native valve leaflet behavior in a personalized manner, as outlined by Catalano et al. [47].

Segmentation involves semi-automatic thresholding of the aortic root wall from the left ventricular outflow tract to the distal ascending aorta. This process employs Hounsfield unit (HU) thresholds (285 - 755 HU) to identify the aortic wall, with manual editing to remove coronary arteries at each ostium and to trim the mask at 15 mm below the aortic annulus and at mid-height of the ascending aorta. Global smoothing is applied to the mask boundary, using 10 iterations with a scale factor of 0.15 (see Fig. 4.1A).

To evaluate the accuracy of the segmentation process, a second mask was generated using the ISO50 threshold-based segmentation methodology, where the material boundary is defined as the middle greyscale value between the background and aortic lumen peaks in the greyscale value histogram. This mask did not undergo smoothing process, but similar cuts were performed below the aortic annulus and at mid-ascending aorta for comparative analysis.

Stenotic valve leaflets were modeled using anatomic measurements and 3rd-order NURBS curves in Rhinoceros software (Rhinoceros v.7, McNeel & associates, USA). Anatomical landmarks and spline curves are used to approximate the native valve leaflet shape, as outlined in prior studies [48, 49]. In brief, leaflet free edges were manually segmented by spline curves in the axial plane after multiplanar reformations of diastolic images. The leaflet-to-sinus attachments were identified by spline curves generated on the aortic root surface. Each leaflet belly was modeled using a curve that was constrained on both the leaflet-free-edge and leaflet-to-sinus curves. A single control point at mid-level was employed for modeling the curvature of native valve leaflets using a spline curve. The leaflet-to-sinus curves were projected onto the aortic root surface, and then the final shape of the native valve leaflets was developed using a multi-patch surface network. To evaluate the accuracy of our reconstruction approach, the black background enclosed by the native

valve leaflets was identified using mask cropping used to define the aortic valve region (see Fig. 4.1B).

The segmentation of calcifications was carried out using grey intensity values, with a fully automatic approach consisting of specific intensity thresholds to distinguish between calcified and non-calcified regions. As part of post-processing, the calcification mask underwent remeshing using Delaunay triangulation with a fixed uniform spacing of 0.3 mm. For comparison, a second mask for calcification was generated using automatic thresholding according to ISO50 method (see Fig. 4.1C).

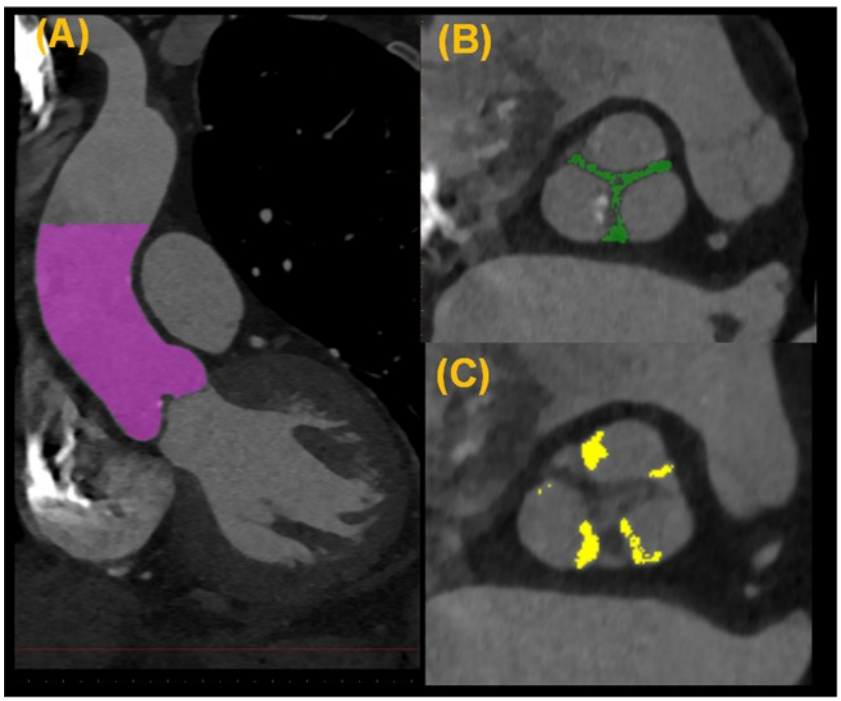

Figure 4.1: *Segmentation process showing (A) the mask for the aortic wall, (B) thresholding of native valve leaflets and (C) calcific plaques.*

4.3 Uncertainty in segmentation process

To quantify the accuracy of the proposed segmentation method, a study (enrolled 20 patients data from the database) was conducted by our research group, comparing the reconstructed anatomy to segmentations based on the ISO50 threshold-based methodology as a reference [50]. Segmentation errors in patient-specific anatomies are assessed using intersection over union (IoU) parameters to evaluate the similarity between the segmentation method and the reference approach. Twenty patients were selected from the database.

Table 2 displays the IoU parameter for segmented structures obtained through the two segmentation methodologies. The highest agreement among anatomies is observed for calcification (average of 93.4 ± 3.1 % for the patient study group), followed by the aortic wall (85.4 ± 8.4 %) and native valve leaflets (75.5 ± 6.3 %).

***Table I**: Agreement as expressed by the IoU between segmentation and standard volume rendering for each patient.*

				IoU		
	Age (yrs)	**Gender (-)**	**S3 size (mm)**	**Aorta (%)**	**Leaflet (%)**	**Calcification (%)**
#1	79	M	23	54.4	74.1	93.6
#2	86	F	23	80.8	81.4	93.0
#3	85	F	23	80.4	73.9	96.5
#4	94	F	23	70.6	72.4	89.5
#5	74	M	26	89.1	75.2	92.6
#6	76	M	26	88.6	88.4	91.6
#7	80	F	23	85.1	71.1	91.1
#8	75	M	26	78.7	75.4	91.0
#9	84	M	26	88.3	73.6	93.2
#10	82	M	23	82.4	81.5	85.9
#11	84	M	26	87.1	68.9	96.4
#12	78	M	26	85.7	76.8	92.1
#13	73	F	23	88.0	61.8	97.3
#14	69	M	26	89.0	75.2	95.1
#15	84	M	26	88.8	70.8	97.4
#16	84	F	26	88.3	67.8	95.2
#17	79	M	23	87.9	81.2	89.5
#18	78	M	26	87.3	83.2	92.4
#19	85	M	26	89.2	67.3	96.3
#20	85	F	23	87.8	70.1	97.7
mean	80.7	65%	45%	85.4	74.5	93.4
SD	5.7			8.4	6.3	3.1

Visual assessment of the agreement among anatomical parts of the segmented aortic root is illustrated in Figure 4.2.

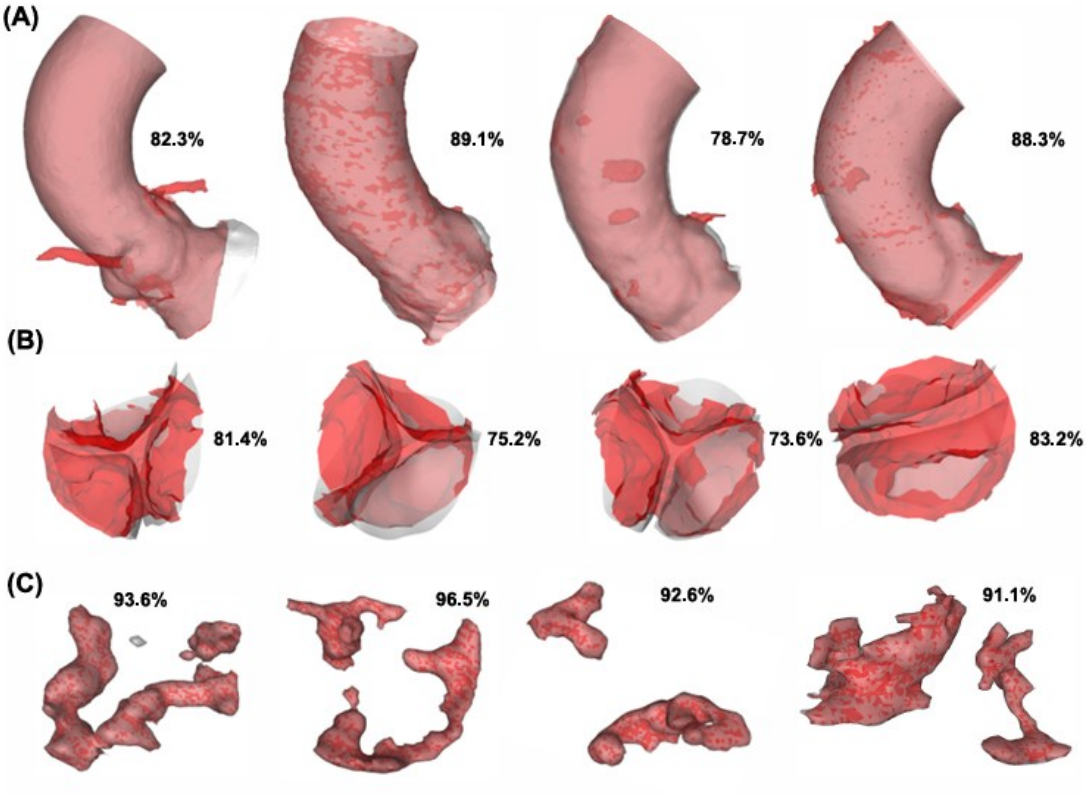

***Figure 4.2**: Comparison between the proposed segmentation method (red color) and the standard approach (grey color) for (A) aortic wall, (B) native valve leaflets and (C) calcifications in selected four patient's anatomies.*

This study aimed to enhance our understanding of the accuracy in the segmentation process from medical images to generate patient- specific models suitable for computational analyses. The IoU analysis assessed the impact of grey-value thresholding and post-processing of segmented masks on resulting aortic root morphologies.

4.2.1 Influence of voxelization

Phantom models were developed to determine the relationship between scanner resolution and the percent error in the segmented volume relative to the nominal phantom volume. To simulate calcifications, a spherical phantom with a nominal volume of 4187.7 mm^3 was created using the CAD software Rhinoceros (v7, McNeel & Associates, USA). The shape of the aortic lumen was replicated with a phantom-like pipe featuring a circular cross-section of 10 mm diameter and a radius of curvature of 0.0153 mm^{-1}, resulting in a nominal volume of 26953.0 mm^3. The CAD phantoms were voxelized through a process of converting them into greyscale images at various resolutions, including the ECG-gated CT image resolution

and lower resolutions aimed at reducing pixel size and slice thickness. After voxelization, the phantom volume was calculated and compared against the nominal CAD value and each low-resolution image.

Table II summarizes the RE in the segmented volume of CAD phantoms compared to the nominal phantom volume. After voxelization process at the baseline resolution of the ECG-gated CT scan, REs of 0.07% and 0.10% were found for the sphere and surface phantoms, respectively. In a different way, the RE due to image resolution increases as both the slice increment and pixel size increase, resulting in an 850% higher value compared to the reference CT resolution. Variations in phantom shape contribute to differences, with the spherical phantom being more sensitive to image accuracy compared to the surface model mimicking the aortic lumen.

***Table II**: Error in the segmentation process of CAD phantom models as a function of scanner voxel size including the slice increment thickness and pixel size.*

			Sphere		Surface	
Change (%)	**Slice Increment (mm)**	**Pixel Size (mm)**	**Volume (mm3)**	**RE (%)**	**Volume (mm3)**	**RE (%)**
0	0.40	0.445	1118.0	-	26943.1	-
30	0.52	0.578	1118.6	0.062	26952.5	0.033
60	0.64	0.712	1115.2	0.250	26943.5	0.034
90	0.76	0.845	1123.6	0.509	26952.3	0.035
120	0.88	0.979	1112.4	0.498	26955.6	0.047
150	1.00	1.112	1110.4	0.680	26945.9	0.100
500	2.40	2.952	1129.6	0.984	27125.6	0.678
675	3.10	3.813	1098.5	1.789	26707.1	0.876
850	3.80	4.674	1079.1	3.488	26648.2	1.095

4.3 Discussion

This study tries to improve the understanding of how accurately medical imaging data can be transformed into patient-specific anatomical models suitable for computational analysis. The investigation quantified the influence of the voxelization process on segmentation fidelity, demonstrating that its impact is morphology - dependent. Across the phantom models examined, voxelization produced only minimal discrepancies, typically below 1% when compared to their CAD-defined nominal volumes, indicating that discretization alone introduces relatively small geometric errors.

Segmentation accuracy was further evaluated in clinical patient anatomies, revealing that uncertainties arise not only from the nature of the anatomical structures but also from interpatient variability. The findings suggest that post-processing operations applied to

segmentation masks have a more substantial effect on geometric accuracy than the initial thresholding step. This was reflected in the IoU values, which were higher for structures less influenced by operator-dependent interpretation, such as calcific plaques, and lower for thin or poorly contrasted tissues such as native leaflets. For this reason, several research groups have addressed the performance of segmentation approaches and software [51-53] and their impact on resulting computational results [54, 55].

Although segmentation errors may appear modest at the geometric level, their influence on hemodynamic quantities can be considerable, as shown by Bertolini et al. [56], even small geometric variations can distort shear stress estimates in stenotic coronary arteries. These findings highlight not only the limitations of ISO50-type methods for patient-specific modeling but also the challenge of establishing standardized, reproducible segmentation protocols.

Overall, the study provides a comprehensive evaluation of segmentation accuracy within the framework of patient-specific TAVI modeling, emphasizing the distinct contributions of voxelization and segmentation methodology. While voxelization introduces only marginal deviations, the segmentation approach itself can meaningfully influence the resulting geometry and must therefore be carefully considered in the development of credible computational models.

Chapter 5

5. Statistical Shape Modeling and Virtual Cohort Generation

This chapter introduces the methodology for the development of statistical shape models in the context of TAVI [57]. THVs require extensive testing during their development to ensure safety and efficacy, traditionally demonstrated through pre-clinical studies and clinical trials. Similar to other engineering fields, the design and performance of biomedical devices can be significantly enhanced through computational modeling and simulation, which accelerate the design process and support the creation of more reliable solutions [58].

Clinical trials remain the cornerstone for assessing cardiovascular devices in the clinical setting; however, they are expensive and time-consuming. This scenario has stimulated growing interest in in-silico trials, which generate clinically oriented evidence by augmenting patient populations with synthetic cohorts derived from computational modeling [59, 60]. Such trials enable the systematic study of anatomies commonly excluded from clinical practice, such as bicuspid valves or younger patients, and provide novel insights into device performance in borderline cases. In the case of TAVI, early clinical trials excluded patients with bicuspid valves or those with longer life expectancy, whereas subsequent studies extended the evidence base to include these anatomies. In-silico trials can serve as a complementary approach by reproducing several anatomical scenarios and evaluating potential complications, thereby contributing to improvements in device design and patient selection.

The implementation of an in-silico trial for TAVI requires the construction of a synthetic patient cohort that replicates the variability of the target population. To achieve this, SSM provides a robust technique for quantifying anatomical variability and generating realistic virtual anatomies. When combined with machine learning, SSM can also support predictions of functional outcomes and device-specific considerations. For regulatory acceptance, such virtual cohorts must demonstrate credibility and reflect both the morphological and functional characteristics of real patients.

The work presented in this chapter develops a framework for extracting shape features of TAVI patients using geometric decomposition techniques. As a proof-of-concept, a virtual cohort of one hundred anatomies was generated and validated against clinical measurements.

Correlation and regression analyses were applied to assess the capacity of shape features to predict transvalvular pressure gradients, while machine learning was employed to explore the prediction of optimal prosthesis size. This framework aims to establish a foundation for credibility in in-silico trials, with potential applications in device optimization, pre-procedural planning, and the evaluation of anatomies at risk of suboptimal outcomes.

5.1 Clinical population and imaging acquisition

A prospective clinical study was conducted to enroll patients undergoing TAVI with the S3 THV within the framework of the H2020 project *SimInSitu*. From the database described in 4.1 section, a total of 68 patients with varying degrees of aortic valve stenosis were included. Devices of 23 mm and 26 mm diameter were implanted, whereas patients receiving the 29-mm prosthesis were excluded due to its infrequent clinical use at the institution (< 5% incidence).

Table III*: Study population characteristics of patients prior TAVI procedure. BMI = Body Mass Index, P_{sys} = systolic pressure, P_{dia} = diastolic pressure, EF = Ejection fraction, PAPs = Pulmonary arterial pressure.*

	TAVI Patient
	(N = 68)
Age (years)	80.52 ± 5.99
Height (cm)	159.25 ± 8.54
Weight (kg)	71.17 ± 13.55
BMI (-)	28.11 ± 4.88
BSA (m^2)	1.77 ± 0.20
P_{sys} (mmHg)	127.15 ± 19.13
P_{dia} (mmHg)	63.27 ± 10.92
Heart Rate (bpm)	71.25 ± 9.87
ECG-gated CT data	
Valve area AVA (cm2)	0.61 ± 0.13
Indexed valve area (cm2)	0.35 ± 0.07
Peak Gradient (mmHg)	79.11 ± 14.59
Mean Gradient (mmHg)	48.58 ± 9.87
Maximum Jet velocity (m/s)	4.40 ± 0.50
EF %	59.82 ± 7.82
PAPs (mmHg)	32.72 ± 11.75
Calcium Score (AU)	2120 ± 770
Cardiac Output (l/min)	4.11 ± 1.15
End Diastolic Left Ventricular Volume (ml)	99.68 ± 26.76
End Systolic Left Ventricular Volume (ml)	41.18 ± 17.37

5.2 Development of the Statistical Shape Model

Patient-specific surfaces of the aortic root and associated calcifications were preprocessed and aligned to create a consistent dataset for SSM. The following steps were performed:

1. **Resampling:** Meshes were uniformly resampled to ~30,000 points for the aortic wall and ~50,000 points for calcifications, ensuring adequate resolution while maintaining computational efficiency.
2. **Alignment:** A two-stage iterative closest point (ICP) procedure was employed:
3. **Rigid ICP:** standardized orientation and position across subjects.
4. **Non-rigid ICP:** applied for scaling adjustments, with convergence defined as < 0.01 mm change across three consecutive iterations. For calcifications, a relaxed tolerance (0.2 mm) was adopted to account for irregularity and variability of plaque distribution.
5. **Bias reduction:** Iterative realignment to the evolving mean shape minimized dependence on the initially selected reference patient.
6. **Shape representation:** After alignment, point coordinates were vectorized, concatenated, and assembled into a matrix encompassing the entire cohort.
7. **Principal Component Analysis (PCA):** Applied to extract orthogonal shape modes, where the first modes represent global size and curvature, while higher-order modes capture local variations, such as annular diameter, sinus expansion, or calcification distribution.

Model quality was assessed using generalization error, quantified by a leave-one-out reconstruction procedure. The mean squared error between the excluded anatomy and its SSM-based reconstruction was calculated for increasing numbers of shape modes, thereby measuring the ability of the model to represent unseen patient data.

5.3 Generation of the virtual patient cohort

A synthetic cohort of 100 virtual patients was generated as proof-of-concept by deforming the mean shape along principal modes of variation. Shape variations were sampled within ±2 standard deviations (σ), in steps of 0.5σ, covering approximately 90% of the population's morphological variability without generating unrealistic or folded geometries.

The probability of each deformed shape was quantified using the Mahalanobis distance combined with the chi-square cumulative distribution function (degrees of freedom = 3). This approach estimated the likelihood of anatomical plausibility for each virtual configuration.

Validation of the synthetic cohort was performed by comparing geometric parameters of the virtual anatomies with those of the original patient group. Metrics such as aortic annulus diameter and calcification volume were evaluated using both descriptive statistics and Mann–Whitney U-tests. Boxplots were used to visualize distributions, with synthetic geometries demonstrating close correspondence to the original dataset and no statistically significant differences in key anatomical metrics.

5.4 Correlation and regression analysis

To explore relationships between anatomical variability and functional parameters, Pearson's correlation was calculated between shape modes obtained from PCA and clinical variables. The clinical variables included peak transvalvular pressure gradient (AS-PPG), stroke volume, and post-procedural flow metrics derived from echocardiography.

For predictive modeling, a support vector machine (SVM) regression model was developed to estimate the AS-PPG based on selected shape modes. The six shape modes showing the strongest correlation with the target variable were retained. Bayesian hyper-parameter optimization was applied to identify the best-performing kernel and penalty parameters. A ten-fold cross-validation strategy was employed to mitigate overfitting and to evaluate model performance. Model accuracy was quantified using the root mean square error (RMSE) and the coefficient of determination (R^2), with the latter indicating the proportion of variance in the clinical data explained by the model.

5.5 Machine learning for predicting optimal device size

In addition to regression analysis, the predictive capacity of shape features was tested for prosthesis sizing. Patients were grouped according to the implanted device diameter (23 mm or 26 mm S3). The principal component scores obtained from PCA served as predictors.

Feature selection was performed using F-scores, identifying the most influential shape features for device sizing. Four machine learning classifiers were trained and tested:

1. Multilayer perceptron neural network

2. Logistic regression
3. k-nearest neighbors
4. Support vector machine

Data was divided into training (70%) and testing (30%) subsets. Model performance was evaluated using the area under the receiver operating characteristic curve (AUROC), together with confusion matrices, accuracy, recall, and precision metrics. This analysis aimed to assess whether three-dimensional shape features can outperform conventional two-dimensional annulus diameter measurements in guiding device selection.

5.6 Results

Figure 5.1 illustrates the scree plot, presenting the cumulative variance explained by each mode computed through PCA for the aortic root and calcification. To encompass 90% of the overall shape variability, the first 25 modes were necessary to account for the aortic root's shape variability, while 32 modes were required for capturing the calcification variance.

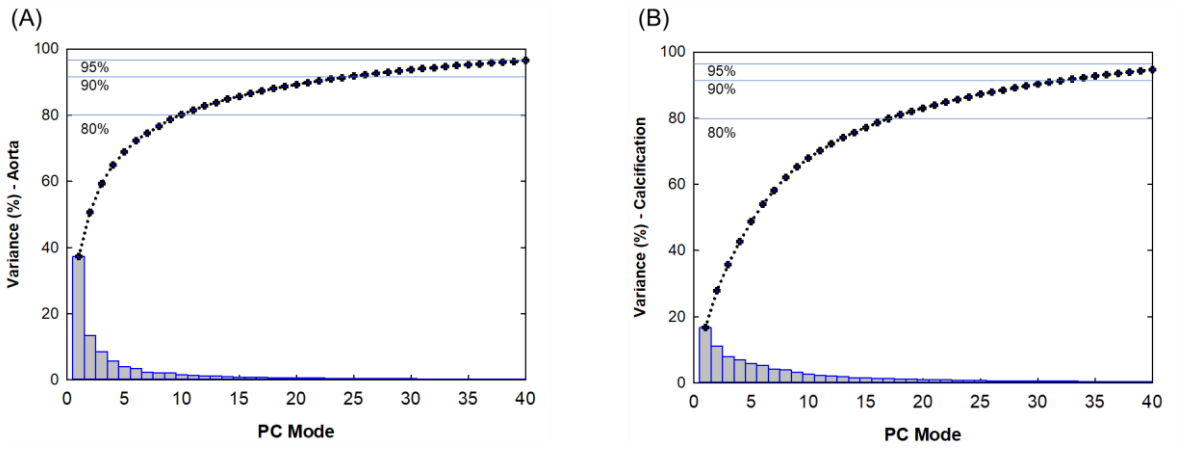

Figure 5.1: *Profile of scree plot (left column) and generalization (right column) of both aortic root and calcification resulting from SSM.*

The first six shape modes for both the aortic root and calcific plaques are depicted in Figure 4.2. Mode 1 for the aortic root represents approximately 39% of the overall shape variability and correlates with proportional vessel size changes (scale factor). Mode 1 for calcification illustrates variations in the distances among calcific plaques, accounting for 19% of the shape variations. Mode 2 for the aortic root manifests changes in vessel curvature (10% of variance), while modes 3 and 4 correlate with aortic annulus (3.8%) and sinus (2.9%) dimension variations, respectively. Notably, mode 4 of the calcification variance is linked to

changes in plaque volume (3.7% of variance), and mode 5 relates to plaque union among valve leaflets (2.7%).

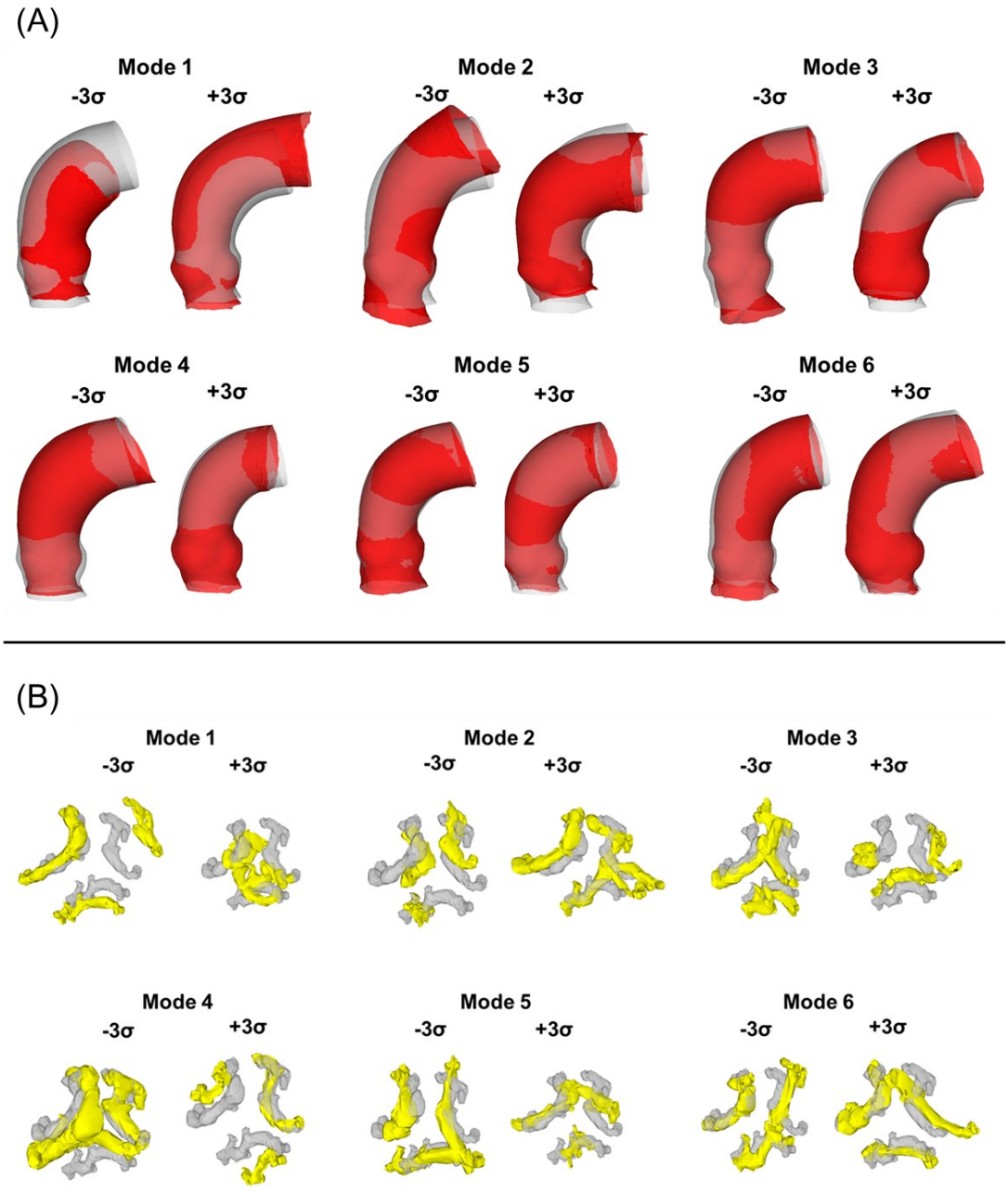

Figure 5.2: *Dominant shape modes shown by deformations of the computed template from low (− 3 σ) to high (+ 3 σ) values for A aortic root and B calcification.*

A virtual cohort of 100 anatomies was generated by deforming the mean shape within ±2σ across retained modes. Qualitative inspection confirmed the absence of non-physiological geometries.

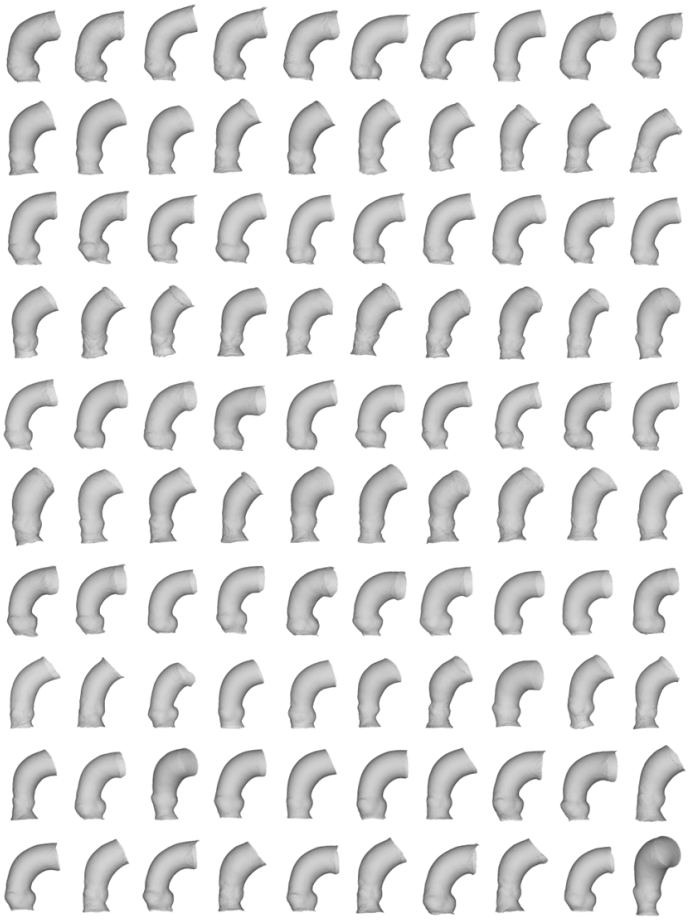

Fig. 5.3 *Synthetic data of n.100 virtual aortic root model.*

Analysis showed a deformed shape probability of 30.85%, 15.87%, 6.68%, 2.28%, 0.62%, and 0.14% for shape deviations of 0.5σ, 1σ, 1.5σ, 2σ, 2.5σ, and 3σ, respectively. As the synthetic models were obtained within ± 2σ, this suggests that only a marginal proportion (i.e., < 2.28% of shape variations) of morphological variance was not considered in our in-silico cohort.

Figure 5.5 displays boxplot graphs comparing the geometry of synthetic models against the original patient dimensions. The median annulus size for synthetic models falls within the 50th percentile of that for TAVI patients, indicating that synthetic vessels generally mirrored true anatomy. However, the median values for synthetic calcification volume slightly exceed those of TAVI patients, suggesting that synthetic calcifications were marginally larger than actual calcific plaques on average. Not any statistically significant difference was observed at Mann–Whitney U-test comparison among groups (i.e., $p = 0.425$ for the aortic root and $p= 0.318$ for the calcifications). The discrepancies in geometric measurement comparison can be attributed to several factors, including intra-operator variability and the lack of one-to-one correspondence.

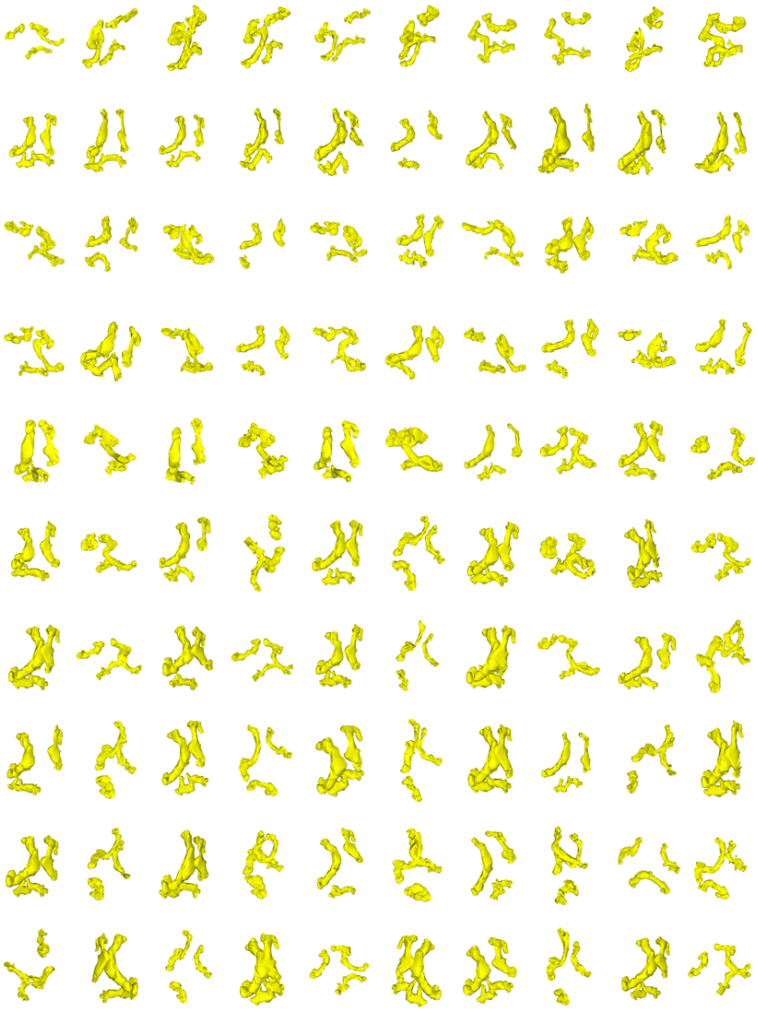

Fig. 5.4 *Synthetic data of n.100 virtual calcification.*

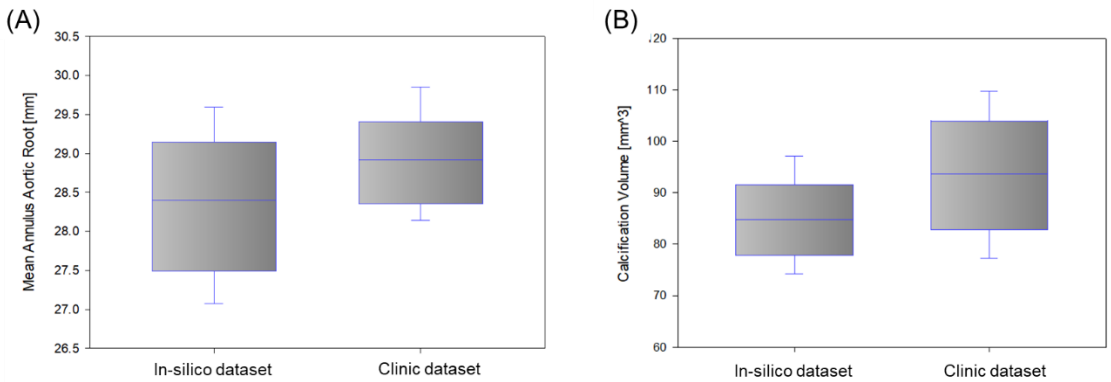

Fig. 5.5 *Boxplots comparing the A annulus diameter and B calcification volume between synthetic and clinical data.*

Significant associations between specific shape modes and clinical variables were identified (Figure 5.6). For example, mode 27 of the aortic root showed a positive correlation with transaortic flow jet velocity (R = 0.41, p = 0.001), while mode 4 was negatively correlated

with left ventricular stroke volume ($R = -0.38$, $p = 0.002$). Peak transvalvular pressure gradient displayed negative correlations with mode 59 of the aortic root and mode 37 of calcifications (both $R \approx -0.34$, $p < 0.01$).

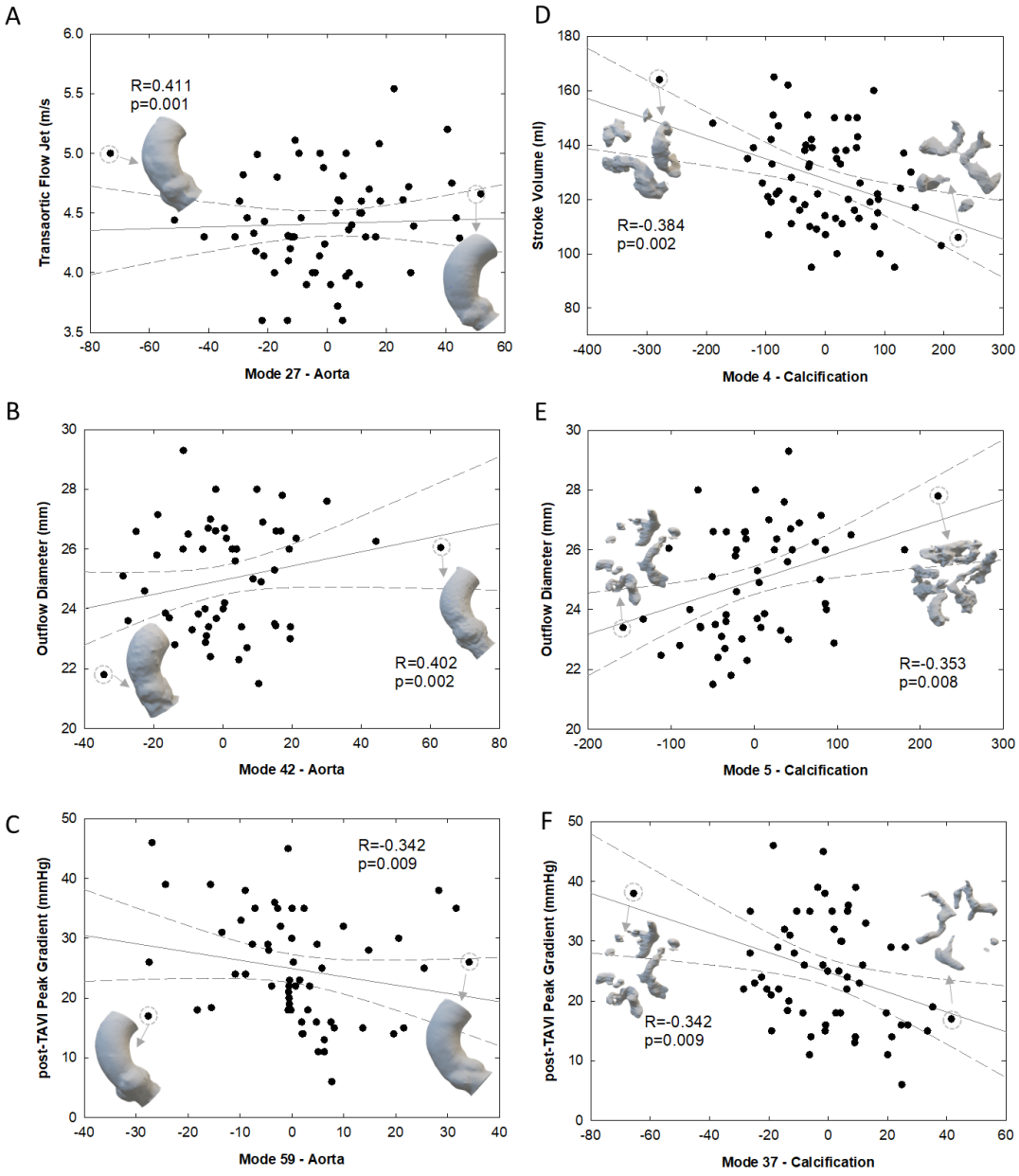

Fig. 5.6 *Pearson correlation showing associations of functional patient parameters with shape modes; (A) flow jet across the stenotic valve versus Mode 27 of the aorta; (B) device diameter at outflow versus Mode 42 of the aorta; (C) post-TAVI pressure gradient versus Mode 59; (D) patient stroke volume before TAVI versus Mode 4 of calcification; (E) device diameter at outflow versus Mode 5 of calcification; (F) post-TAVI pressure gradient versus Mode 37 of calcification.*

The SVM regression model trained on six selected shape modes achieved an R^2 of 0.55 and an RMSE of 11.7 mmHg (Figure 5.7). This result indicated that approximately 55% of the variance in AS-PPG could be explained by shape features alone.

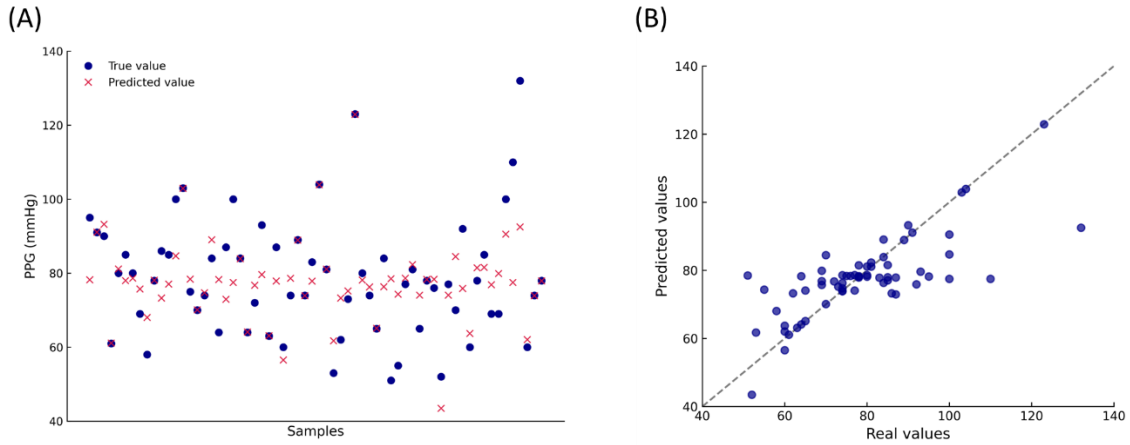

Fig. 5.7 *SVM regression of AS-PPG showing* ***A*** *the predicted and true response for each patient and* ***B*** *the comparison between predicted and true values.*

Among the machine learning models tested, the multilayer perceptron (MLP) demonstrated the highest predictive performance for device size classification. The MLP achieved an AUROC of 0.98, with accuracy values of 91.7% for the 23-mm group and 88.9% for the 26-mm group. Logistic regression, SVM, and KNN achieved lower but still acceptable performance.

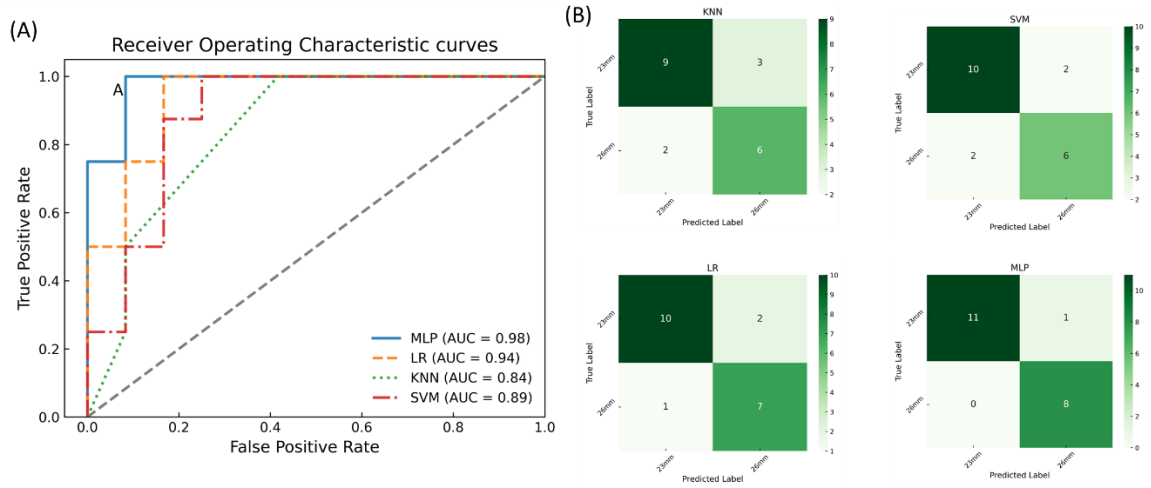

Fig. 5.8 *Machine learning classification showing (A) ROC curves and (B) confusion matrices for the investigated models.*

These findings confirmed that PCA-derived shape features can provide accurate predictions of optimal device size, outperforming single-parameter measures such as annulus diameter.

5.7 Discussion and Conclusion

The context of this chapter lies in the development of in-silico clinical trials, which use computational simulations to generate clinically relevant data on medical device performance [7, 61]. Such trials reduce cost and time while offering controlled, repeatable conditions that can complement or extend traditional clinical studies. Their utility is becoming increasingly recognized, especially in areas like TAVI where emerging clinical scenarios, such as valve degeneration and redo-TAVI, create new challenges. The feasibility of treating failed transcatheter valves with a second device has been demonstrated in recent clinical investigations [62, 63], underscoring the need for models capable of capturing complex anatomical and functional variability to support the design and evaluation of next-generation devices [64].

Within the cardiovascular field, SSMs have proven effective in quantifying anatomical variability [65] although relatively few studies have focused specifically on generating validated TAVI-specific virtual cohorts. For example, Bridio et al. [66] created a synthetic cerebrovascular population using random sampling of PCA modes, while La Mattina et al. [67] examined femoral fracture risk using virtual cohorts representing phase-III–scale populations. In the TAVI domain, Verstraeten et al. [40] expanded a retrospective dataset into a cohort of 500 virtual stenotic valves using a non-parametric SSM, though their model did not incorporate calcific plaque information. In contrast, the present work integrates both aortic root geometry and calcific burden, enabling a more comprehensive representation of the diseased anatomy.

The SSM constructed here demonstrated the capacity to replicate unseen patients, as shown by the generalization analysis, and identified shape features that correlate with clinically meaningful parameters. For example, the association between a root shape mode (mode 27) and the transaortic flow jet suggests that sinus morphology may influence flow distribution in stenotic valves. Similarly, high calcification volumes, captured by mode 4, were linked to reduced stroke volume, consistent with clinical findings in severe aortic stenosis [68].

The SVM regression achieved an R^2 of 0.551, capturing approximately 55% of the variance in pressure gradients, with a prediction error around 11.67 mmHg. While these results confirm the potential of shape-driven functional prediction, further improvements may be achievable through alternative ML architecture or enhanced feature engineering. Comparable studies combining SSM with computational fluid dynamics have demonstrated promising results using surrogate models or deep learning approaches [69].

Overall, Chapter 5 establishes SSM as a powerful framework for quantifying interpatient anatomical variability, generating geometrically credible virtual cohorts, and enabling morphology-driven predictive modeling. By linking shape descriptors to functional outcomes and device selection, this approach provides a quantitative foundation for in-silico TAVI evaluation and supports more patient-specific procedural planning.

Chapter 6

6. Patient-specific modeling of TAVI

This chapter describes the framework for the patient-specific simulation of TAVI, from cohort selection and imaging to device reconstruction and coupled structural–fluid simulations. The focus is on the Edwards S3 balloon-expandable transcatheter heart valve. The pipeline reproduces the clinical workflow implemented at IRCCS-ISMETT. Particular attention is given to the three-step structural simulation in Abaqus/Explicit (crimping → recoil → deployment) and to the subsequent SPH fluid simulations reproducing post-TAVI valve dynamics and hemodynamics.

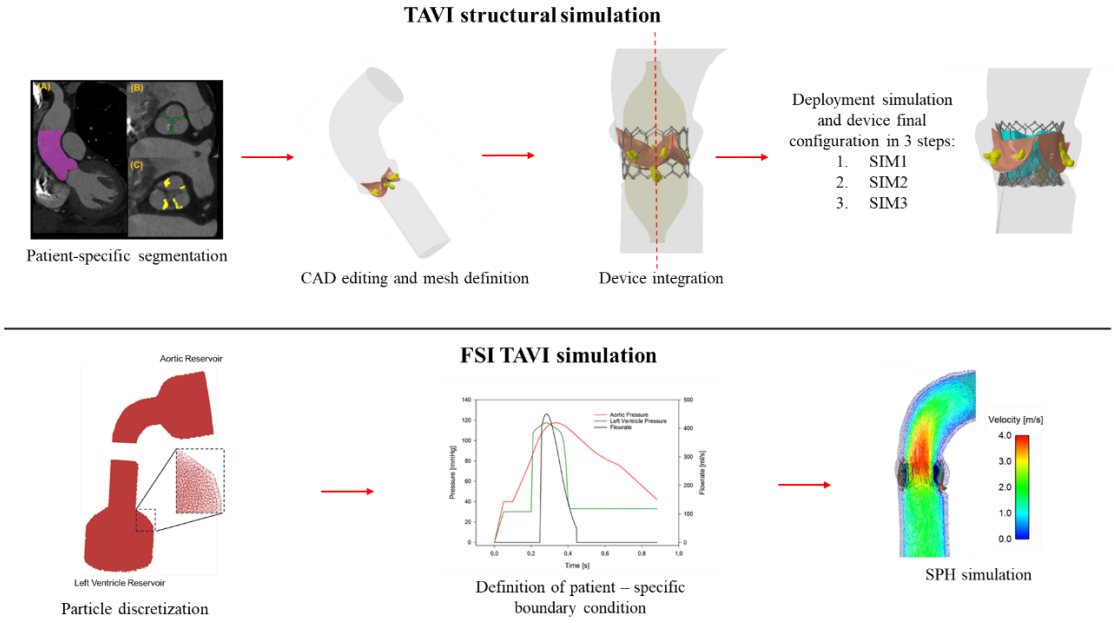

***Figure 6.1**: Workflow of structural and FSI simulation.*

This doctoral research project is embedded in ***Horizon SimInSitu project***, which aims to establish an automated, validated, and clinically driven computational workflow for patient-specific simulation of TAVI. As part of this broader framework, the thesis contributes to the development of modeling strategies capable of accurately reproducing the mechanical deployment and the hemodynamic performance of transcatheter heart valves by directly integrating patient-specific anatomical and physiological data. The overarching objective of the project is to generate a robust and reproducible in silico workflow, grounded in clinical evidence and capable of supporting procedure planning, device evaluation, and regulatory decision-making.

6.1 Patient-specific model definition

Patient-specific model segmentation was performed according to paragraphs 4.2.

In the context of SimInSitu project, the biomechanical response of the aortic wall is derived using an inverse approach, assuming a linear elastic material model [47]. Although the aorta exhibits anisotropic properties, recent studies on patient-specific TAVI modeling have validated the use of a linear elastic model against clinical data [70, 71]. The inverse analysis estimates material response from diastole to systole based on ECG-gated CT images, aiming to minimize discrepancies between simulated and observed aortic wall strain. For the patient-specific TAVI model, the inverse analysis yielded a linear elastic material parameter of 5.3 MPa after minimization of the difference between predicted and actual measurements of aortic wall strain.

The aortic root is modeled as a shell with uniform thickness of 2 mm and a Poisson's ratio of 0.475. These geometric and material parameters will serve as inputs for UQ analysis. Boundary constraints are applied by fixing the proximal and distal ends of the aortic wall in the longitudinal direction using cylindrical coordinate systems.

Native valve leaflets are meshed with triangular shell elements and subsequently converted to prismatic solid elements by offsetting the shell layer, assigning a uniform thickness of 0.5 mm. Material properties for the leaflets are determined through inverse analysis, using the CT-measured systolic orifice area as the output parameter in the minimization cost function. The derived material properties are then adapted to a neo-Hookean constitutive model (C10 = 3.7 MPa and D1 = 0.08 MPa), as this model offered greater numerical stability compared to a linear elastic model in the explicit-based simulations.

Calcifications are exported in STL format from Mimics and imported into ICEM software for mesh generation. Tetrahedral solid elements are used to mesh the calcific plaques, which are subsequently connected to the native valve leaflets through an embedment contact condition in the Abaqus finite element solver. Material properties for the calcific plaques are defined using a neo-Hookean material model based on data from Bosi et al. [71] (C10 = 67.7 MPa and D1 = 7.5×10^{-3} MPa).

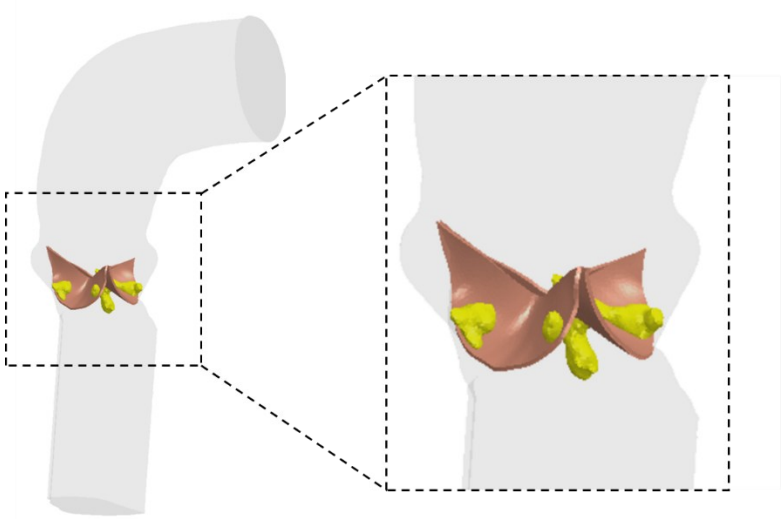

***Figure 6.2**: Final patient-specific model.*

6.2 SAPIEN 3 device reconstruction

This study focuses on TAVI simulation using the balloon-expandable Sapien 3 (S3) Ultra THV with a size of 23 mm. Detailed information on the numerical development of the S3 device model and the TAVI simulation process is provided in the work by Catalano et al. [47].

Compared to other computational simulations of the TAVI procedure, the stent frame is modeled using a hybrid approach with different mesh element types to optimize computational efficiency while maintaining the structural performance of the device. The stent frame is represented with surface elements to describe the outer device skin and beam elements to capture the device skeleton. This method is selected due to the thin, wire-like structure of the stent frame, which is effectively modeled with beam elements to represent the overall device stiffness and deformation behavior. The surface elements accurately model the contact interactions between the S3 stent frame and surrounding anatomical structures during the TAVI simulation.

Following verification analysis, the S3 geometry is meshed with 22,974 surface elements tied to 5,718 beam elements and is modeled using a cobalt-chromium alloy. The elastic material properties are defined by a Young's modulus of 238.54 GPa and a Poisson's ratio of 0.29. The plasticity model is characterized by a yield stress of 465.0 MPa, a hardening

parameter of 2,140 MPa, a strain-hardening exponent of 0.73, and a material density of 7,650 kg/m³.

The skirt, a fabric component that wraps around the stent frame, is modeled using solid elements to enhance contact interactions during the TAVI simulation. It comprises both an inner and outer skirt, designed to minimize blood leakage at the stent-aortic root interface. The skirt is initially modeled as a flat structure, then meshed and reshaped into a circular configuration to fit around the stent frame. The use of solid elements (with a thickness of 0.125 mm) allows for a detailed representation of the skirt interaction with both the stent frame and the patient-specific anatomy. The skirt is made of polyethylene terephthalate fabric, modeled as a Neo-Hookean hyperelastic material, with material parameters obtained from the literature (C10 = 1.7 MPa, D1 = 0.652 MPa) [72]. The skirt is represented using linear brick elements with reduced integration, and tie contact conditions are employed to simulate the suturing interaction between the fabric and the metallic stent frame. To mitigate unwanted high-frequency oscillations, Rayleigh damping factors and viscous pressure are applied to the device skirt.

The valve leaflets of the S3 model are generated through a forming simulation process, as outlined by Bailey et al. [26]. In this process, the leaflets are initially constructed in a planar position and then deformed into their final functional shape using a series of geometric operations. The device valve leaflets are meshed with 1,457 structured elements and a single solid-element layer through the thickness, with full integration.

The biomechanical response of the pericardial tissue in the valve leaflets is modeled using the Ogden constitutive law with a second-order polynomial form. The material parameters are defined as: $\mu1 = 0.96$ MPa, $\alpha1 = -56.5$, $\mu2 = 3.57$ MPa, $\alpha2 = 1.87$, and D1 = 0.027 MPa [26]. This model captures the nonlinear, elastic behavior of the tissue, which is critical for accurately simulating leaflet function during the opening and closing phases of the valve. Similar to the skirt, the valve leaflets are tied to the S3 stent with secondary node being tied to two different primary nodes to avoid over-constraint.

The balloon-expandable geometry is extrapolated from the study by Bailey et al. [26], where photography was used to model the outer balloon profile and revolution around the axis to derive the final balloon geometry. The balloon is discretized with 82,322 unstructured shell elements and modeled with neo-Hookean material properties (C10 = 36.5 MPa, D1 = 1.36

$\times 10^{-3}$ MPa). These material parameters are derived from multiple simulations designed to replicate the balloon inflation process.

6.3 Computational modeling of TAVI

6.3.1 Structural simulation of TAVI

Prior to implantation, the device is placed on the folded balloon catheter and crimped to a specified diameter so that it can fit inside the sheath. Device positioning is then accomplished using radiopaque valve-related alignment markers on the balloon catheter, which define the working length. A 3-mm center marker, located at the midpoint of the balloon catheter, is used for deployment (i.e., the Commander delivery system). The distal end of the balloon marker is aligned with the base of the aortic valve cusps, representing the aortic annulus circumference by the three hinge points on the aortic annulus.

According to manufacturer's guidelines, the S3 device is placed with 80-90% in the aorta while the remaining 10-20% faces the LVOT. The balloon axis is aligned perpendicular to the aortic valve plane. Balloon inflation, controlled by a specified fluid volume, is used to deploy the device in the human host.

To replicate this clinical procedure, an automatic framework based on Python was developed by our partner 4Realsim to align the device in the patient-specific model. The patient-specific model served as input for the Python script. To enable the automated integration of the patient-specific platform with the S3 TAVI system, the three hinge points were identified for each patient by detecting their coordinates from the CT scans. The balloon axis was computed as the axis of the circle defined by these three hinge points, intersecting the annulus at its center. A cylindrical reference system was then created, with the center of the aortic annulus as the origin and the -z axis aligned along the balloon axis.

The script then automatically positioned the device system at the level of the balloon radiomarker (i.e., at the midpoint of the balloon) and aligned the delivery system with the aortic annulus. Two parameters, the balloon axial position shift and the radiomarker shift, were defined to control the relative position between the device and the patient model. The balloon axial position shift ensured the alignment of the balloon and catheter with the S3 device, while the radiomarker shift adjusted the entire S3 system along the balloon axis (-z direction) to ensure proper positioning on the aortic annulus. The final implantation depth,

derived by post-TAVI CT scans, was used, ensuring optimal placement. The integration process was standardized across all patient models and device sizes by using consistent terminology for each anatomical part, datum feature, and mesh. The device selection, size, implantation depth, and balloon inflation volume were all parameterized, allowing the script to adjust the model automatically based on user input. To model the complex delivery of the S3 system into the aortic root, several contact conditions were defined. These included tangential behavior modelled with a penalty friction formulation and normal behavior with hard contact.

In SIM-1, the metallic stent frame is crimped onto the folded balloon to achieve the nominal crimped diameter, followed by the stent's recoil. The final stage involves balloon inflation and deflation, deploying the device. This process is executed using a fluid cavity approach in combination with a VUAMP subroutine, which controls the stent expansion to its nominal diameter based on the inflation volume. Additionally, a cylindrical surface is employed to displace calcified plaques and native leaflets, preventing undesired penetration during the assembly of other device components. A 0-velocity boundary condition is applied to the stent to ensure stability.

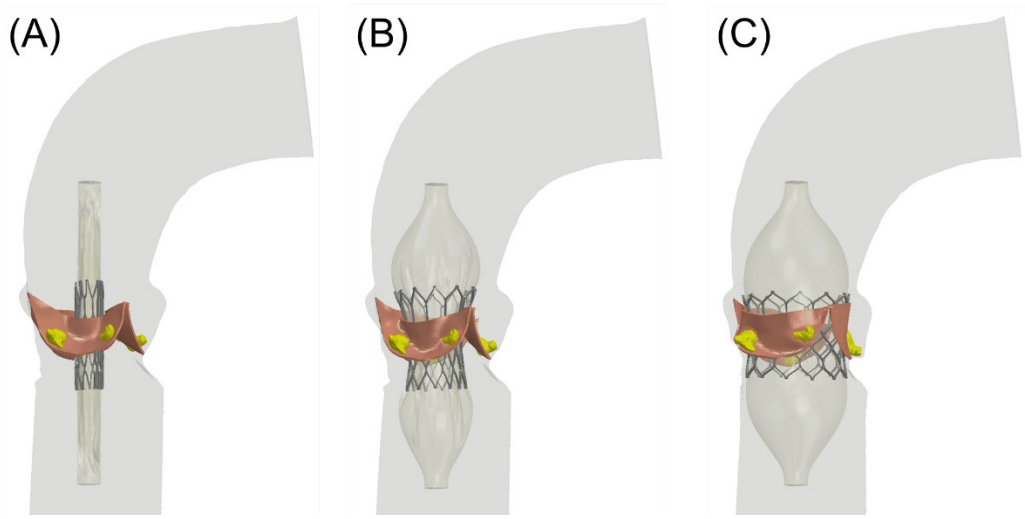

***Figure 6.3**: Different steps of SIM1 simulation; from crimped S3 (A) to final deployment (C).*

In SIM-2, the deformed configuration of the device, including the valve leaflets and skirt, is imported, as these components were not included in SIM-1. During this single-step simulation, the S3-related leaflets and skirt are introduced, and constraints are established between the stent, leaflets, and skirt. The nodal displacements from SIM-1 are first applied to the stent in its undeformed state. As the simulation progresses, these displacements guide

the stent to its final deformed configuration. Since the leaflets and skirt are constrained to the stent from the beginning, they deform accordingly throughout the process.

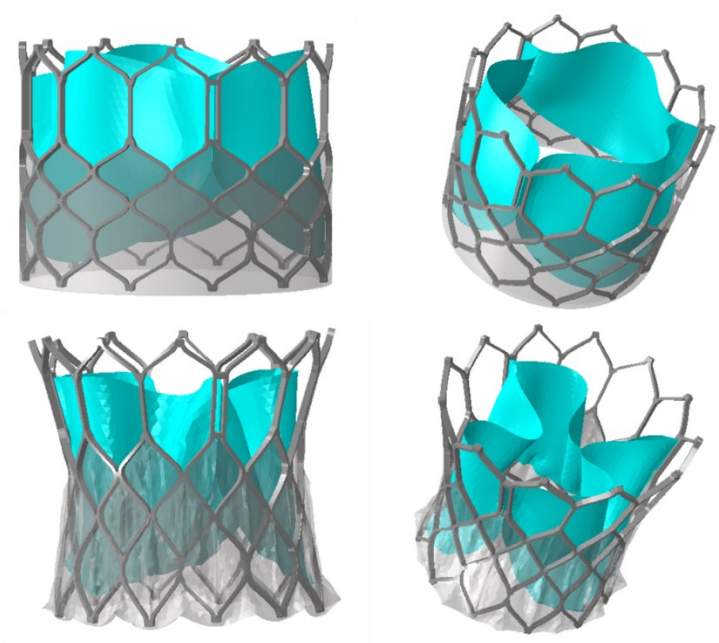

***Figure 6.4**: SIM2 simulation; final deformed S3 configuration.*

In SIM-3, the entire device is fitted into the patient-specific platform, with all components imported in their deformed state from SIM-1 and SIM-2. The surface used in SIM-1 to displace calcifications and native leaflets is returned to its original dimension, allowing the anatomical parts to elastically recoil and make contact with the S3 skirt. High-friction contact is established between the skirt, stent, native leaflets, aorta, and calcifications to prevent slippage during flow analysis. The components are imported using a shrink-fit approach, resolving overclosure and enhancing friction between the device and the patient-specific anatomy.

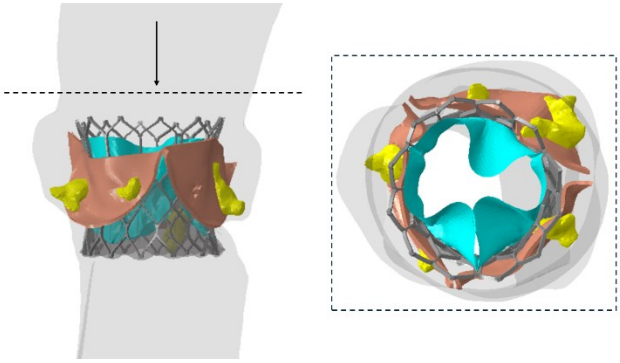

***Figure 6.5**: SIM3 simulation; final TAVI configuration.*

6.3.2 SPH-based fluid simulation of post-TAVI dynamics

An FSI approach based on the meshless SPH method is developed to simulate post-TAVI hemodynamics. The SPH is a fully Lagrangian modeling technique that discretizes continuum equations by interpolating the properties of particles within the solution domain. This method calculates fluid-flow values at specific points by using the properties of surrounding particles. The SPH method offers remarkable advantages over other FSI techniques in TAVI [32, 35], as it is fully integrated into the Abaqus/Explicit finite element software, making the SPH particularly suitable for modeling contact interactions between the fluid domain and structural components of the anatomy.

The SPH analysis starts with the deformed configuration of the anatomy with the deployed S3 device. Patient-specific simulations are carried out within the Abaqus solver, with the cubic kernel formulation set as the default. To facilitate particle discretization and collection, a dummy model with two fluid reservoirs is created and strategically positioned at both ends of the aorta using tie constraints. The fluid domain is converted into SPH particles via background grid conversion. The blood is modeled as an incompressible, Newtonian fluid using the Hugoniot equation of state and data from the literature [73]. Particle discretization and material properties were summarized in Table IV.

***Table IV**: Particle discretization and material properties of the fluid domain.*

Particle diameter	0.9 mm
Density, ρ	1.0E-09 tonne/mm^3
Wave speed, $c0$	7.5E+04 mm/s
Grüneisen ratio, $\Gamma 0$	0
Hugoniot curve slope, s	0
Viscosity, η	3.0E-09 Mpa*s
Bulk viscosity damping coefficient	0.006

The interaction between the patient-specific TAVI geometries and blood particles is modeled as contact pairs using a general contact definition. Patient-specific flow boundary conditions are derived from clinical data collected during in-hospital admission.

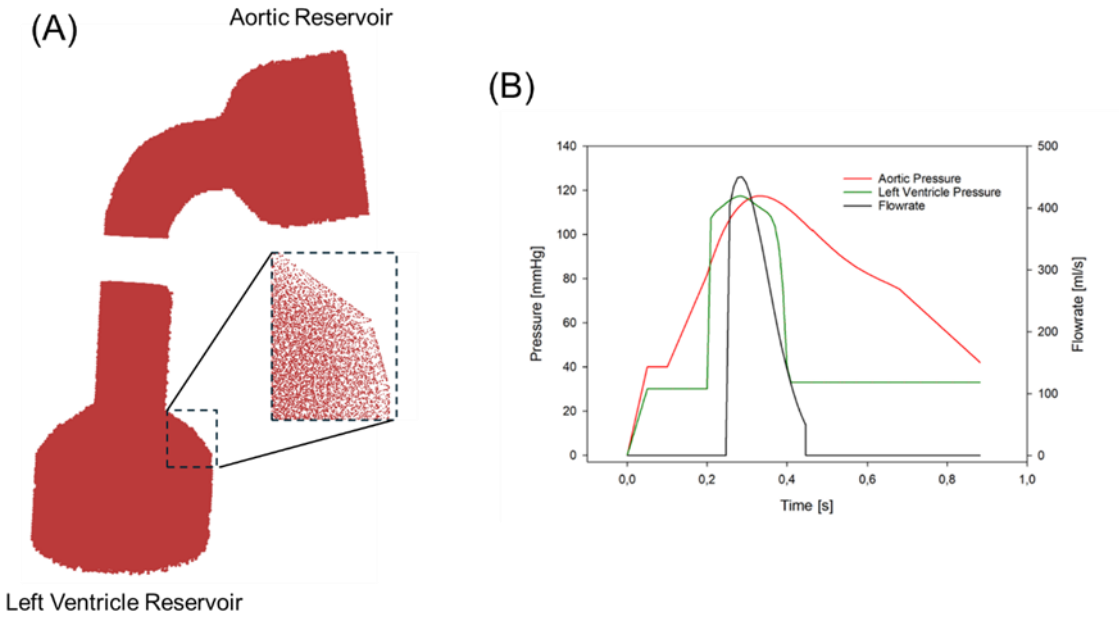

***Figure 6.6**: (A) Particle discretization of blood; (B) Physiological boundary conditions derived from patient - specific data.*

These include the heart rate, cuff pressure, and aortic jet velocity from Doppler echocardiography, which are used to scale the duration and offset of pressure and flow waveforms. During systole, the flow is governed by the flow rate curve, which is applied as a velocity boundary condition on the left ventricular reservoir. During diastole, the velocity boundary condition is deactivated, and flow is driven by the pressure boundary condition, generating a gradient between the left ventricular and aortic pressures. The aortic reservoir functions as a fluid collector during systole and contracts during diastole to simulate in-vivo arterial compliance. Switching between the flow boundary conditions is achieved by utilizing a single truss element with temperature-dependent stiffness properties. The vessel is initialized with a load condition derived from the structural TAVI simulation, which is imported into the SPH model using a predefined field.

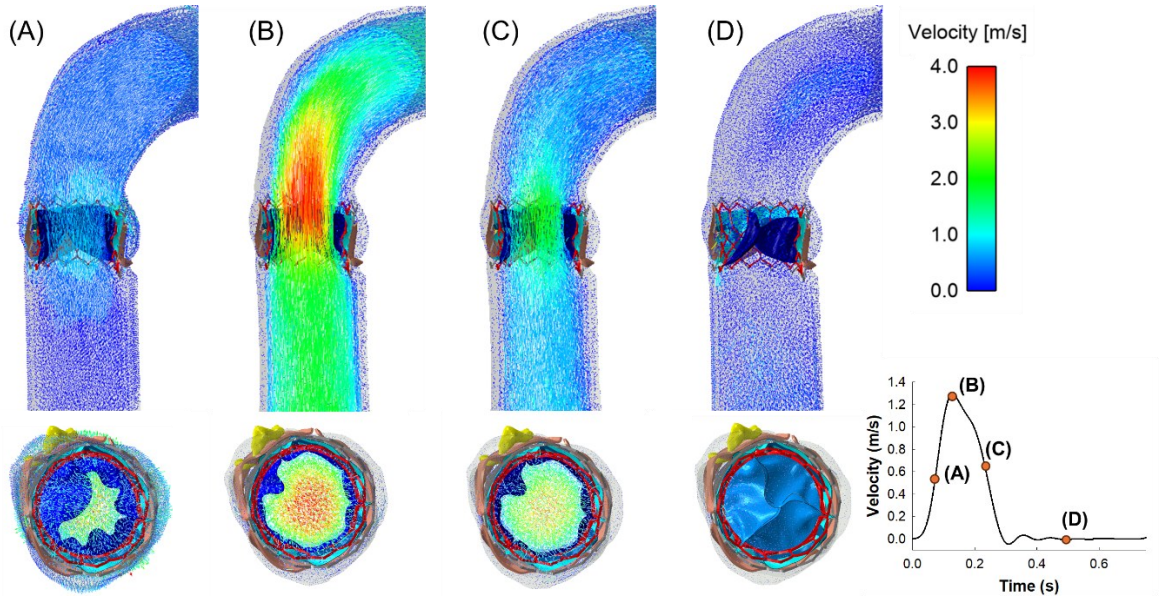

***Figure 6.7**: Different steps of SPH simulation across one cardiac cycle; from (A) at the beginning of systole, (B) peak systole, (C) diastole and (D) late diastole.*

6.4 Conclusion

This chapter presented the complete workflow developed for patient-specific simulation of TAVI procedures, detailing the reconstruction of individualized anatomical structures and the integration of the S3 Ultra device with its delivery system.

Once the patient-specific platform was established, Python-based automation enabled the systematic insertion of the TAVI system across the entire cohort, substantially accelerating the modeling pipeline. These methodological innovations significantly streamline the generation of high-fidelity models for large populations and support the systematic validation of the proposed in silico framework.

Most existing finite element models of patient-specific TAVI do not incorporate all procedural components or device features [19, 71, 74]. In contrast, the platform established in this chapter integrates the full TAVI device geometry, delivery catheter, and surrounding anatomy, representing an advancement beyond the current state of the art.

Building upon the development of a high-fidelity patient-specific modeling framework, the next chapter focuses on assessing the credibility, reliability, and regulatory readiness of the computational simulations through a rigorous VVUQ process aligned with the ASME V&V40 standard.

Chapter 7

7. Uncertainty Quantification in TAVI Models

The predictive accuracy of computational models for simulating device deployment in stenotic aortic valves is affected by multiple sources of uncertainty, including variations in imaging modalities, model assumptions, and biological variability across patients. Systematic uncertainty analyses are essential to identify and characterize these uncertainties, facilitating quantification of variability in model predictions. Sources of uncertainty impacting model predictions include epistemic uncertainty (arising from incomplete knowledge) and aleatoric uncertainty (arising from inherent variability). Rigorous validation and quantification of these uncertainties are crucial for improving model credibility, thereby supporting the development of safe and effective medical devices [42, 75].

Model credibility assessment involves a systematic approach, including VVUQ, alongside an applicability assessment to address model risk and output rigor [76, 77]. Verification evaluates whether the computational model accurately implements the underlying mathematical model and its solution. Validation assesses how well the model reflects corresponding physical experiments or in-vivo data relevant to the model intended use. In contrast, uncertainty quantification (UQ) examines the influence of input uncertainties on model outputs [55]. Finally, model risk encompasses the potential for the computer model to produce incorrect results, leading to undesirable outcomes in subsequent clinical decisions. Such a framework was proposed by FDA to quantify model credibility and was largely based on the ASME V&V40 standard, "Verification and Validation in Computational Modeling of Medical Devices" [44, 45].

This chapter presents an application of the ASME V&V40 framework to establish the credibility of computational modeling for TAVI simulations. The ASME V&V40 standard is applied to the case of patient-specific TAVI modeling to define a risk-informed approach to model credibility. The study introduces the validation and uncertainty framework, which validates the computational model against clinical data (i.e., the comparator) and examines the influence of various uncertainties on model response. This analysis employs techniques such as surrogate modeling, Pareto plots, and cumulative distribution functions to assess agreement levels between simulations and clinical data.

We investigated the case of two patients who underwent TAVI with the 23 mm S3 device and two patients underwent TAVI with the 26 mm device (Figure 7.1). The restriction to four patients was dictated by the remarkable computational efforts needed for developing the surrogate model for probabilistic analysis.

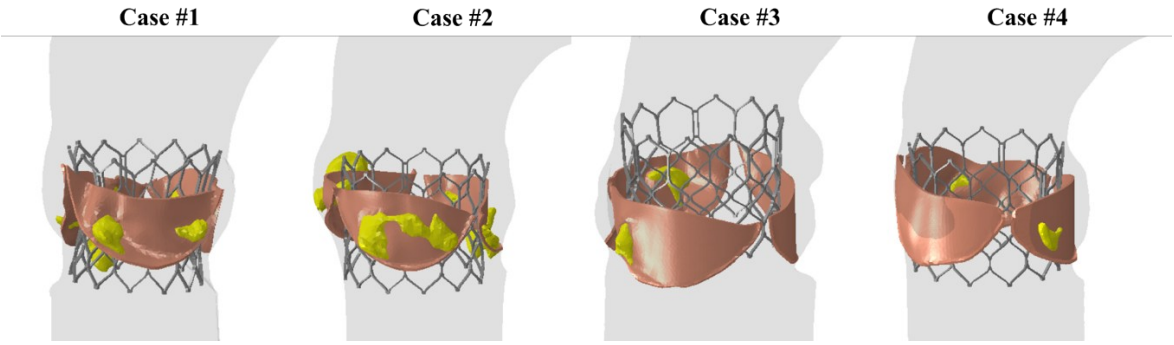

***Figure 7.1**: Patient – specific models analyzed for UQ analysis: Case #1 and Case #2 with a 23 mm S3 e Case #3 and Case #4 with a 26 mm S3.*

7.1 ASME V&V40 Application

The ASME V&V40 framework offers a structured methodology for assessing the credibility of computational models, particularly in the context of medical device applications [44]. This framework is crucial for ensuring the accuracy and reliability of models used to simulate real-world phenomena. The credibility assessment process begins with the definition of the Question of Interest (QoI), which specifies the specific prediction or simulation goal of the model. Following this, the Context of Use (CoU) is defined, detailing the conditions under which the model will be applied and the associated risks.

The ASME V&V40 framework underscores the significance of model risk assessment, which involves evaluating both the potential for the model to generate incorrect results (model influence) and the consequences of such errors (model consequence). The framework adopts a risk-based approach to determine the appropriate level of rigor for VVUQ activities (Figure 2). This approach ensures that models with higher associated risks undergo more stringent credibility evaluations. Additionally, the framework includes the specification of credibility goals, which define the acceptable levels of accuracy and uncertainty in the model predictions. These goals are established based on the model intended application and the risks involved. For high-risk applications, more stringent credibility goals are set, necessitating more comprehensive VVUQ processes.

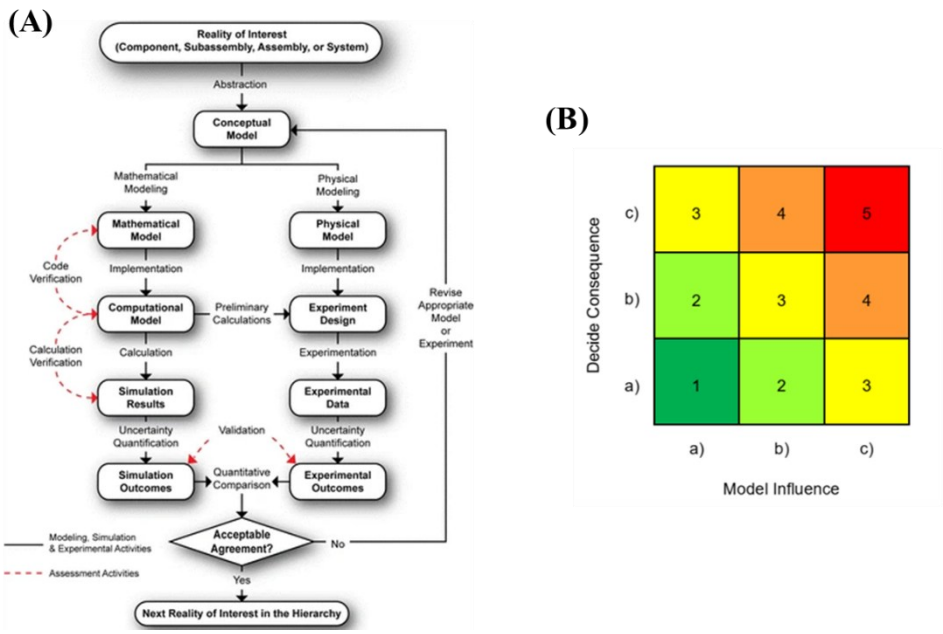

Figure 7.2: *(A) VVUQ activities suggested by the ASME V&V40 for the simulation and experiment to establish the credibility of the computational model – with permission from Schwer et al. [78] (B) model risk matrix.*

For the patient-specific TAVI modeling, the following Question of Interest (QoI) and Context of Use (CoU) are defined:

QoI: "Can the S3 stent-frame model be successfully deployed in a patient-specific aorta at a given position within the calcified aortic valve leaflets, and will it replicate heart valve function?" From a clinical perspective, the severity of calcified aortic valve dysfunction depends on the pattern of calcific plaques, the reduction in orifice area during the cardiac cycle, and the post-operative hemodynamics.

CoU: Given the substantial variability in calcification patterns, annulus sizes, and patient demographics, patient-specific modeling provides an essential tool for simulating the post-TAVI patient condition. This enables prediction of both the aortic wall's structural and fluid-dynamic behavior.

The VVUQ process evaluates whether the model accurately represents post-TAVI valve function, particularly with regard to device expansion within stenotic valve leaflets and the fluid-induced loading on the vessel. Validation metrics associated with the QoI include:

Device Diameter (DD): The S3 device is assessed at three cross-sectional levels (inflow, mid, and outflow) based on diameter measurements of the deformed device. The minimum

and maximum device diameters of the S3 stent frame are automatically measured, with the average value used for validation.

Effective Orifice Area (EOA): EOA is calculated by post-processing the flow velocity and pressure curves according to ISO 5840-1, by using the Gorling equation.

Transvalvular Pressure Gradient (TPG): The pressure gradient across the device valve leaflets is calculated from blood velocity, as done in clinical echocardiographic estimates.

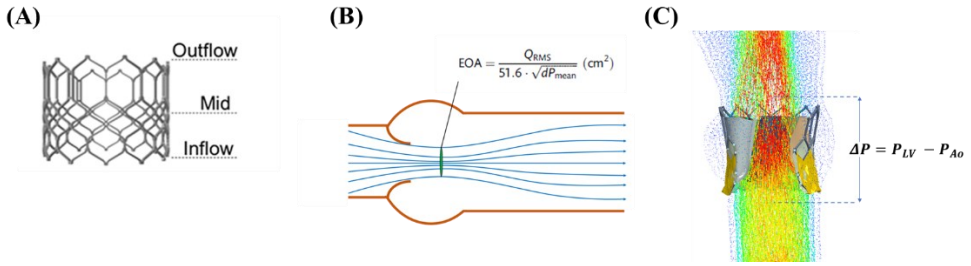

Figure 7.3*: Validation metrics; (A) DD at three different levels – inflow, mid, outflow; (B) EOA calculated with Gorlin equation [79]; (C) TPG calculation.*

Regarding model risk, both the model influence and decision consequence are classified as "high". This is due to the direct application of the model in informing decisions about a medical device, where inaccurate predictions could potentially result in severe patient harm. Accordingly, a risk level of 5 on a 1 - 5 scale is assigned (see Figure 7.2B) to the patient-specific TAVI model, indicating the necessity for stringent credibility goals within the ASME V&V plan. This severity level establishes the rigor required for VVUQ activities, with relevant model changes constrained to Relative Error (RE) below 5%.

7.2 Uncertainty Quantification in TAVI simulation

UQ plays a critical role in elucidating the variability in model predictions arising from uncertainties in input parameters and model assumptions. This process entails characterizing the uncertainty inherent in model inputs and evaluating its influence on the resulting outputs. Common techniques for UQ analysis include surrogate modeling, Monte Carlo simulations (MCS) and sensitivity analysis. In the context of patient-specific TAVI modeling, uncertainty can arise from multiple sources and can be broadly classified into epistemic and aleatoric uncertainties.

7.2.1 Epistemic Uncertainty

Epistemic uncertainty, also known as reducible uncertainty, originates from a lack of knowledge or incomplete information about the system being modeled. In the setting of TAVI computer modeling, the following sources of epistemic uncertainty are considered:

- **Imaging and segmentation**: variability in imaging techniques and the resolution of imaging modalities like CT scans can lead to inaccuracies in the segmentation of anatomical structures. These inaccuracies can propagate through the model, affecting the overall predictions.
- **Material properties**: the constitutive models that describe the mechanical behavior of the aortic root, valve leaflets, and other components rely on material properties that may not be precisely known. The experimental data used to derive these properties often comes with inherent uncertainties.
- **Boundary and initial conditions**: assumptions regarding boundary and initial conditions, such as physiological pressures and valve positioning, can introduce uncertainties. These conditions are often estimated based on limited clinical data or generalized assumptions.
- **Modeling assumptions and simplifications**: simplifications and assumptions made to make the computational model tractable, such as assuming uniform material properties or neglecting certain physiological interactions, can introduce significant epistemic uncertainties.

7.2.2 Aleatoric Uncertainty

Aleatoric uncertainty, also known as irreducible or stochastic uncertainty, is associated with the inherent variability and randomness in biological systems. In TAVI computational models, sources of aleatoric uncertainty include:

- **Patient-specific variability**: biological variability among patients, such as differences in anatomy, tissue properties, and physiological conditions, contributes to aleatoric uncertainty. Each patient presents a unique set of characteristics that can affect the outcome of the TAVI procedure.

- **Intra-observer variability**: measurement of S3 diameter after TAVI procedures or echocardiographic estimates are influenced by the operator experience leading to difference in the resulting evaluations. These errors are often not quantifiable.
- **Environmental and procedural variability**: variability in procedural execution, such as the exact positioning of the valve during implantation and the skill level of the operator, can introduce aleatoric uncertainties. These variations are often beyond the control of the modeler.

On the basis of the established aleatoric and epistemic uncertainties, the following model inputs and associated changes are investigated (see Table V):

- **Aortic wall thickness**: the thickness of the aortic wall is a crucial parameter for simulating the mechanical behavior of the aorta. The nominal thickness is set at 2 mm, with an epistemic uncertainty range from 1.5 to 2.5 mm. This range is defined based on engineering judgment, capturing the variability in patient anatomy.
- **Neo-Hookean calcification parameter**: this material parameter represents the stiffness of calcified regions within the aortic valve. The nominal value is set at 67.8 MPa, with an uncertainty range from 40 to 100 MPa, based on engineering judgment.
- **Neo-Hookean aorta parameter**: this parameter describes the mechanical properties of the aortic tissue wall. The nominal value is 0.98 MPa, with an aleatoric uncertainty standard deviation of 0.24 MPa, derived from estimations based on the inverse analysis [15]. This parameter ensures that the elasticity of the aortic wall is accurately represented in simulations.
- **Implantation depth of the S3 device**: The depth at which the S3 THV is implanted influences both mechanical stability and hemodynamic performance. The nominal implantation depth is set at 6 mm as collected from the clinical procedure, with an uncertainty range from 5 to 7 mm, determined based on clinician judgment.
- **Fluid volume of balloon expansion**: This parameter affects the deployment of the balloon-expandable valve. The nominal value is 17 mL according to manufacturer guidelines, with an epistemic uncertainty range from 16 to 18 mL and an aleatoric uncertainty component of 0.1 mL, based on typical production tolerance of the medical syringe.

- **S3 stent-frame material parameter**: the elastic material properties of the S3 stent-frame are relevant for the radial force exerted on the aortic tissue wall and thus the device expansion. The nominal value is 238.5 GPa, with an epistemic uncertainty range from 229.6 GPa to 247.4 GPa and an aleatoric uncertainty component of 30 GPa.

- **Diastolic blood pressure**: the diastolic blood pressure measured at in-hospital admission is critical for assessing the hemodynamic performance of the S3 THV. The nominal value is set at 63.5 mmHg as measured for the investigated patient, with an aleatoric uncertainty standard deviation of 10.64 mmHg, reflecting patient variability.

- **Systolic blood pressure**: The systolic blood pressure from cuff measurement is another key hemodynamic parameter. The nominal value is set at 127.3 mmHg, with an aleatoric uncertainty standard deviation of 16.44 mmHg, capturing the range of pressures experienced during the cardiac cycle.

- **Velocity flow jet**: The velocity of the flow jet across the valve as collected from Doppler echocardiography is essential for evaluating the device performance. The nominal value is 2.4 m/s, with an aleatoric uncertainty standard deviation of 0.5 m/s.

- **Heart rate**: the heart rate influences the duration of the cardiac cycle and the hemodynamic loading on the S3 THV. For the investigated patient, the nominal value is 71.2 bpm, with an aleatoric uncertainty standard deviation of 9.74 bpm, accounting for patient-specific variability.

Table V: *Model inputs and uncertainties for UQ analysis with the boundary adopted for validation of patient-specific TAVI model. EUQ = epistemic uncertainty; AUQ = aleatoric uncertainty; LB = lower bound; UB = upper bound; s = standard deviation.*

Model Inputs	Nominal	Units	EUQ LB	EUQ UB	AUQ σ	Mixed LB (2σ)	Mixed UB (2σ)
Aortic Wall Thickness	2.0	mm	1.5	2.5	0.0	1.5	2.5
Neo-Hooke Calcification Material	67.8	MPa	40.0	100.0	0.0	40.0	100.0
Neo-Hooke Aorta Material	0.98	MPa	/	/	0.24	0.5	1.4
Implantation Depth	6.0	mm	5.0	7.0	0.0	5.0	7.0
Balloon Expansion	17.0	mL	16.0	18.0	0.1	15.8	18.2
Stent Young Modulus	238.5	GPa	229.6	247.4	30.0	224.8	252.2
Diastolic Pressure	63.5	mmHg	/	/	10.6	42.2	84.7
Systolic Pressure	127.3	mmHg	/	/	16.4	94.4	160.1
S3 Flow Velocity	2.4	m/s	/	/	0.5	1.4	2.4
Heart rate	71.2	bpm	/	/	9.7	51.7	90.6

7.2.3 Source of Uncertainty in Clinical Parameter Evaluation

Clinical assessment of S3-related performance parameters is influenced by uncertainty in the instrument accuracy and the intra-operator variability. For each quantity of interest, the level of uncertainty is assessed:

- **DD at inflow, mid and outflow levels**: S3 diameters are measured by an experienced radiologist using the medical software of the 256-row detector CT scanner used in this study. To include the uncertainty, the effect of artifacts leading to error of 5% is considered as shown in our previous work [50]. This error is used to estimate the standard deviation likely occurring in the DD measurement at CT imaging, which is 23 ± 1.3 mm.

- **EOA**: The EOA is measured by an expert cardiologist using echocardiography after TAVI procedure. Image resolution, voxel distortion and image distortion of the ultrasound probe are the main sources of uncertainty. According to literature data [80], a standard deviation of 7 mm^2 was considered for the measurement of EOA.

- **TPG**: the pressure gradient across the S3 is quantified by the echocardiographic system using Bernoulli's principles. The TPG is therefore derived by the flow jet velocity (v) across the valve at systole as $TPG = 4 \cdot v^2$. According to literature data [81], a standard deviation of 4 mmHg was considered for each measurement done by echocardiography for each patient.

7.3 UQ Approach and Sensitivity Analysis

The validation assessment finishes in the quantification of uncertainties in the distribution of model outputs, which arise from uncertainties in the model inputs. A sensitivity analysis is conducted to partition and allocate the uncertainty in the outputs across various sources of uncertainty, incorporating the probability distribution functions of the input parameters. Validation is performed through the initial development and subsequent utilization of a surrogate model for model response evaluation in UQ, owing to the high computational expense associated with quasi-MCS analysis.

7.3.1 Design of experiment

The surrogate model is developed using Latin Hypercube Sampling (LHS) to create a finite-element simulation plan consisting of 88 simulations (11 parameters × 8 random combinations of input variables). Although the optimal number of samples is typically ten to adequately capture the variability of the model inputs, a sensitivity analysis reducing the number of random combinations from ten to seven revealed no significant impact on the surrogate model predictive capability. However, the LHS method may produce unrealistic combinations of input parameters for flow boundary conditions, which need to be excluded.

7.3.2 Surrogate modeling

Following each structural analysis simulating device implantation and FSI analysis for post-TAVI flow assessment, the quantities of interest were extrapolated using a Python script integrated within Abaqus software. This approach not only automated the result analysis but also minimized potential user errors in data estimation. Several surrogate models, including the response surface method, radial basis function, and Gaussian process regression (GPR),

were evaluated using MATLAB (v2024, MathWorks, USA) to fit the simulation output parameters and assess the quality of the fit. GPR models the simulation output response as a realization of a Gaussian process, which is fully specified by a mean function $\mu(x)$ and a covariance function $k\ (x, x')$, also known as the kernel. The output $y(x)$ at any input point x is assumed to follow a multivariate Gaussian distribution:

$$y(x) \sim GP(\mu(x), k\ (x, x))$$

In the end, GPR with leave-one-out cross-validation (LOO) is adopted to approximate the response of the original numerical simulations as a function of input variables at a relatively low computational cost.

7.3.3 Probabilistic analysis and global sensitivity

Sobol sequences are employed for probabilistic MCS to sample the input space, with samples scaled to conform to the specified ranges of input variables. By repeatedly sampling from the input distributions and executing the model, the MCS generates a distribution of possible outcomes. This offers insights into the range and likelihood of various responses. The surrogate model substitutes the original numerical simulations to provide deterministic data points for the Sobol analysis.

Global sensitivity analysis is conducted using Pareto plots to identify the input parameters that most significantly influence uncertainty in the model outputs. This analysis helps to isolate the most sensitive parameters, enabling control and refinement of model variables to enhance accuracy. The total effect index (TEI) quantifies the percentage contribution of each input parameter to the total output variance, which is visualized using Pareto plots.

The TEI for a given input parameter X_i is computed as:

$$TEI(X_i) = 1 - \frac{Var(Y|X_i)}{Var(Y)}$$

where:

- $Var(Y)$ is the total variance of the output Y,
- $Var(Y|X_i)$ is the conditional variance of Y when all parameters except X_i are fixed.

7.4 Validation

Validation aims to estimate how well the model outputs correspond to real-world data, which includes determining the prediction error and associated uncertainty in the patient-specific TAVI model. This process involves comparing the model predictions to experimental or observational data to ensure that the model can accurately simulate the physical phenomena under consideration.

Model outputs, reported in paragraph 7.1, are DD, EOA and TPG. These metrics are directly related to the clinical outcomes of the TAVI procedure and are used to assess the model predictive accuracy.

The validation process requires comparing the model's outputs with a comparator. In this study, the comparator data are derived from post-TAVI CT imaging and Doppler echocardiography. Specifically, post-TAVI CT imaging is used to measure the S3 DD, while Doppler echocardiography is used to estimate the EOA and TPG across the implanted device.

For validation, the cumulative distribution function (CDF) curve of the surrogate-derived parameters is calculated. Similarly, the CDF for clinical variables is determined based on uncertainties in clinical parameter evaluations (see paragraphs 7.2.3). The CDF represents the probability that a variable will take a value less than or equal to a specified threshold. To quantitatively assess the agreement between the simulations and clinical data, the area under the model and comparator CDFs is computed (referred to as the area metric), and the percentage difference between them is determined to evaluate the model's accuracy [39].

7.5 Results

Regarding the structural deployment of S3 device, only a minimal part of simulations presented numerical failures due to unrealistic combinations of material parameters and TAVI-related procedural variables. This was not, however, observed for the n.88 post-TAVI FSI analyses for which a fraction of 8.4% to 22.7% simulations failed due to the variability in the model inputs resulting from the LHS methodology.

Figure 7.4 illustrates the predictive capability of the surrogate model based on GP regression with LOO for the quantification of the S3 device expansion across different device heights for two patients with the 23 mm and 26 mm device sizes. Specifically, the mean relative error (MRE) between surrogate model and actual finite-element values for the device

diameter is consistently lower than 1% in all patients. Low LOO mean squared errors (RMSE) and high correlation coefficient (R) were also found for all models as reported in Table VI. However, the response of the trained surrogate model highlighted lower effectiveness in capturing the bioprosthesis hemodynamic response estimated with actual FSI outputs (see Figure 7.5).

***Table VI**: Fitting response of the surrogate model response of each model parameter for both 23-mm and 26-mm S3 devices. LOO RMSE = LOO root mean square error; R = correlation coefficient; MRE = mean relative error.*

		23-mm S3 device		**26-mm S3 device**	
		Case #1	**Case #2**	**Case #3**	**Case #4**
Inflow Diameter					
	LOO RMSE	0.004	0.011	0.001	0.002
	R^2	0.98	0.99	0.99	0.98
	MRE (%)	0.22	0.41	0.10	0.15
Mid Diameter					
	LOO RMSE	0.001	0.014	0.001	0.001
	R^2	0.97	0.98	0.99	0.91
	MRE (%)	0.58	0.48	0.09	0.43
Outflow Diameter					
	LOO RMSE	0.006	0.003	0.001	0.001
	R^2	0.96	0.98	0.98	0.99
	MRE (%)	0.26	0.19	0.09	0.08
EOA					
	LOO RMSE	12.678	29.404	26.155	46.788
	R^2	0.96	0.94	0.97	0.92
	MRE (%)	2.07	4.37	8.45	11.83
TPG					
	LOO RMSE	32.156	34.901	16.583	28.990
	R^2	0.91	0.93	0.86	0.89
	MRE (%)	24.53	15.96	15.70	22.17

Figure 7.6 and Figure 7.7 display the Pareto plots of input parameters on output uncertainties for the device diameter at three cross-section levels and flow parameters for the 23 mm and 26 mm stent frames, respectively. Blue bars indicate positive association of the uncertain parameter with the quantity of interest whilst red bars display negative correlation with the model output variable. Pareto plots of other two cases are shown in Appendix I.

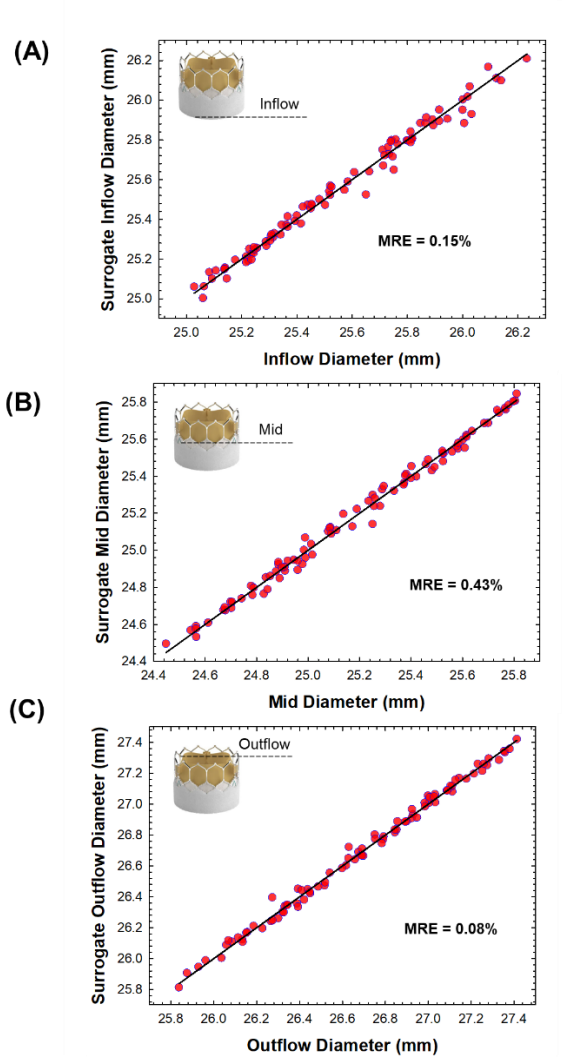

***Figure 7.4**: Correlation between the surrogate model response and actual structural numerical predictions of the device diameter at (A) inflow, (B) mid and (C) outflow levels for Case #4 model with the 26 mm S3 device.*

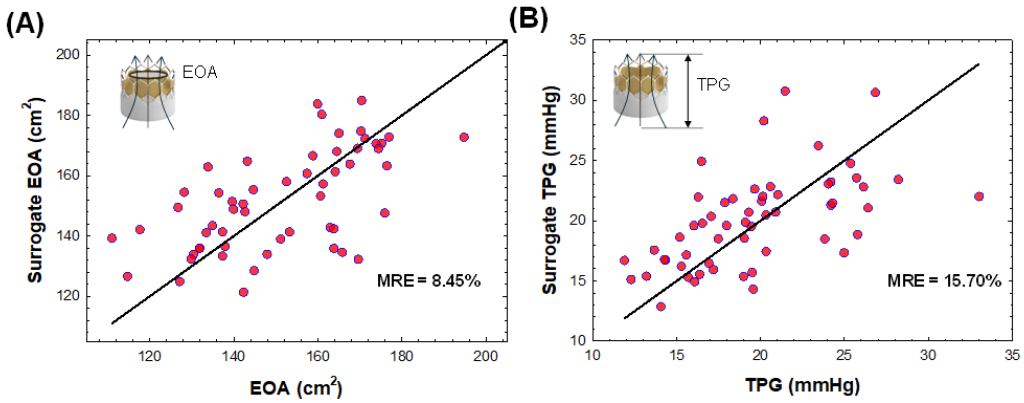

***Figure 7.5:** Correlation between the surrogate model response and actual FSI predictions of the (A) EOA and (B) TPG of the 26 mm S3 device for Case #3 model.*

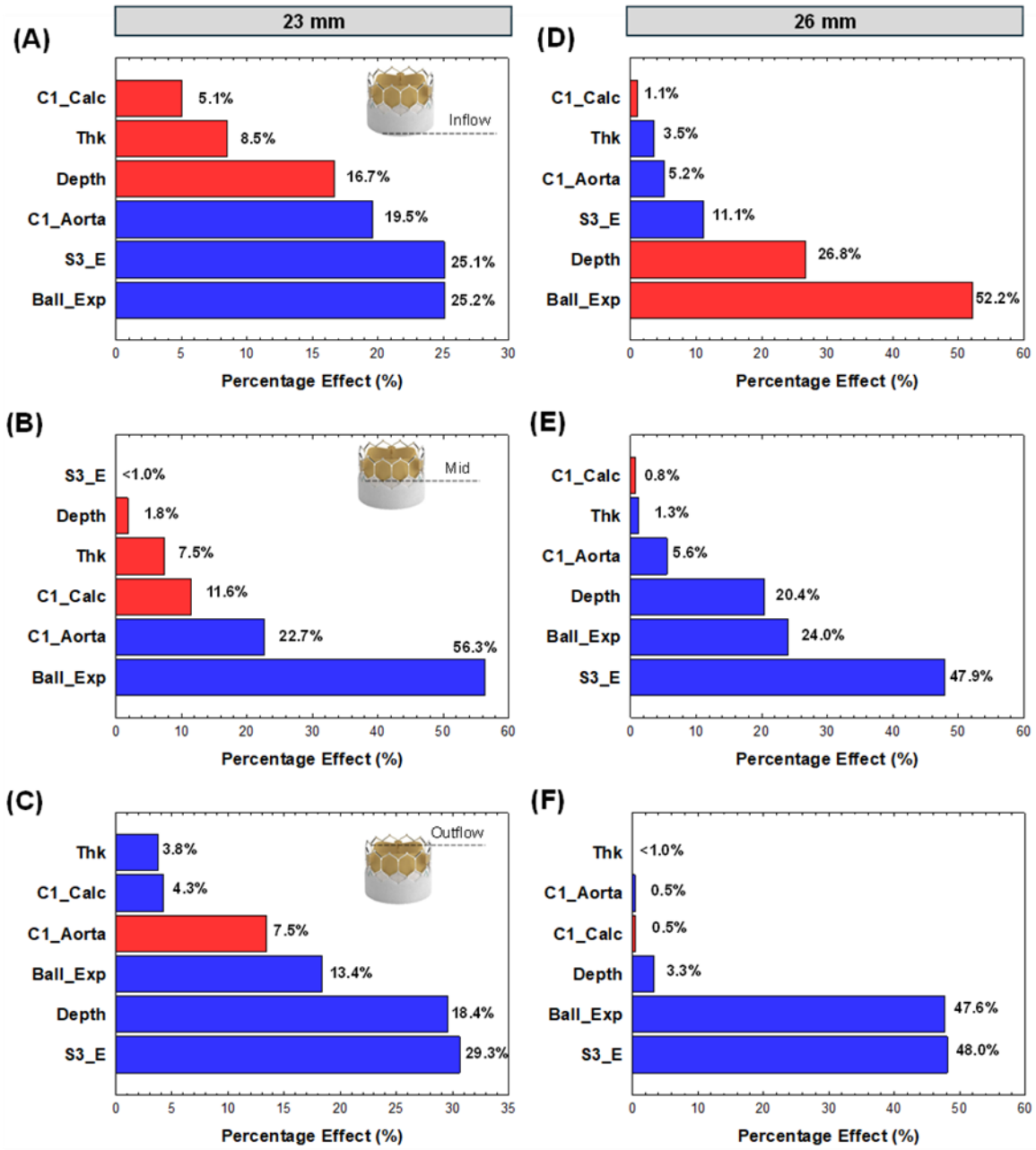

***Figure 7.6**: Pareto plot showing sensitivity of model inputs on the output device diameter for the 23 mm S3 device (Case #1) and 26 mm S3 device (Case #3) at different cross-sections (A-F); Note: Ball_Exp = balloon expansion; C1_Calc = Neo-Hookean material parameter of calcification; C1_Aorta = Neo-Hookean material parameter of aortic wall; Depth = implantation depth; S3_E = Young's modulus of S3 device; Thk = aortic wall thickness.*

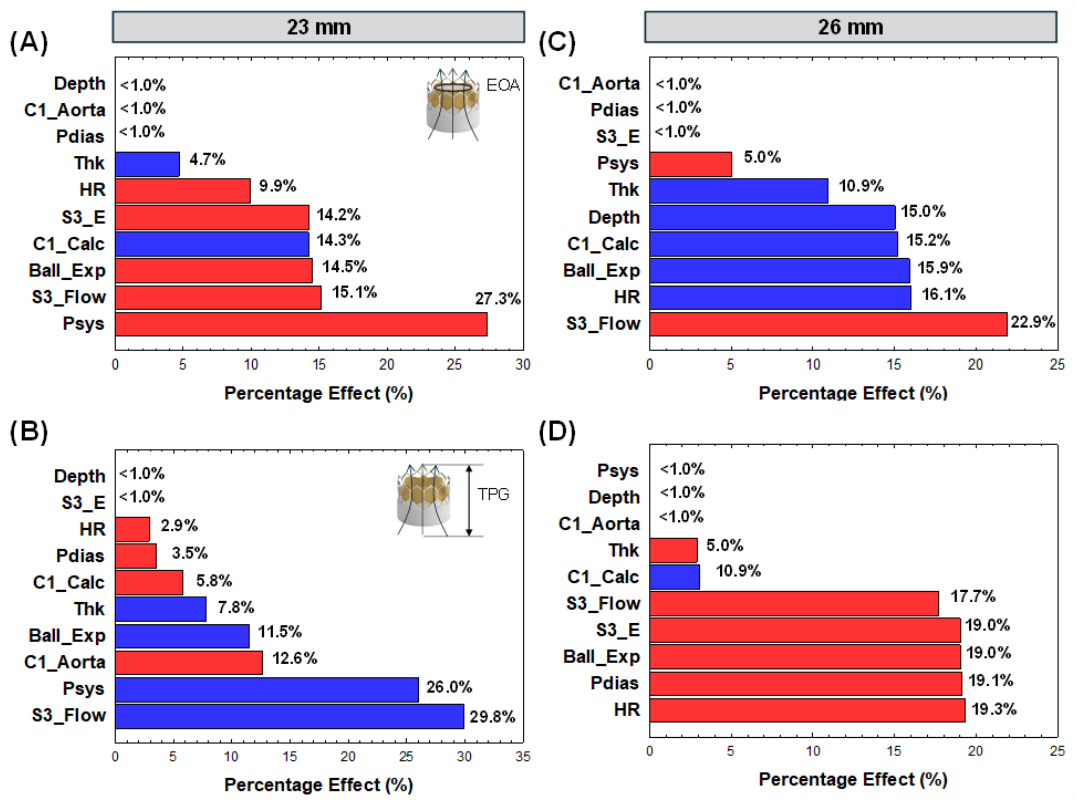

***Figure 7.7**: Pareto plot showing sensitivity of model inputs on both EOA and TPG device (A-D) diameter for the 23 mm S3 device (Case #1) and 26 mm S3 device (Case #3); Note: Ball_Exp = balloon expansion; C1_Calc = Neo-Hookean material parameter of calcification; C1_Aorta = Neo-Hookean material parameter of aortic wall; Depth = implantation depth; HR = heart rate; Pdias = diastolic pressure; Psys = systolic pressure; S3_E = Young's modulus of S3 device; S3_Flow = S3 flow velocity; Thk = aortic wall thickness.*

Global sensitivity analysis revealed that the device adaptation to the stenotic aortic valve is primarily influenced by the balloon expansion and the medical device elastic material modulus. Only for one patient case with the 23 mm device, the implantation depth was found as the key player of the device biomechanical response with sensitivity index of 32.4% at the outflow diameter. The uncertainty in the Young Modulus of S3 device was the most influential parameter with percentage effect ranging from 29.3% to 48%. Less consistent influence of uncertain parameters on the model-related fluid-dynamic response was observed. Sensitivity indexes highlighted that blood pressure, heart rate and the transaortic flow jet are the most influential parameters of the post-TAVI hemodynamic. For the 23 mm device, as an example, a 16.4 mmHg deviation of the mean systolic pressure values may result in 27.3% variation in the prediction of the EOA. Similarly, a 0.5 m/s deviation of mean S3 flow velocity may lead to a change of nearly 30% in the TPG estimates.

Figure 7.8 and Figure 7.9 show the clinical and in-silico CDF curves for all investigated quantities of interest together with the corresponding area metric for two patients with different devices sizes. The validation criterion (ie, area metric ≤5%) was observed in the majority of device diameter predictions. Out of 12 assessments (ie, 3 device height and 4 patients), only three cases had a level of agreement higher than the 5% acceptance threshold with the highest area metric of 13.0% for the patient with the 23 mm device. Both clinical and in-silico CDF curves showed a steep rise, which indicated that the diameter values are tightly clustered around a specific range. In a different way, the discrepancy between clinical and in-silico predictions was remarkably higher for both the EOA and TPG hemodynamic parameters as compared to diameter-related CDFs. Only in one patient with the 23 mm device size, the 5% acceptance threshold was found for the TPG parameter. CDFs of other two patients are shown in Appendix II.

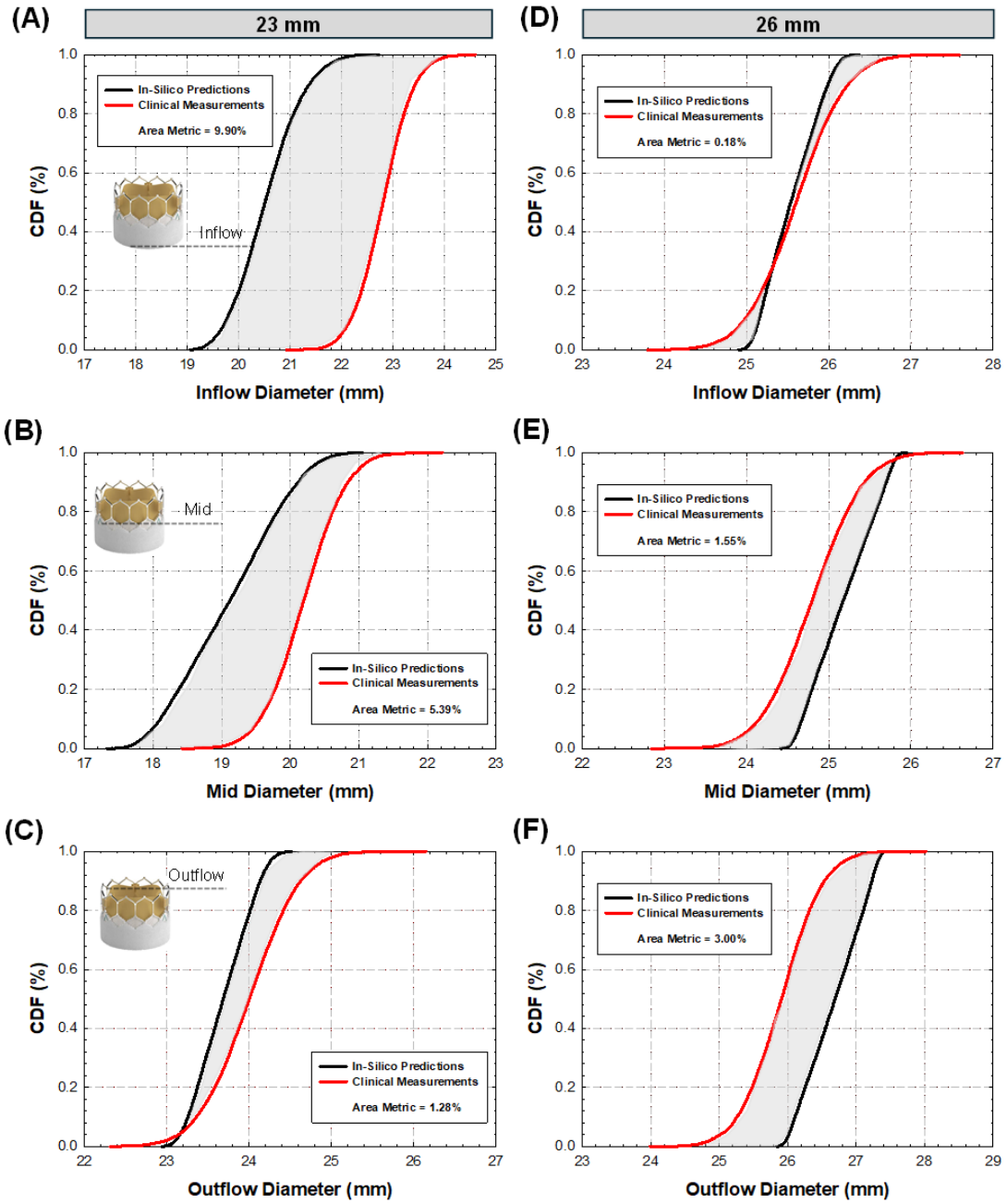

***Figure 7.8**: CDF curves for both clinical and in-silico data of the device diameter showing the area metric and its value confined by the two CDF curves (grey area) computed for both 23 and 26 mm S3 devices of Case #1 (A - B - C) and Case #3 models (D - E - F).*

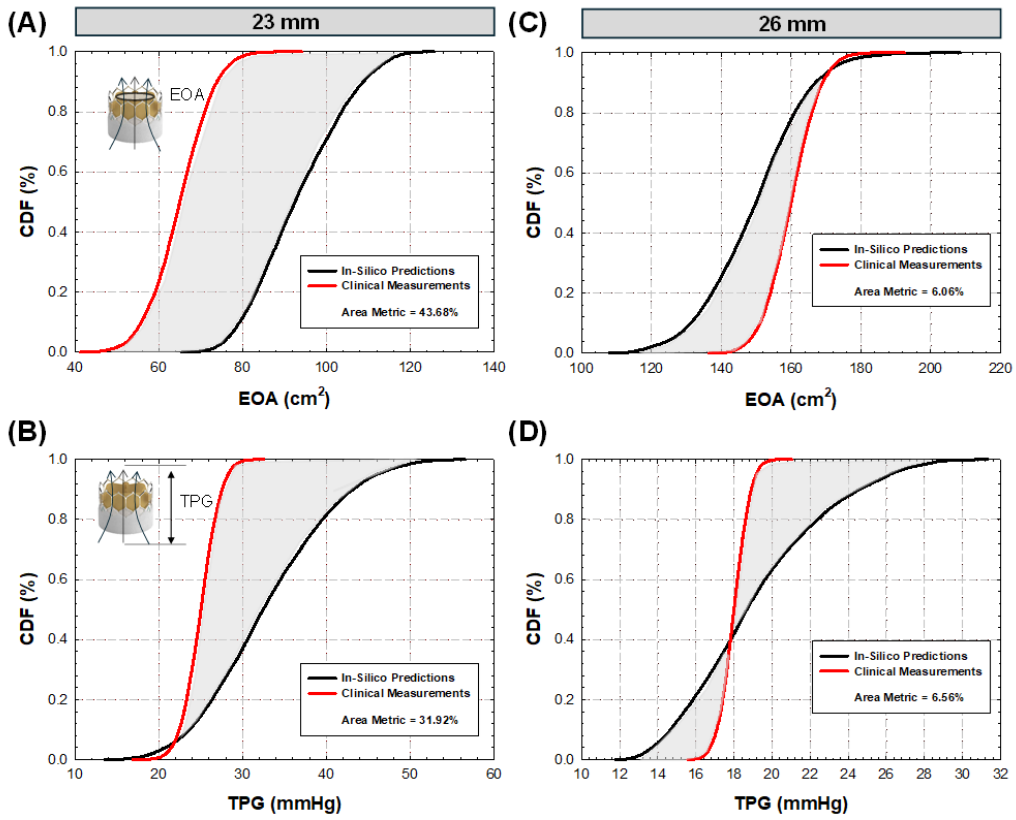

***Figure 7.9**: CDF curves for both clinical and in-silico data of both EOA and TPG showing the area metric and its value confined by the two CDF curves (grey area) computed for both 23 and 26 mm S3 devices of Case #1 (A – B) and Case #3 models (C - D).*

7.6 Discussion and conclusion

In this chapter was described our application of ASME V&V 40 framework to assess uncertainty in patient-specific TAVI modeling, evaluating both model rigor and associated risks. UQ encompassed anatomical and material properties, physiological conditions, and procedural variables. The findings confirm the model robustness in predicting the structural response of the medical device, supporting its reliability for in-silico safety-critical decisions. However, the model predictive accuracy for post-TAVI hemodynamics requires careful attention, as discrepancies of up to 43.68% exceeded acceptance criteria. These differences cannot be only attributed to poor predictive capability but rather to the evaluation criteria and methodologies used to measure the investigated quantities of interest. Nonetheless, this approach advances the standardization and validation of in-silico models for medical devices.

Sensitivity analysis indicated that the biomechanical response of the aortic root after device implantation was mainly affected by balloon inflation and the elastic properties of the

medical device material. The manual management of fluid expansion by the interventional cardiologist via a syringe is crucial in establishing the final configuration of the device. In clinical practice, deviating from the manufacturer's specifications for the filling of the balloon delivery system is common; yet, quantifying its effect on the final device diameter by post-TAVI surveillance imaging remains challenging [82]. The second most significant input parameter was the Young's modulus of the medical device, which proved to be the most crucial material property in the patient-specific TAVI model. This finding is significant, as the majority of research has concentrated on enhancing tissue wall models to elucidate ideal material properties using imaging data [71] or investigating material behavior via different constitutive relationships [19]. Conversely, Finotello et al. [83] aimed to elucidate the impact of device material characteristics, demonstrating that material uncertainty in self-expandable devices might result in erroneous estimates of tissue wall stress values.

There was significant variation in the sensitivity indices with respect to the fluid-dynamic response. Two factors may elucidate the difference. First, the EOA and TPG metrics were assessed immediately the structural heart intervention in the hybrid operating room while the patient was still anesthetized. The observed patient's behavior differed from the model because the simulations relied on stochastic limitations of hemodynamic parameters obtained from the physiological norms of the overall patient population.

The validation activity, based on CDFs and the area measure, raises numerous key questions about the rigor of the patient-specific TAVI model. The 5% acceptance level for comparing simulated and observed data represents a stringent criterion, especially considering the inherent inter-subject variability in human physiology. The suggested validation study implicitly assumes that all model inputs are affected only by measurement errors; nevertheless, certain inputs may represent population-based features instead of individual-specific data. In a prior work [50], we demonstrated a low interclass correlation coefficient in post-TAVI CT imaging assessments of the S3 device between expert and non-expert radiologists. The intra-observer variability in evaluating EOA and TPG using echocardiography frequently exceeds that noted for CT-derived diameter values, as indicated by Calleja et al [84].

The area metric accurately identifies variance discrepancies between clinical and computational results, even when their mean values are comparable. Nevertheless, when clinical and simulation outcomes diverge, as evidenced by the significant disparities in CDFs

for EOA and TPG, the area metric may exhibit diminished sensitivity to variations in differences. Despite these considerations, the area metric values obtained for our patient-specific TAVI model exhibit strong concordance between in-silico and in-vivo data.

Chapter 7 implemented a risk-informed credibility assessment of the patient-specific TAVI model according to ASME V&V40. The model was classified as high risk, requiring a stringent level of verification, validation, and uncertainty quantification.

Sensitivity analysis showed that structural outputs were mainly influenced by device and expansion parameters, while hemodynamic results were more sensitive to physiological boundary conditions. Structural predictions demonstrated good agreement with clinical data, whereas larger variability was observed for flow parameters. These differences between computational and clinical flow parameters (EOA and TPG) may arise from both modeling assumptions and measurement variability. Clinically, these metrics are indirectly estimated using Doppler echocardiography, introducing approximation and operator-dependent uncertainty. In contrast, the computational model directly computes pressure and flow fields but relies on simplified boundary conditions.

To conclude, the work presented establishes a systematic and rigorous framework for assessing model credibility and supporting the integration of patient-specific simulations in clinical decision-making.

Chapter 8

8. Parametric Analysis of redo-TAVI Configurations

This chapter examines the hemodynamic and structural implications of performing TAVI within a previously implanted transcatheter heart valve (redo-TAVI or TAVI-in-TAVI). As TAVI is increasingly offered to younger patients with longer life expectancy, the likelihood of valve degeneration and the need for redo-TAVI procedures is expected to rise. Although the implantation of a second THV represents a minimally invasive alternative to surgical replacement, the permanent displacement of the first THV leaflets and stent frame can compromise coronary access and potentially obstruct coronary perfusion [62].

In this context, computational modeling provides a powerful tool to explore the effect of device selection and implantation strategy on coronary hemodynamics. By combining FEA of device deployment with FSI simulations of coronary flow, it becomes possible to identify anatomical and procedural configurations that predispose to obstruction.

This chapter presents a parametric analysis of redo-TAVI configurations in a patient-specific setting, with variation of implantation depth and device sizing. The objective is to establish quantitative relationships between valve-to-coronary (VTC) distance and post-procedural coronary flow, providing a mechanistic basis for pre-procedural risk stratification.

8.1 Clinical rationale and risks of coronary flow obstruction

The long-term durability of THVs remains a challenge, as biological leaflets are subject to progressive degeneration via calcification, thrombosis, and fibrotic remodeling. Registry data suggest that structural valve deterioration can occur within 5 - 10 years post-implantation, particularly in younger patients. In such cases, redo-TAVI is often preferred over surgical explantation.

However, redo-TAVI carries unique risks. The second device displaces the first THV's degenerated leaflets against its metallic stent frame, creating a tubular structure that may extend into the sinuses of Valsalva or above the sino-tubular junction. This configuration can narrow the anatomical space available for coronary flow and complicate future coronary access. Imaging-based studies have demonstrated that up to 25% of patients may be at risk of coronary obstruction following redo-TAVI with tall self-expanding frames, while as many as 80% may experience restricted coronary access in subsequent procedures.

Current pre-procedural assessments rely on morphometric parameters such as sinus diameter, coronary ostium height, and leaflet length, but these metrics do not fully capture the complex interaction between device frames, displaced leaflets, and the coronary ostia. Computational modeling addresses this gap by integrating device - host interactions into the risk assessment process.

8.2 FEA of S3-Evolut deployment

8.2.1 Patient-specific model

The computational model was based on a 68-year-old patient who had previously undergone implantation of a 23-mm S3 THV, which degenerated due to leaflet thrombosis and reduced motion. A subsequent redo-TAVI procedure with a 29-mm Evolut PRO device was performed. Patient-specific anatomy was reconstructed from ECG-gated CT scans at three stages: pre-TAVI, post-initial TAVI, and post-redo-TAVI. The aortic root, calcifications, and native/bioprosthetic valve leaflets were segmented using Mimics and Rhinoceros software.

8.2.2 Structural modeling

The structural heart intervention was simulated using FEA with Abaqus/Explicit software (v2021hf7, Dassault Systèmes, USA). To model the dynamic phenomenon, we used a quasi-static FEA approach that ensured the kinetic to internal energy ratio remained below 10%. This was achieved through a mass scaling technique using a stable time increment and thus reducing the computational cost. In addition, a penalty contact algorithm with a friction coefficient of zero was used to enable contact during simulations.

Bioprosthesis models were meshed with structured hexahedral elements [20, 23]. Stainless steel with bilinear elasto-plastic material and superelastic Nitinol alloy (14 constants user material [19]) were employed to model the S3 and Evolut PRO, respectively. The device sealing skirt was considered closing the cell geometries of each stent frame with several surfaces modelled at mid-thickness of each device frame. For the S3, all cell-structs of the THV frame were closed to mimic the displaced shape of valve leaflets as seen in TAVI-in-TAVI. This surface, which represents the device skirt and leaflets, was modelled at the crimped phase of S3 deployment in the human model. For the Evolut PRO, the skirt was included at end of TAVI-in-TAVI simulation by mapping the skirt surface on the stent frame

and resolving potential overclosure by strain-free adjustments analysis in Abaqus\Explicit. Skirts were meshed with triangular membrane elements with a thickness of 0.1 mm and were then connected to the device frame using tie contact conditions.

Crimping of SAPIEN 3 under frictionless contact conditions was carried out using a cylindrical surface gradually moved along the radial direction from the initial device diameter of 23 mm to the final diameter of 6 mm. Then, the SAPIEN 3 Ultra device was placed in the patient-specific model with an implantation depth of 5 mm whilst a restart analysis was considered to account for the stress state resulting from the crimping numerical analysis. For the sake of simplicity, expansion of SAPIEN 3 Ultra THV was performed by radially displacing a cylindrical surface representing the wall of the expanding balloon. Expansion was obtained by enlarging the balloon surface upon the device nominal diameter of 23 mm (Figure 8.1 A-C).

After deploying the SAPIEN 3 Ultra, the Evolut Pro was positioned in the post-TAVI model with an implantation depth of 9 mm and was then crimped with an approach similar to that of first device. By pulling the sleeve towards the distal ascending aorta and releasing the device, the Evolut Pro stent was gradually deployed into the first device to mimic the TAVI-in-TAVI (Figure 8.1 D-F).

A parametric analysis of the redo-TAVI procedure was carried out by varying the implantation depth and device size with respect to the baseline model Figure 8.2. The following scenarios were therefore explored:

- 5-mm implantation depth for the 23-mm SAPIEN 3 Ultra and 9-mm implantation depth for the 29-mm Evolut Pro (ie, the S3-in-Ev) - reference model as clinically done by the Heart Team.
- 5-mm implantation depth for the 23-mm SAPIEN 3 Ultra and 16-mm implantation depth for 29-mm Evolut Pro (ie, the S3-in-EvL) - low TAVI-in-TAVI implantation.
- 2-mm implantation depth for the 23-mm SAPIEN 3 Ultra and 9-mm implantation depth for the 29-mm Evolut Pro (ie, the S3H-in-Ev) - high TAVI implantation.
- 5-mm implantation depth for the 23-mm SAPIEN 3 Ultra and 9-mm implantation depth for the 26-mm Evolut Pro (ie, the S3-in-Ev26) - device undersizing of TAVI-in-TAVI.

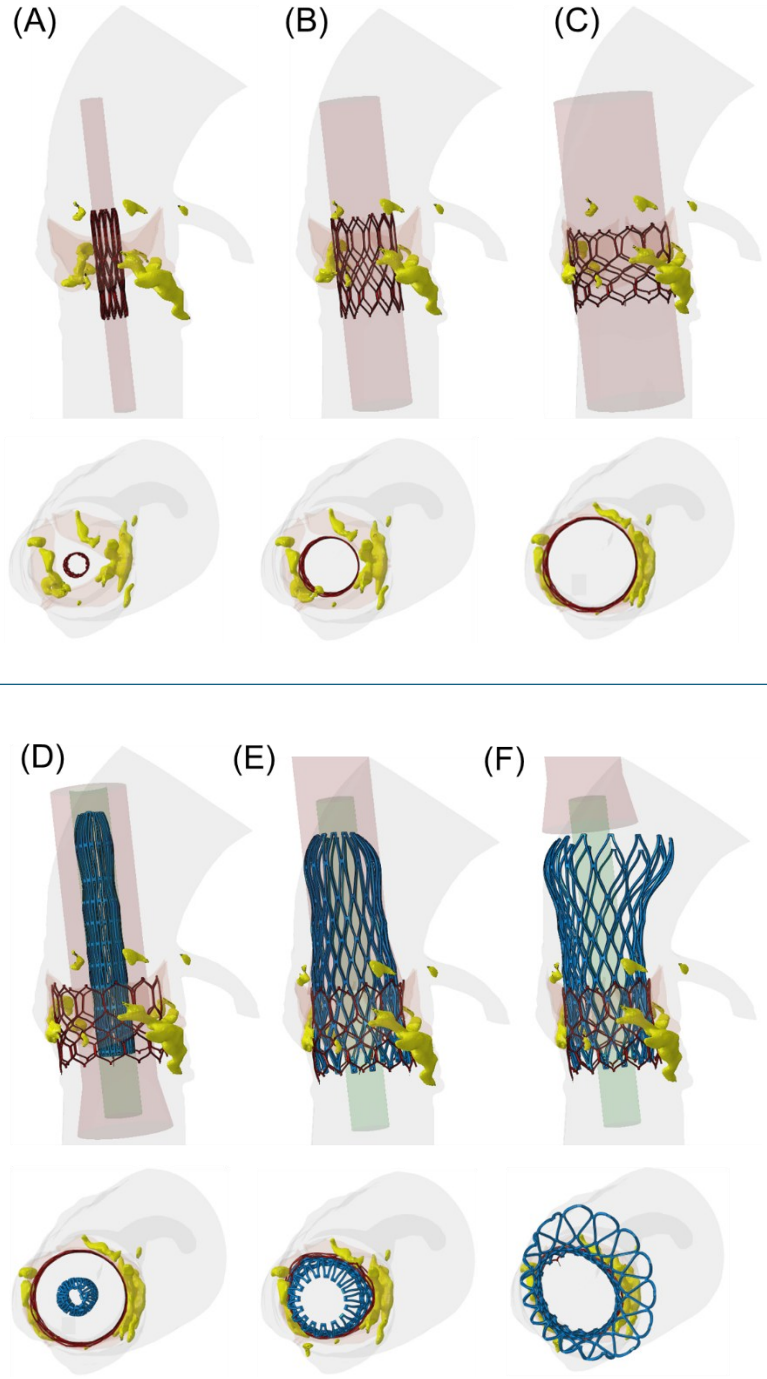

***Figure 8.1**: Different steps of S3 deployment from crimped configuration (A) to final implant (C); Different steps of Evolut PRO deployment from crimped configuration (D) to final implant (F).*

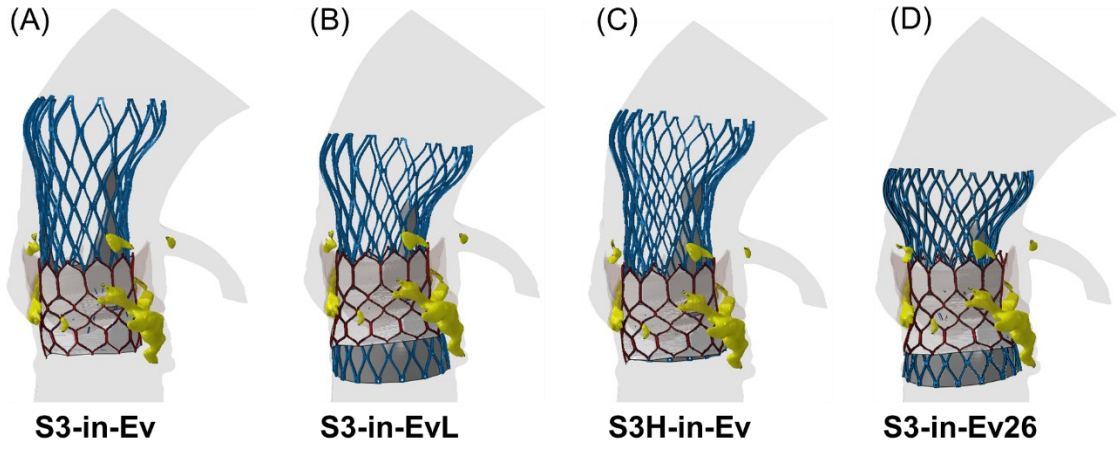

Figure 8.2: *Deformed shapes of redo-TAVI for (A) baseline model, (B) low Evolut Pro implantation depth, (C) high S3 implantation depth, (D) Evolut Pro undersize.*

For each scenario VTC distance was quantified, defined as the minimum distance between the deployed valve - leaflet complex and the coronary ostia. Separate measurements were obtained for the left main and right coronary arteries. VTC distance was extracted to serve as a predictor of coronary obstruction risk and compared with the VTC distance measured on CT-scans in order to test also the credibility of the computational models.

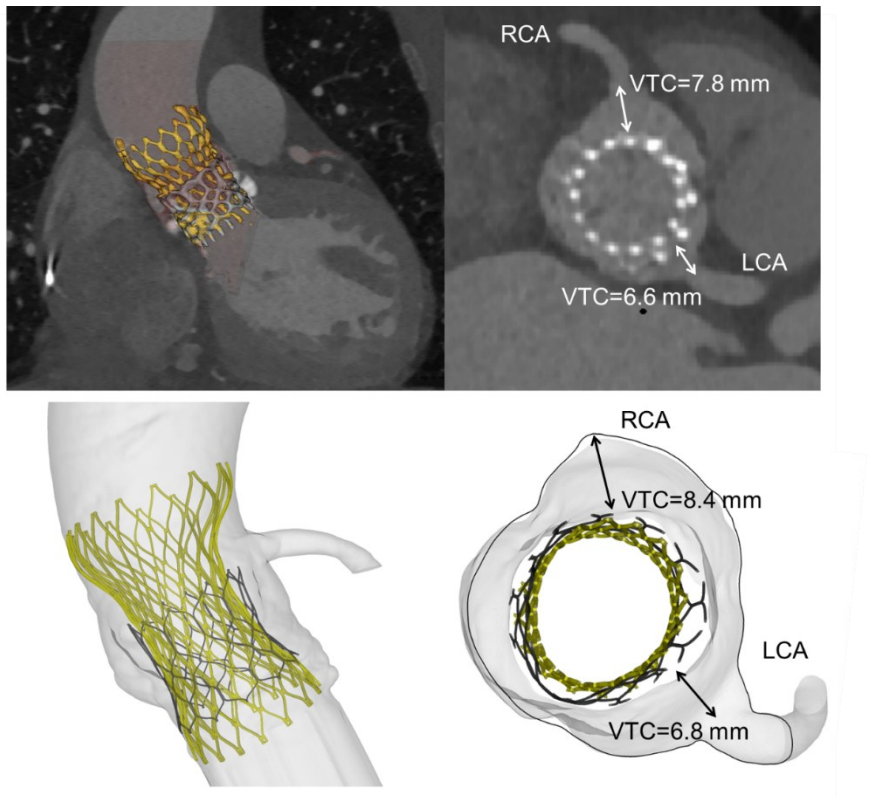

Figure 8.3: *VTC distance calculations from CT images and simulation outputs.*

Simulations demonstrated that deeper implantation systematically reduced the VTC distance by forcing the nitinol frame closer to the coronary ostia. Oversizing the second device produced similar effects through radial overexpansion. Scenarios combining deep implantation and oversizing resulted in the most critical reductions, with VTC distances shortened by more than 30% relative to the baseline case, highlighting the risk of coronary obstruction.

8.3 Hemodynamic Assessment through FSI

After the redo-TAVI simulation, the SPH modeling approach was used to quantify flow circulating in coronary arteries. The blood was modelled as a Newtonian fluid characterized by a density of 1060 kg/m^3 and viscosity of 0.0035 Pa*s, using the pressure-density relation governed by the linear Hugoniot equation of state (artificial sound speed of c0=145 m/s). For particle discretization, the fluid domain confined by the aortic lumen was meshed with unstructured tetrahedral elements for all redo-TAVI configurations. Flow motion was generated by pressure boundary conditions exerted on the fluid volume by several rigid plates located at the proximal and distal ends of the aortic wall and coronary arteries [20]. This allowed the development of a transmural pressure gradient across the device valve leaflets according to physiological pressure waveforms generated by the beating heart. Tie contact conditions were developed between the fluid and rigid plates to avoid separation among parts. This allowed the transfer of the pressure applied to each rigid plate in fluid motion. Using a predefined field in Abaqus, an initial fluid pressure of 80 mmHg was set for the SPH particle. For coronary arteries, the rigid plates were loaded with a pressure waveform identical to that of the distal aortic wall. However, we did not consider the systolic increase in hydraulic resistance of the coronary circulation. The proximal end of the aortic wall and coronary arteries was extended 5-fold the annulus diameter to reduce transient effect during the simulated cardiac beat (time step of 0.8 s). The cardiac output was 5 L/min assuming a systolic time of 0.3 s. The general contact algorithm in Abaqus/Explicit enabled the FSI interaction between fluid particles and device valve leaflets.

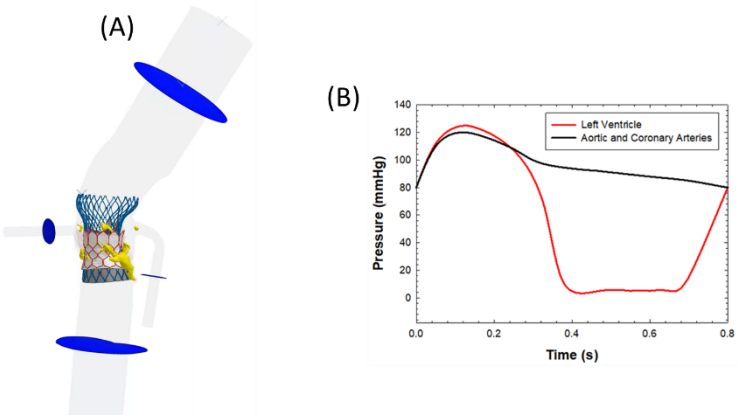

***Figure 8.4**: (A) SPH model with the aortic wall, extension and rigid plates for applying the boundary conditions; (B) Pressure boundary conditions applied to each plate for simulating fluid motion.*

For post-processing, particle flow data were mapped on a solid tetrahedral element mesh of the fluid domain to analyze flow velocity in contour map instead of discrete particle point collection.

The flow velocities over the cardiac beat were analyzed to investigate the flow circulating in the coronary arteries after redo-TAVI (Figure 8.5). During peak systole, a central flow jet from the opened device valve leaflets was observed while high flow velocities were noted at the end of the deceleration phase when the valve is almost closed. Mid-diastole showed the phase with the most pronounced coronary flow circulation (see Figure 8.5 E). A region of high flow velocities was observed above the LCA ostium, suggesting that the increased flow velocity is likely due to a narrowing region confined by the aortic wall and the Evolut device skirt. The alignment of the leaflet commissures of Evolut Pro with those of the native aortic valve ensured coronary circulation, thereby reducing the effect of the tall device skirt on coronary obstruction.

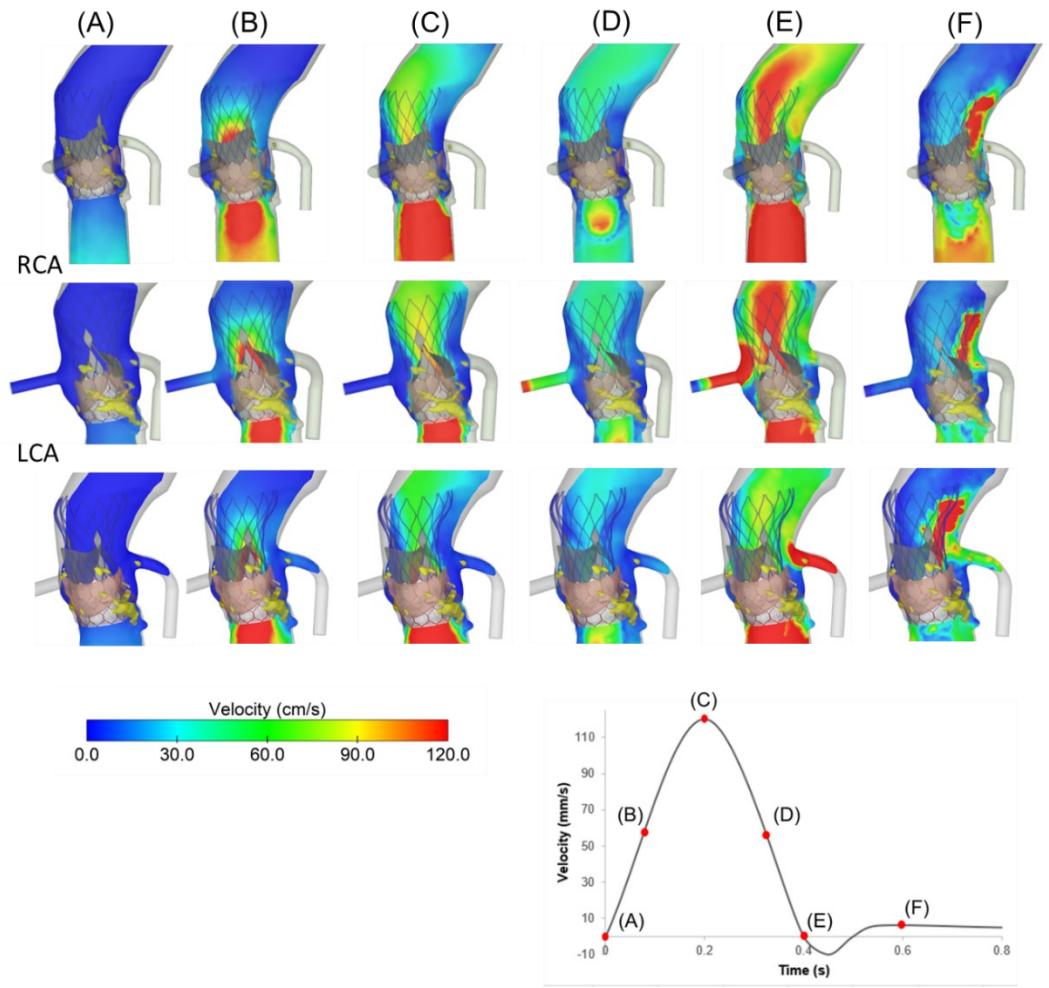

***Figure 8.5**: Flow velocities for the baseline model at different cardiac phases (A - F); velocities in right coronary artery and left coronary artery are shown.*

Figure 8.6 depicts the map of flow velocities at early-diastole (ie, just before valve closure) for various implantation scenarios. The S3-in-Ev26 model had lower coronary flow velocities than those observed in other models, likely due to the marked device size. The model with low implantation depth of Evolut PRO in the S3 device (ie, S3-in-EvL) highlighted high coronary flow velocities, while the model with high implantation depth for the first device mainly altered the flow velocity of the RCA vessel.

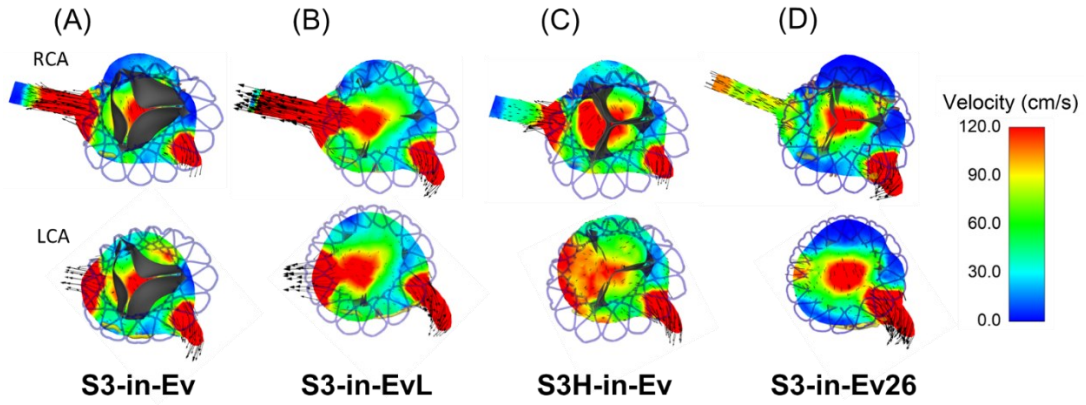

***Figure 8.6**: Flow velocities in the axial view for various redo-TAVI; (A)baseline model, (B) low Evolut Pro implantation depth, (C) high S3 implantation depth, (D)Evolut Pro undersize at early diastole just before valve closure.*

8.3.1 Relationship between VTC distance and flow reduction

Figure 8.7 A illustrates the coronary flow percent changes for different models. A reduction of coronary flows was observed for the S3-in-Ev26 model as compared to the pre-TAVI stage. For the reference configuration (ie, S3-in-Ev), the LCA flow was reduced to 60% with respect to pre-TAVI model, while the RCA flow remained relatively unchanged. At Pearson correlation, a strong positive linear relationship of coronary flow percent with the VTC distance was observed (see Figure 8.7 B). The VTC distance from the device frame to the LCA ostia was positively correlated with LCA flow (R=0.86 and p=0.032), while the correlation between VTC distance and RCA coronary flow was stronger (R=0.93 and p=0.014).

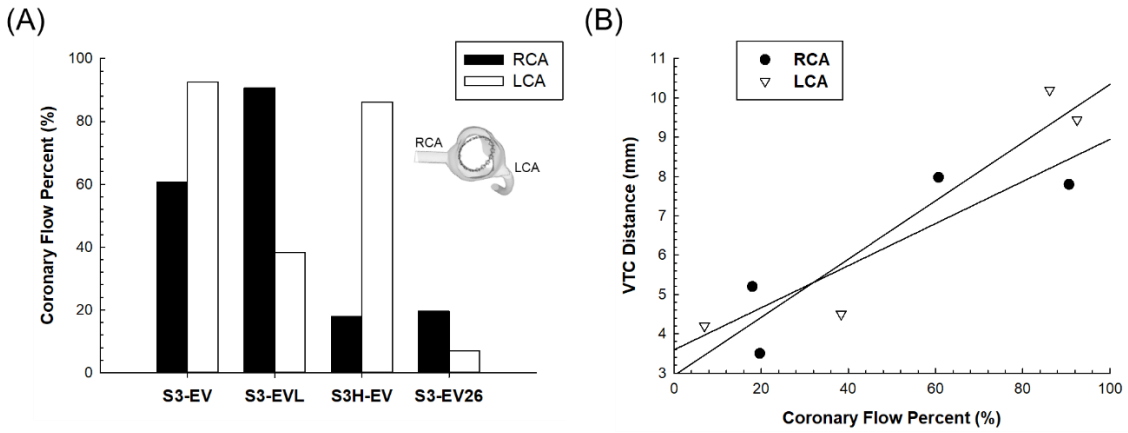

***Figure 8.7**: (A) Comparison of coronary flow percent between RCA and LCA in different implantation configurations; (B) linear regression analysis between coronary flow percent and VCT distance.*

8.4 Discussion and conclusion

In this chapter computational modeling was used to investigate the impact of redo-TAVI on coronary flow as the placement of the second prosthetic valve in the degenerated device can cause changes in the hemodynamics of the aortic root. The parametric analysis we conducted revealed that variations in the implantation depth or device undersize can alter the flow circulation compared to pre-TAVI flow analysis. We also discovered that the VTC distance, used as a pre-procedural metric for patient risk stratification, correlates with the amount of flow circulating in the coronary arteries. While this study is limited to this specific patient case, the identification of design and positioning strategies that optimize coronary flow has the potential to enhance the clinical outcomes of redo-TAVI procedures and mitigate the risk of adverse events.

Coronary artery obstruction is four times more common for valve-in-valve deployment when compared to traditional TAVI, as the leaflets of the degenerated THV become tilted vertically by the second device, creating a cylindrical covered stent frame [85]. Thus, redo-TAVI may be unfeasible in a significant proportion of patients, especially those treated with a tall frame like the Evolut Pro during the initial procedure. To minimize the likelihood of coronary obstruction, safety imaging guidelines based on geometric factors of the patient's aortic root were introduced [86, 87]. For THV in failed aortic bioprostheses, a short VTC distance evaluated by CT (< 4 mm) was found as a predictor of complications in redo-TAVI [88]. The permanent displacement of the first implanted THV may lead to coronary obstruction with a mechanism similar to transcatheter mitral valve replacement, where the device displaces permanently the anterior mitral valve leaflets towards the intraventricular septum [73, 89]. This leads to a narrowing of left ventricular outflow tract, which can ultimately lead to hemodynamic impairment. For this reason, Khan et al. [90] have proposed a percutaneous treatment using an electrosurgical catheter to lacerate the pericardial tissue of the first device and thus restore the coronary access. This solution was indeed elaborated on the basis of the LAMPOON procedure [91], which lacerates the anterior mitral valve leaflet to prevent outflow obstruction in transcatheter mitral valve replacement. During diastole, coronary perfusion is reliant on the pressure drop between the myocardial tissue and the coronary ostia of the aortic root wall. The flow field near the device closing valve leaflets and coronary resistance have been shown to impact this pressure difference, as demonstrated by Wald et al. [38].

Several computational studies have examined the effects of various procedural factors on TAVI configuration, including the implantation depth and tilt angle [25], the utilize of self-expanding devices [23, 92] or balloon-expandable devices [21]. Additionally, simulations were used to examine the efficacy and safety of TAVI in patients at high risk or with bicuspid aortic valves [20, 93]. However, there remains a dearth of computational studies focused on evaluating coronary flow in TAVI procedures.

Our findings indicate that there is a positive correlation between VTC distance and coronary flow (i.e., the larger the VTC distance, the higher the coronary flow). This relationship is reasonable since patient geometry was not altered in this study, and thus the impact of sinus anatomy on coronary obstruction was not considered.

While Chapter 8 explored a parametric analysis of redo-TAVI configurations, examining how variations in implantation depth and prosthesis size influence device interaction and coronary flow, the following Chapter 9 focuses on a novel transcatheter strategy aimed at improving redo-TAVI outcomes. Specifically, this chapter investigates a procedure in which the leaflets of the first implanted THV are explanted prior to deploying the second valve, with the objective of enhancing expansion of the new prosthesis and reducing the risk of coronary obstruction.

Chapter 9

9. Transcatheter Leaflet Resection prior to redo-TAVI

This chapter explores the concept of transcatheter leaflet resection as a strategy to overcome the challenges of redo-TAVI. With the expansion of TAVI to younger patients and those with longer life expectancy, the likelihood of repeat interventions is rising.

One of the major challenges in redo-TAVI interventions is the interaction between the new THV and the previously implanted device, particularly when the first valve has undergone structural degeneration. Calcification of the degenerated TAVI leaflets can lead to asymmetric expansion of the second valve, resulting in suboptimal hemodynamic performance, increased paravalvular leak, and altered coronary flow dynamics. To address these challenges, novel strategies such as leaflet resection prior to second-valve implantation have been proposed to enhance the expansion and function of the new device [94, 95].

In this study, a patient-specific computational approach was used to evaluate the biomechanical and hemodynamic performance of a redo-TAVI procedure with and without leaflet resection. FEA and SPH simulations were employed to assess the expansion, eccentricity, and hemodynamic efficiency of a second S3 or Evolut PRO valves implanted inside a previously deployed S3. By comparing standard redo-TAVI implantation with a scenario in which the calcified leaflets of the first valve were virtually resected, this study aims to provide insights into the mechanical and fluid dynamic advantages of leaflet removal in redo-TAVI procedures.

9.1 Clinical motivation and technological innovation

Redo-TAVI is associated with distinct mechanical and hemodynamic challenges compared with native TAVI. The previously implanted valve introduces a rigid cage and degenerated leaflets that modify the compliance of the aortic root and alter coronary access. Calcification in particular leads to localized resistance against frame expansion, resulting in bulging at inflow or outflow levels and incomplete stent - wall apposition. These features have been linked to higher transvalvular gradients and reduced EOA.

Leaflet resection aims to eliminate this barrier by mechanically removing calcified valve tissue while preserving the structural support of the skirt and commissures.

From a procedural standpoint, the System is conceived with three main components working in different successive phases.

1. A *Temporary Valve* is opened into the degenerated THV, ensuring hemodynamic support and stabilizing the patient throughout the procedure
2. *The Grasping System*, part of the Temporary Valve stent, can capture the three degenerated leaflets with one mechanical movement (managed by the delivery system handle). At the same time, grasping ensures coaxial traction of the leaflets during the resection.
3. The *Resection System* grants the mechanical cut of the three leaflets, leaving a small tissue margin between the commissures, which are used to anchor the new TAVI. *(this procedure belongs to a patent – with permission of Tresquare technologies)*.

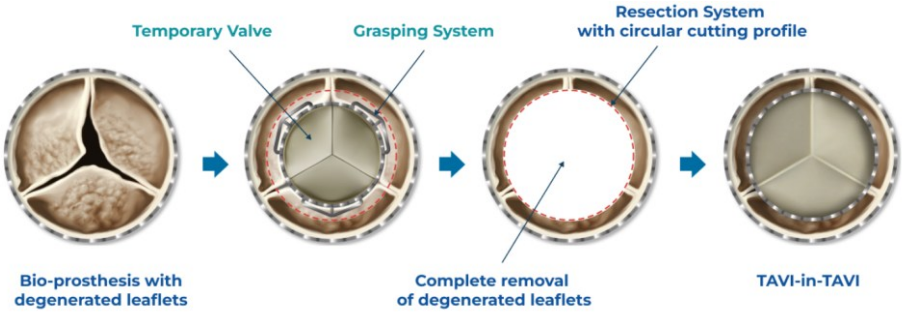

***Figure 9.1**: Resection procedure workflow. This procedure belongs to a patent, with permission from **Tresquare technologies**.*

This minimally invasive strategy conceptually offers an alternative to surgical valve explantation, with the potential to improve device expansion, reduce transvalvular gradients, and mitigate the risk of coronary obstruction in redo-TAVI procedures, all while avoiding the morbidity associated with open-heart surgery.

9.2 Computational framework for evaluating leaflet resection

To investigate the biomechanical and hemodynamic benefits of leaflet resection, a patient-specific computational modeling pipeline was established. The TAVI FEA simulation was performed according to paragraphs 6.3.1.

To simulate the redo-TAVI procedure, an additional computational simulation was

performed. Prior to the deployment of the second S3 valve, a calcification pattern was reconstructed on the leaflets of the first implanted S3, using a mid-range distribution of calcification to replicate S3 structural degeneration (Figure 9.2) [96].

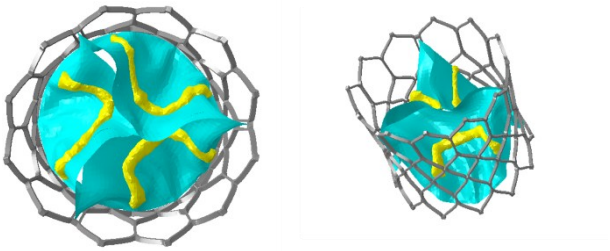

***Figure 9.2**: Pattern of calcification virtually generated on S3 device.*

The second S3 was positioned at the outflow of the initial implant, and all procedural steps from the first TAVI simulation were replicated to implant the new device above the pre-existing one.

The redo-TAVI procedure was simulated under two conditions: first, with the calcified S3 leaflets, and second, following a virtual resection process. The resection aimed to remove calcified tissue while preserving the commissures and the leaflet regions attached to the skirt. This process was implemented in Rhinoceros by generating a cylindrical geometry centered on the leaflets and applying a Boolean splitting operation between the cylinder and the leaflets. The resected leaflets were then meshed and reintroduced into the computational model for the redo-TAVI simulation. Contact interactions were defined between the stent frame of the second S3 and all components of the THV to accurately simulate anchoring mechanics (Figure 9.3 A – B).

The workflow was then extended to explore redo-TAVI scenarios involving the Evolut PRO valve, following the methodology outlined in paragraph 8.2.2 (Figure 9.3 C – D).

The complete set of simulated scenarios included:

- 23 mm S3 implanted in 23 mm S3 (Figure 9.4 – 1)
- 23 mm S3 implanted in 26 mm S3 (Figure 9.4 – 2)
- 26 mm S3 implanted in 26 mm S3 (Figure 9.4 – 3)
- 26 mm Evolut PRO implanted in 26 mm S3 (Figure 9.5 – 1)
- 29 mm Evolut PRO implanted in 26 mm S3 (Figure 9.5 – 2).

Each simulation was performed in two different conditions (without leaflet resection and with leaflet resection).

Eccentricity and expansion indices were derived from the simulation results and explore the

benefits of resection procedure. The eccentricity index was computed as follows: [1 − (minimum external TAV diameter/maximum external TAV diameter)] × 100 while the expansion index was expressed in relation to nominal prosthesis size as follows: (observed TAV external area/ device area nominal size) × 100. Both indices were measured at three distinct heights along the valve structure: inflow, mid, and outflow levels.

For each structural simulation, a corresponding SPH analysis was performed following the procedure described in paragraphs 6.3.2. These hemodynamic simulations used the post-deployment geometry extracted from the finite element analysis and incorporated patient-specific cuff pressures to ensure physiologically meaningful inflow conditions (Figure 9.6). Key outcome measures, EOA (calculated with the Gorlin equation) and TPG were computed according to ISO 5840-1 guidelines.

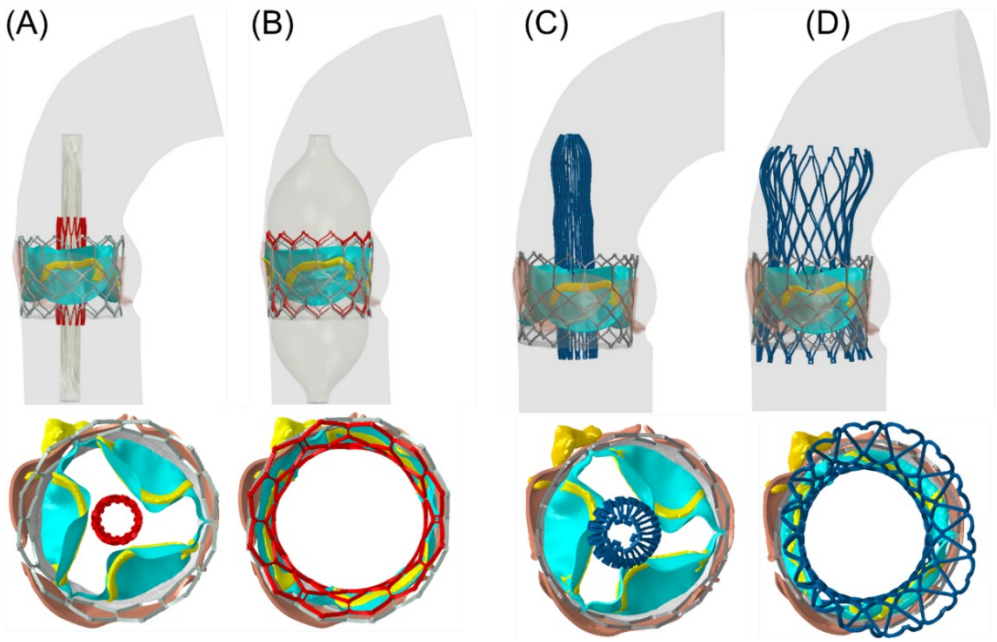

***Figure 9.3**: Different steps of redo-TAVI with S3 – in – S3 scenario (A – B); Evolut – in – S3 scenario (C – D).*

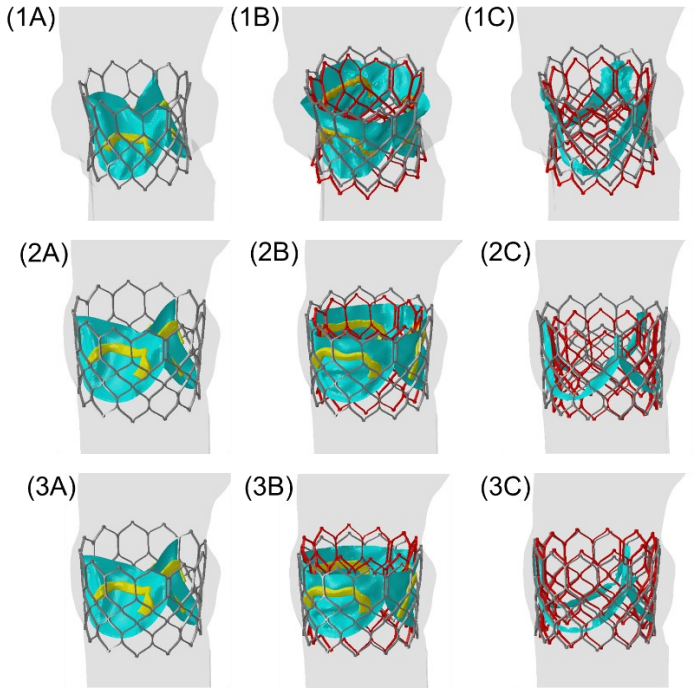

***Figure 9.4**: All S3-in-S3 scenarios explored; (1A) First TAVI with S3 of 23 mm, (1B) 23-in-23 redo-TAVI, (1C) 23-in-23 redo-TAVI after resection of first THV; (2A) First TAVI with S3 of 26 mm, (2B) 23-in-26 redo-TAVI, (2C) 23-in-26 redo-TAVI after resection of first THV; (3A) First TAVI with S3 of 26 mm, (3B) 26-in-26 redo-TAVI, (3C) 26-in-26 redo-TAVI after resection of first THV.*

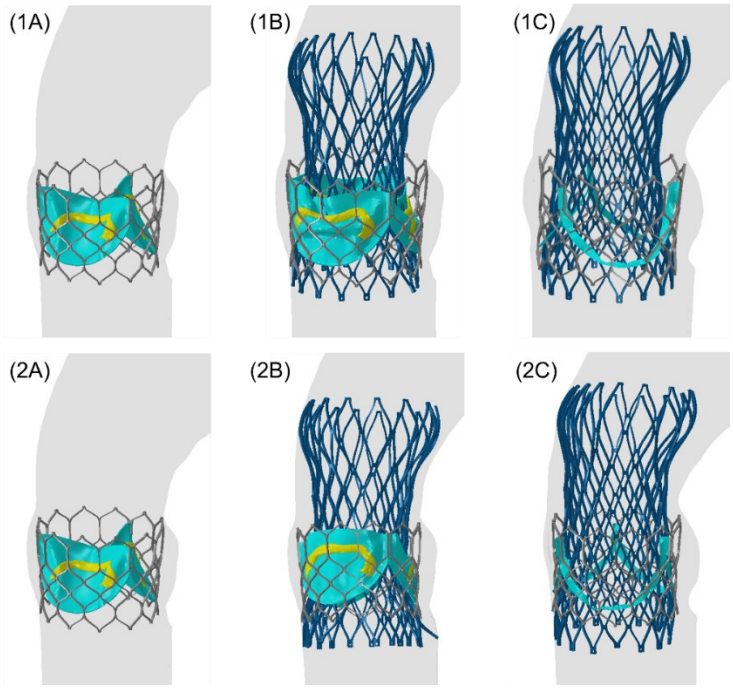

***Figure 9.5**: All Evolut-in-S3 scenarios explored; (1A) First TAVI with S3 of 26 mm, (1B) 26 Evolut-in-26 redo-TAVI, (1C) 26 Evolut-in-26 redo-TAVI after resection of first THV; (2A) First TAVI with S3 of 26 mm, (2B) 29 Evolut-in-26 redo-TAVI, (2C) 29 Evolut-in-26 redo-TAVI after resection of first THV.*

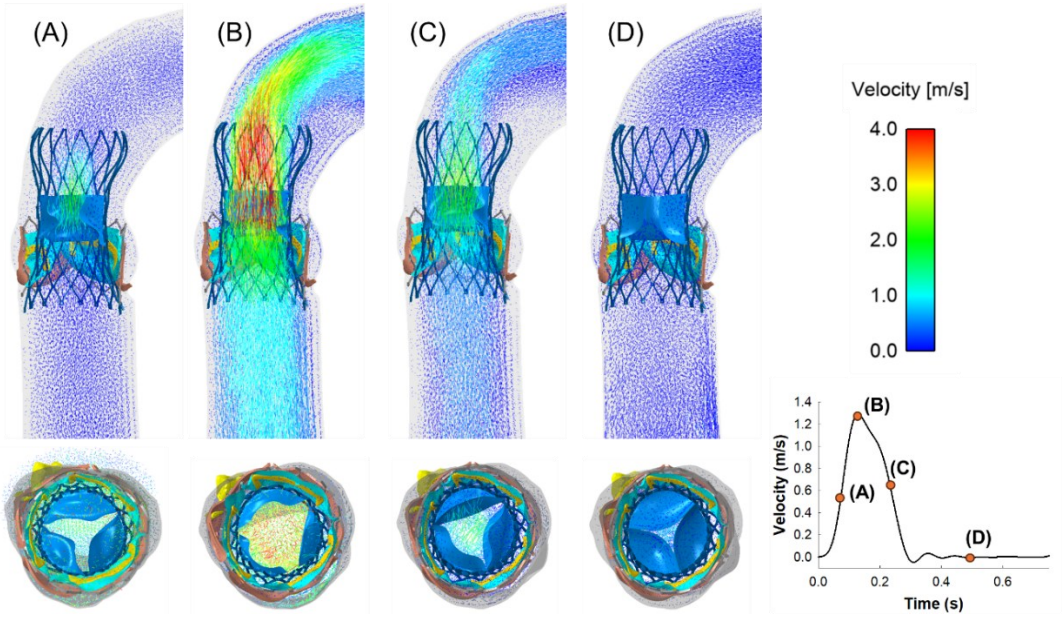

***Figure 9.6**: Different steps of SPH simulation across one cardiac cycle; from (A) at the beginning of systole, (B) peak systole, (C) diastole and (D) late diastole.*

9.3 Results

A direct one-to-one comparison between each redo-TAVI configuration with and without leaflet resection revealed a consistent and measurable improvement across all investigated performance metrics. In every scenario, the presence of calcified leaflets inside the first implanted valve acted as a mechanical constraint, limiting the ability of the second prosthesis to expand symmetrically. When the calcified cusps were removed, the geometric and hemodynamic conditions improved systematically.

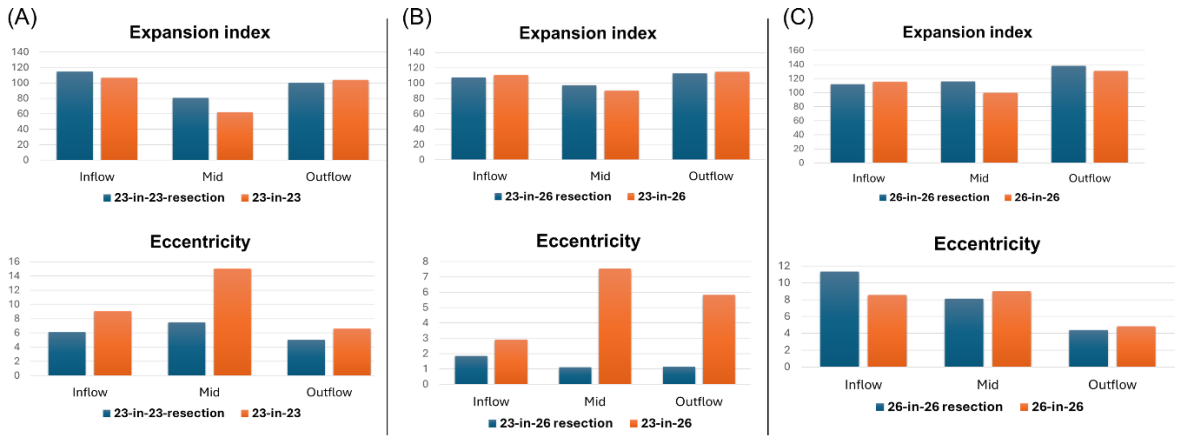

***Figure 9.10**: Results in terms of Expansion index and Eccentricity for S3-in-S3 scenarios; specifically (A) 23-in-23, (B) 23-in-26, (C) 26-in-26.*

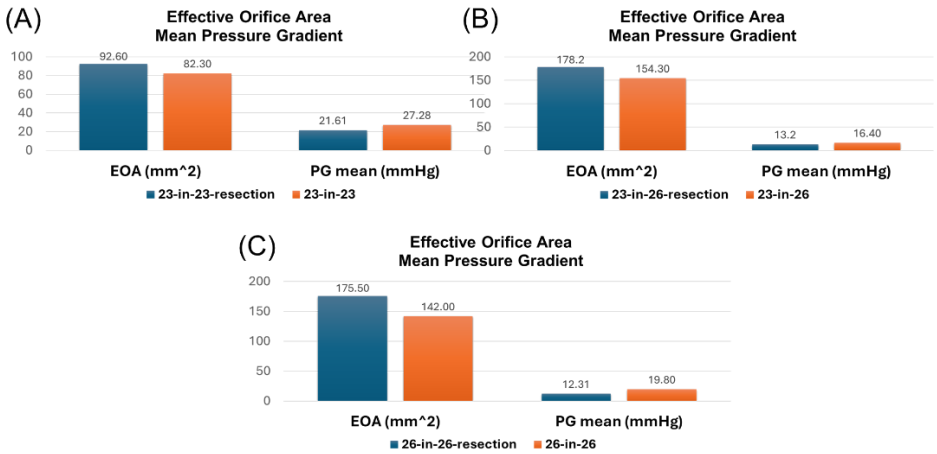

***Figure 9.11**: Results in terms of EOA and TPG for S3-in-S3 scenarios; specifically (A) 23-in-23, (B) 23-in-26, (C) 26-in-26.*

From a structural perspective, leaflet resection produced a notable reduction in stent eccentricity, reflecting a more uniform expansion of the second device and a closer interaction with the surrounding frame. This improvement was closely associated with a higher overall expansion of the implanted valve, particularly in configurations where the initial prosthesis imposed significant geometric restriction. The reduction of asymmetric loads and localized resistance allowed the second THV to achieve a deployment profile closer to its intended circular design.

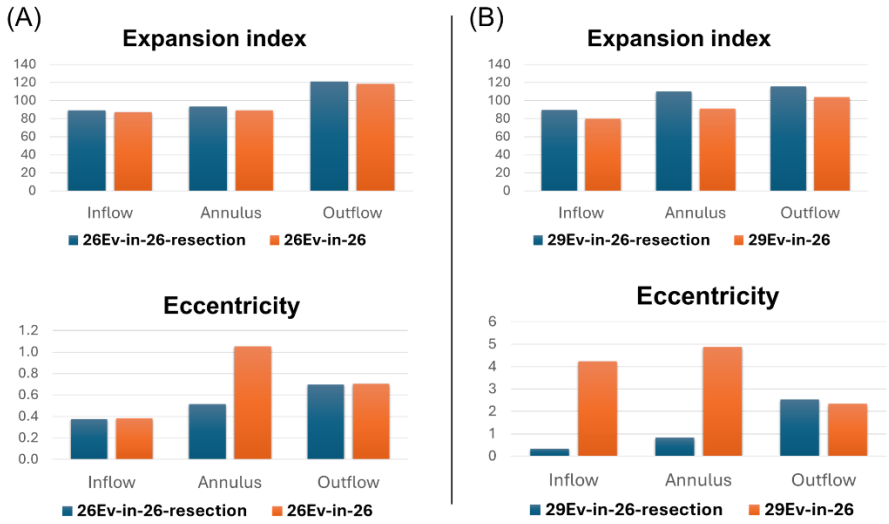

***Figure 9.12**: Results in terms of Expansion index and Eccentricity for Evolut-in-S3 scenarios; specifically (A) 26Evolut-in-23, (B) 29Evolut-in-26.*

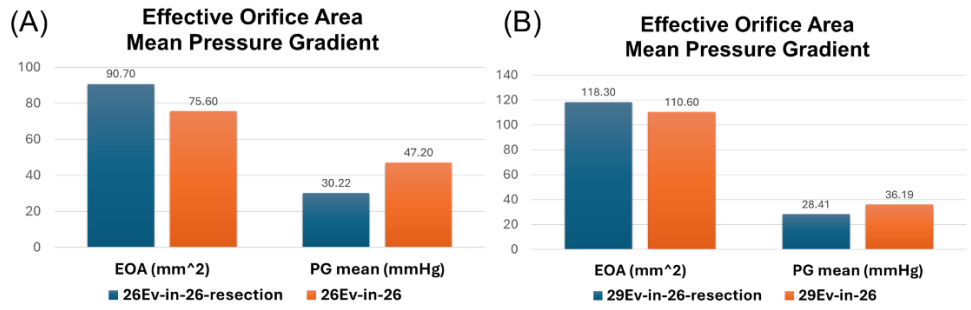

***Figure 9.13**: Results in terms of EOA and TPG for Evolut-in-S3 scenarios; specifically (A) 26Evolut-in-23, (B) 29Evolut-in-26.*

These mechanical improvements translated directly into enhanced hemodynamic performance. In all corresponding pairs of simulations, leaflet resection led to an increase in EOA, indicating a larger functional opening for blood flow. This improvement was most pronounced in small-frame redo procedures, where residual leaflet tissue would otherwise occupy a substantial portion of the flow channel. Consistently, the TPG decreased across all resected configurations, demonstrating a reduction in flow resistance and a restoration of more physiological pressure recovery.

9.4 Discussion and conclusion

This study explores the feasibility and potential benefits of transcatheter leaflet resection before redo-TAVI procedures. Current redo-TAVI techniques face limitations due to the presence of calcified leaflets, which can impede optimal valve expansion and contribute to PPM and coronary obstruction [97]. To address these challenges, a novel catheter-based cutter was developed to remove the leaflets of the previously implanted transcatheter valve before the second valve implantation. FEA and SPH simulations were employed to evaluate the mechanical and hemodynamic performance of this approach. The results demonstrated improved valve expansion, reduced eccentricity, and enhanced hemodynamic function compared to conventional redo-TAVI procedures. This innovation has the potential to significantly improve redo-TAVI outcomes by ensuring a more symmetrical expansion and minimizing complications.

Different scenarios were explored to cover a broad spectrum of redo-TAVI conditions encountered in clinical practice. The S3-in-S3 configurations reproduce typical redo procedures, where a device of equal or slightly larger size is used to manage structural

degeneration of the first prosthesis. The Evolut-in-S3 scenarios reflect a strategy commonly adopted when improved hemodynamic performance is desired: the supra-annular design of the Evolut PRO valve and its ability to expand within larger internal diameters can enhance flow capacity, which is particularly beneficial in smaller or underexpanded first implants.

From a biomechanical standpoint, a larger internal diameter provides increased leaflet opening area, which generally leads to a higher EOA and lower TPG. This relationship is well established clinically and represents a key motivation for selecting larger valves in redo-TAVI, especially in patients with elevated gradients or PPM. The possibility of increasing the valve expansion during redo-TAVI after the resection of the first implanted THV represents a gold option to solve this limitation.

The BASILICA technique is currently one of the most used approaches to mitigate coronary obstruction in redo-TAVI procedures [98, 99]. While BASILICA effectively splits the leaflets, it does not remove them entirely, leaving residual tissue that can contribute to PPM and suboptimal valve expansion. The presence of residual leaflet material may also interfere with optimal hemodynamic function and long-term durability of the implanted valve.

Navarra et al. [100] presents a novel approach to native aortic valve resection using a circular blade-based device. This study, conducted on surgical aortic valve replacement candidates, evaluated the feasibility and efficacy of a resection tool equipped with a foldable blade designed to efficiently remove the native aortic valve while preventing debris embolization. The device effectively captured and removed the leaflets without significant complications, making it a promising advancement in valve resection for surgical applications. However, this approach remains surgical rather than transcatheter, limiting its use in minimally invasive procedures. The present study introduces a new concept: a fully transcatheter device designed to remove the leaflets of the previously implanted TAVI prosthesis before redo-TAVI. Unlike traditional surgical leaflet resection methods, this innovative approach employs a catheter-based cutter for resection of degenerated leaflets prior to the implantation of a second TAV. This advancement seeks to address key issues associated with TAV-in-TAV procedures, including restricted expansion due to calcified leaflets and potential coronary obstruction. By removing the existing leaflets, the new valve can expand more symmetrically, reducing eccentricity and optimizing hemodynamic performance.

10. Conclusions

This thesis presented an integrated and comprehensive framework for patient-specific computational modeling of TAVI, addressing multiple levels of complexity—from anatomical reconstruction and device deployment mechanics to hemodynamics, virtual population analysis, and model credibility assessment. As TAVI continues to expand toward younger and more heterogeneous patient populations, the ability to generate accurate, validated, and reproducible computational predictions becomes increasingly important for supporting device innovation, pre-procedural decision-making, and regulatory acceptance.

The contributions of this thesis span four major domains: patient-specific anatomical modeling and segmentation accuracy, SSM and virtual cohort generation, high-fidelity structural and hemodynamic simulation of TAVI, and UQ and advanced applications including redo-TAVI and leaflet resection. Together, these developments form a robust computational ecosystem for the study and prediction of TAVI outcomes.

First, the thesis established a rigorous evaluation of segmentation accuracy, demonstrating that voxelization introduces only marginal geometric deviations, while segmentation methodology constitutes the major source of geometric uncertainty. These findings underscore the need for standardized segmentation protocols to ensure reproducibility of patient-specific models, a key prerequisite for the deployment of in silico tools in clinical and regulatory environments.

Second, a SSM of the calcified aortic root was created to quantify morphological variability and to generate a virtual cohort of anatomies representative of a real TAVI population. By integrating principal component analysis with machine learning methods, the study demonstrated that shape-derived features can reliably predict clinical parameters such as transvalvular pressure gradient and optimal prosthesis sizing. This research highlights the feasibility and value of in-silico trials, where synthetic populations can augment clinical datasets, explore rare anatomies, and support device evaluation across wide morphological scenarios.

Third, the thesis developed an advanced patient-specific FEA and SPH platform capable of simulating the complete TAVI procedure, including crimping, deployment, device - tissue interaction, and post-deployment blood flow. The framework integrates detailed device modeling, automated positioning algorithms, inverse-calibrated material properties, and physiological boundary conditions, offering a high-fidelity tool for investigating both

mechanical and hemodynamic responses. This modeling environment was validated against clinical data, demonstrating strong predictive capabilities for structural outcomes and identifying limitations in hemodynamic prediction accuracy.

Fourth, the work incorporated a complete VVUQ analysis following the ASME V&V40 standard. Sensitivity analyses revealed that device material properties and balloon expansion volume dominate the mechanical response, while hemodynamic outcomes are driven primarily by physiological parameters such as heart rate, pressure waveforms, and flow velocity. The risk-informed validation approach confirmed strong agreement between simulated and clinical device expansion, while highlighting remaining challenges in the accurate prediction of EOA and TPG. These findings represent an important contribution to establishing regulatory-grade computational models for TAVI.

Finally, two advanced applications were investigated: a parametric study of redo-TAVI, quantifying how implantation depth, device size, and interactions between multiple THV frames affect coronary flow and VTC distance; a novel transcatheter leaflet resection strategy designed to improve redo-TAVI outcomes. Computational results demonstrated that resection of degenerated leaflets promotes more symmetric expansion, reduces eccentricity, and improves hemodynamic performance, suggesting a promising minimally invasive alternative to mitigate PPM and coronary obstruction.

The proposed computational framework is designed as a decision-support tool that complements clinical judgment. Its main clinical application concerns complex and borderline cases and redo-TAVI procedures, where valve-in-valve interaction may affect device expansion or compromise coronary access. In these situations, patient-specific simulations can provide additional insight that cannot be fully obtained through conventional imaging alone. To support this intended use, a high level of rigor was adopted during the credibility assessment. In accordance with the ASME V&V40 standard, the model was validated against clinical data with a target difference between predicted and measured quantities below 5%.

Overall, this thesis demonstrates that computational modeling can serve as a credible, efficient, and clinically relevant complement to traditional TAVI evaluation methods, supporting both device development and personalized treatment planning.

11. Appendix

Appendix I

Pareto plot showing sensitivity of model inputs on the output device diameter for the 23 mm S3 device (Case #2) and 26 mm S3 device (Case #4) at different cross-sections (A-F); Note: Ball_Exp = balloon expansion; C1_Calc = Neo-Hookean material parameter of calcification; C1_Aorta = Neo-Hookean material parameter of aortic wall; Depth = implantation depth; S3_E = Young's modulus of S3 device; Thk = aortic wall thickness.

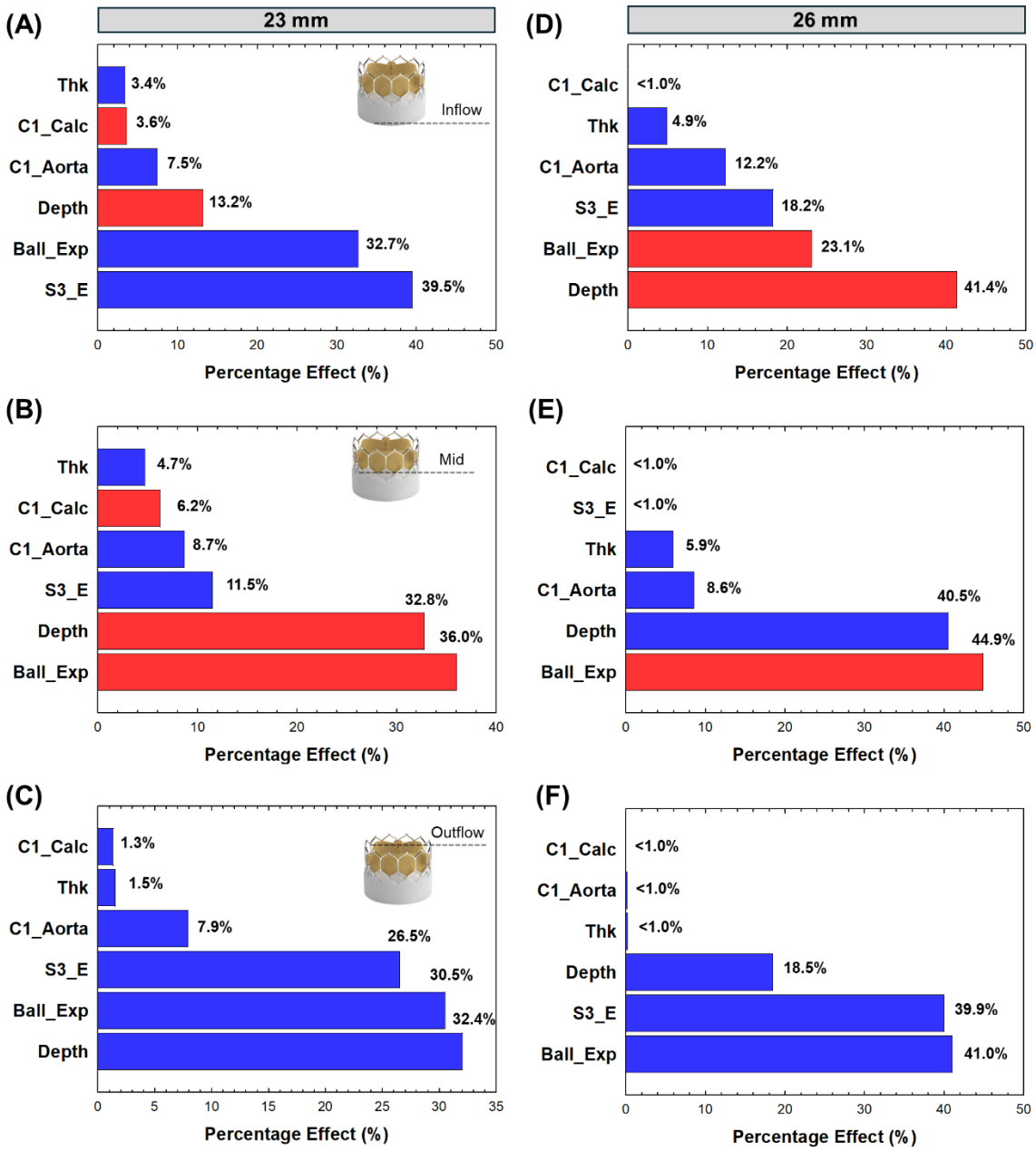

Pareto plot showing sensitivity of model inputs on both EOA and TPG device (A-D) diameter for the 23 mm S3 device (Case #2) and 26 mm S3 device (Case #4); Note: Ball_Exp = balloon expansion; C1_Calc = Neo-Hookean material parameter of calcification; C1_Aorta = Neo-Hookean material parameter of aortic wall; Depth = implantation depth; HR = heart rate; Pdias = diastolic pressure; Psys = systolic pressure; S3_E = Young's modulus of S3 device; S3_Flow = S3 flow velocity; Thk = aortic wall thickness.

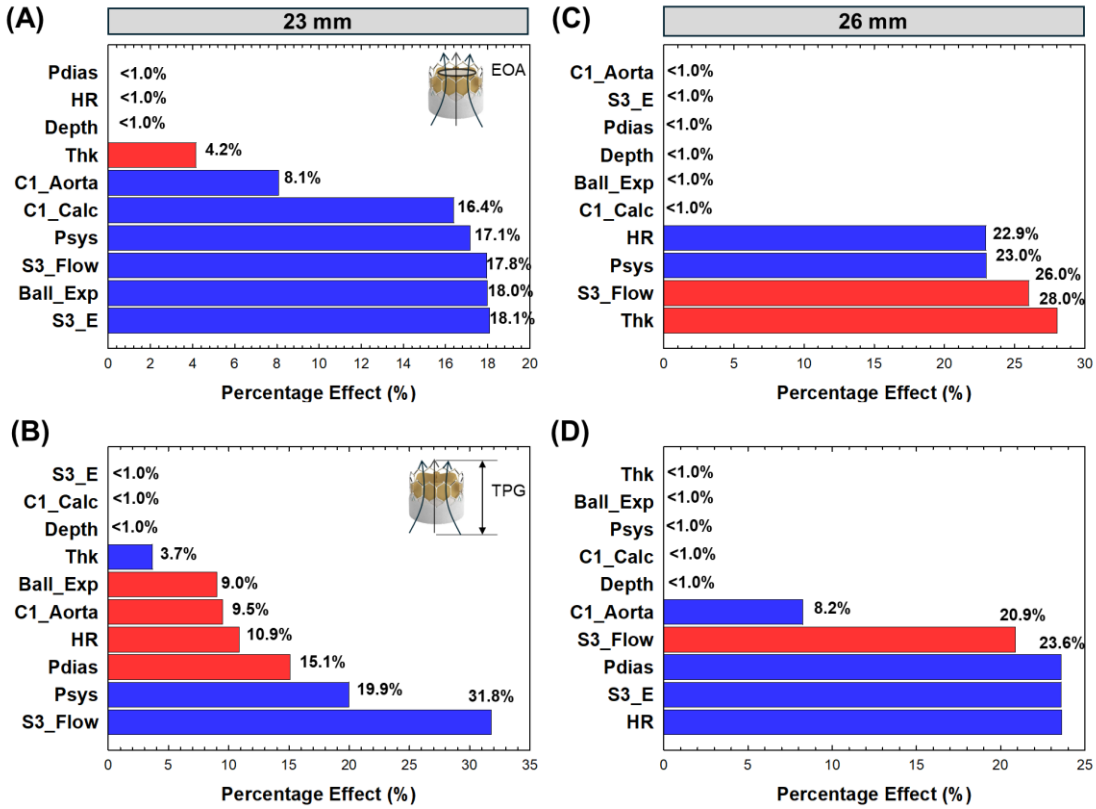

Appendix II

CDF curves for both clinical and in-silico data of the device diameter showing the area metric and its value confined by the two CDF curves (grey area) computed for both 23 and 26 mm S3 devices of Case #2 and Case #4 models (A-F).

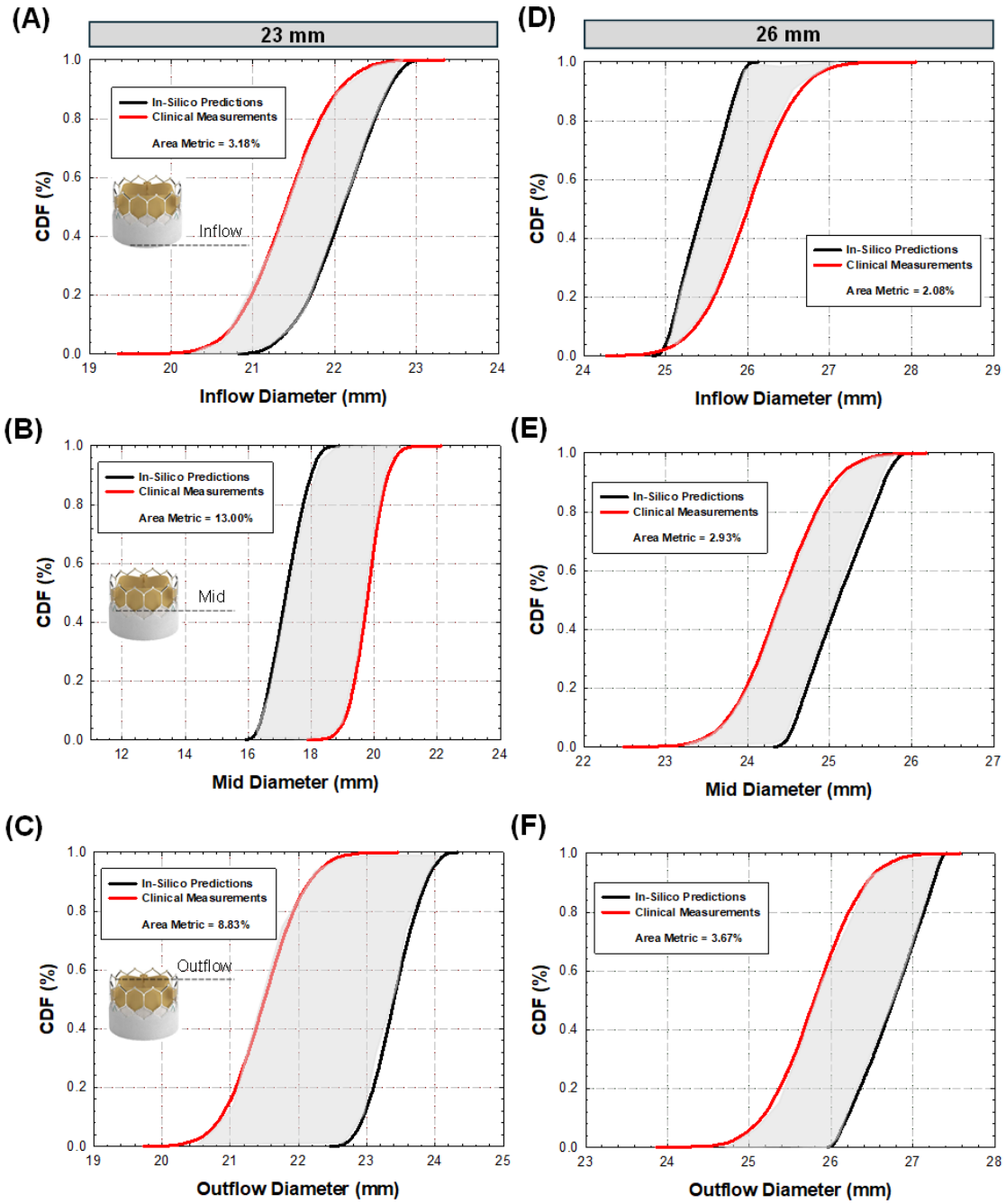

CDF curves for both clinical and in-silico data of both EOA and TPG showing the area metric and its value confined by the two CDF curves (grey area) computed for both 23 and 26 mm S3 devices of Case #2 and Case #4 models (A-D).

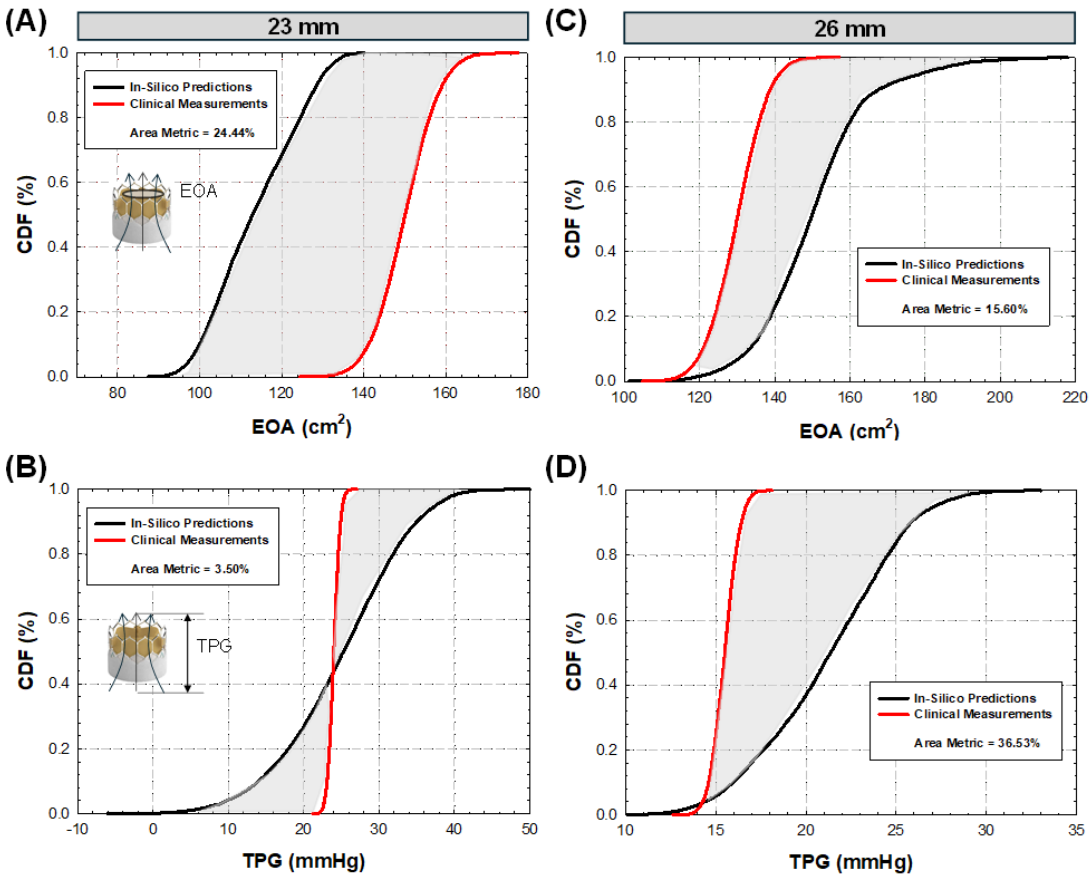

12. List of publications

Journal articles

1. Pasta Salvatore; Catalano Chiara; Crascì Fabrizio; **Scuoppo Roberta**; A custom-built planar biaxial system for soft tissue material testing. HardwareX, 16 (2023).

2. Catalano Chiara; Crascì Fabrizio; Puleo Silvia; **Scuoppo Roberta**; Pasta Salvatore; Raffa Giuseppe M; Computational fluid dynamics in cardiac surgery and perfusion: A review. Perfusion, 40, 2, 362-370 (2025).

3. **Scuoppo Roberta**; Castelbuono Salvatore; Cannata Stefano; Gentile Giovanni; Agnese Valentina; Bellavia Diego; Gandolfo Caterina; Pasta Salvatore; Generation of a virtual cohort of TAVI patients for in silico trials: a statistical shape and machine learning analysis. Medical & Biological Engineering & Computing, 63, 2, 467-482, (2025).

4. **Scuoppo Roberta**; Cannata Stefano; Gentile Giovanni; Gandolfo Caterina; Pasta Salvatore; Parametric analysis of transcatheter aortic valve replacement in transcatheter aortic valve replacement: evaluation of coronary flow obstruction. Frontiers in Bioengineering and Biotechnology, 11, 1267986, (2023).

5. **Scuoppo Roberta**; Catalano Chiara; Costagliola Eleonora; Cannata Stefano; Pasta Salvatore; Gandolfo Caterina; Augmented Reality and Computational Simulations for the Preprocedural Planning of Transcatheter Aortic Valve Replacement After Previous Transcatheter Mitral Valve Replacement. Biomechanics, 4, 4, 730-737 (2024).

6. **Scuoppo Roberta**; Cannata Stefano; Gandolfo Caterina; Bellavia Diego; Pasta Salvatore; On the accuracy of the segmentation process and transcatheter heart valve dimensions in TAVI patients. Journal of Biomechanics, 176, 112357 (2024).

7. **Scuoppo Roberta**; Puleo Silvia; Sausa Giuseppe; Cannata Stefano; Gentile Giovanni; Guccione Julius M; Kassab Ghassan S; Gandolfo Caterina; Pasta Salvatore; Simulations of left atrial appendage inversion procedure: Patient-specific models with different appendage geometries. Computers in Biology and Medicine, 188, 109875 (2025).

8. **Scuoppo Roberta**; Catalano Chiara; Crascì Fabrizio; Pasta Salvatore; Credibility Assessment of the Patient-Specific Modeling of the Aneurysmal Ascending Thoracic Aorta: Verification, Validation and Uncertainty Quantification. Cardiovascular Engineering and Technology, 1-15 (2025).

9. **Scuoppo Roberta**; Catalano Chiara; Turgut Tahir; Götzen Nils; Cannata Stefano; Gentile Giovanni; Gandolfo Caterina; Pasta Salvatore; Credibility assessment of patient-specific modeling in transcatheter aortic valve implantation - Part 2: Uncertainty quantification and sensitivity analysis. APL bioengineering, 9, 4 (2025).

10. Catalano Chiara; **Scuoppo Roberta**; Turgut Tahir; Bouwman Vincent; Götzen Nils; Cannata Stefano; Gentile Giovanni; Gandolfo Caterina; Pasta Salvatore; Credibility assessment of patient-specific modeling in transcatheter aortic valve implantation. A population-based validation of patient-specific modeling, APL bioengineering, 9, 4 (2025).

Conference papers

1. **Scuoppo Roberta**; Cannata Stefano; Gandolfo Caterina; Pasta Salvatore. Structural Simulation of Transcatheter Heart Valve in Transcatheter Heart Valve. GNB2023, June 21st-23rd 2023, Padova, Italy.

2. **Scuoppo Roberta**; Cannata Stefano; Gandolfo Caterina; Pasta Salvatore. TRANSCATHETER HEART VALVE IN TRANSCATHETER HEART VALVE: A COMPUTATIONAL STUDY. XII Annual Meeting of the Italian Chapter of the European Society of Biomechanics, September 18-19, 2023, Turin, Italy.

3. **Scuoppo Roberta**; Pasta Salvatore, ON THE MODELING OF LEFT ATRIAL APPENDAGE INVERSION: A REVERSE GROWTH ANALYSIS, ECCOMAS Congress 2024, 3 - 7 June 2024, Lisbon, Portugal.

4. **Scuoppo Roberta**; Cannata Stefano; Gandolfo Caterina; Pasquino Stefano; Pasta Salvatore; Ferraro Mauro. Patient-specific computational analysis of TAVI-in-TAVI: assessing the impact of calcified leaflets resection. GNB2025, June 16th-18th 2025, Palermo, Italy.

5. **Scuoppo Roberta**; Cannata Stefano; Gandolfo Caterina; Pasta Salvatore. VERIFICATION, VALIDATION AND UNCERTAINTY QUANTIFICATION IN PATIENT-SPECIFIC TAVR MODELS. XIX Annual Meeting of the Italian Chapter of the European Society of Biomechanics June 18-19, 2025, Palermo, Italy.

6. **Scuoppo Roberta**; Gandolfo Caterina; Pasta Salvatore, Ferraro Mauro. PATIENT-SPECIFIC COMPUTATIONAL MODELING OF REDO-TAVI: EVALUATING THE ROLE OF CALCIFIED LEAFLET RESECTION. CMBBE, 2025, Barcelona.

13. References

1. Osnabrugge, R.L., et al., *Aortic stenosis in the elderly: disease prevalence and number of candidates for transcatheter aortic valve replacement: a meta-analysis and modeling study.* J Am Coll Cardiol, 2013. **62**(11): p. 1002-12.
2. Baillargeon, B., et al., *The Living Heart Project: A robust and integrative simulator for human heart function.* Eur J Mech A Solids, 2014. **48**: p. 38-47.
3. Aggarwal, A., et al., *Patient-Specific Modeling of Heart Valves: From Image to Simulation.* Funct Imaging Model Heart, 2013. **7945**: p. 141-149.
4. Anam, S.B., et al., *Assessment of Paravalvular Leak Severity and Thrombogenic Potential in Transcatheter Bicuspid Aortic Valve Replacements Using Patient-Specific Computational Modeling.* J Cardiovasc Transl Res, 2022. **15**(4): p. 834-844.
5. Hintermuller, C., et al., *A model based approach for multi-lead ECG array layout selection.* Med Image Comput Comput Assist Interv, 2006. **9**(Pt 1): p. 264-71.
6. Circhetta, S., et al., *Designing the Optimal Procedure: Role of CT Scan in the Planning of Transcatheter Structural Heart Interventions.* Applied Sciences-Basel, 2023. **13**(3).
7. Zhong, A. and C.A. Simmons, *Heart Valve Mechanobiology in Development and Disease.* Molecular and Cellular Mechanobiology, 2016: p. 255-276.
8. Freeman, R.V. and C.M. Otto, *Spectrum of calcific aortic valve disease: pathogenesis, disease progression, and treatment strategies.* Circulation, 2005. **111**(24): p. 3316-26.
9. Verheyen, N., et al., *Worsening Heart Failure After Transcatheter Aortic Valve Replacement: Unmasking the Left Ventricular Outflow Tract Obstruction.* JACC Cardiovasc Interv, 2021. **14**(18): p. e253-e255.
10. Maganti, K., et al., *Valvular heart disease: diagnosis and management.* Mayo Clin Proc, 2010. **85**(5): p. 483-500.
11. Onishi, T., et al., *The role of echocardiography in transcatheter aortic valve implantation.* Cardiovasc Diagn Ther, 2018. **8**(1): p. 3-17.
12. De Backer, O., et al., *Patient-Tailored Aortic Valve Replacement.* Front Cardiovasc Med, 2021. **8**: p. 658016.
13. Cribier, A., et al., *Percutaneous transcatheter implantation of an aortic valve prosthesis for calcific aortic stenosis: first human case description.* Circulation, 2002. **106**(24): p. 3006-3008.
14. Mack, M.J., et al., *Transcatheter aortic-valve replacement with a balloon-expandable valve in low-risk patients.* New England Journal of Medicine, 2019. **380**(18): p. 1695-1705.
15. Vinayak, M., et al., *Transcatheter Aortic Valve Replacement: Current Status and Future Indications.* J Clin Med, 2024. **13**(2).

16. Binder, R.K., et al., *Transcatheter aortic valve replacement with the SAPIEN 3: a new balloon-expandable transcatheter heart valve.* JACC Cardiovasc Interv, 2013. **6**(3): p. 293-300.

17. Mack, M.J., et al., *Transcatheter Aortic-Valve Replacement with a Balloon-Expandable Valve in Low-Risk Patients.* N Engl J Med, 2019. **380**(18): p. 1695-1705.

18. Claessen, B.E., et al., *Considerations for Optimal Device Selection in Transcatheter Aortic Valve Replacement: A Review.* JAMA Cardiol, 2021. **6**(1): p. 102-112.

19. Morganti, S., et al., *Simulation of transcatheter aortic valve implantation through patient-specific finite element analysis: Two clinical cases.* Journal of Biomechanics, 2014. **47**(11): p. 2547-2555.

20. Pasta, S., et al., *Simulation study of transcatheter heart valve implantation in patients with stenotic bicuspid aortic valve.* Med Biol Eng Comput, 2020.

21. Bianchi, M., et al., *Patient-specific simulation of transcatheter aortic valve replacement: impact of deployment options on paravalvular leakage.* Biomech Model Mechanobiol, 2019. **18**(2): p. 435-451.

22. Ghosh, R.P., et al., *Numerical evaluation of transcatheter aortic valve performance during heart beating and its post-deployment fluid–structure interaction analysis.* Biomechanics and modeling in mechanobiology, 2020. **19**(5): p. 1725-1740.

23. Pasta, S., et al., *Transcatheter Heart Valve Implantation in Bicuspid Patients with Self-Expanding Device.* Bioengineering, 2021. **8**(7): p. 91.

24. Bosi, G.M., et al., *Patient-specific finite element models to support clinical decisions: A lesson learnt from a case study of percutaneous pulmonary valve implantation.* Catheter Cardiovasc Interv, 2015. **86**(6): p. 1120-30.

25. Finotello, A., S. Morganti, and F. Auricchio, *Finite element analysis of TAVI: Impact of native aortic root computational modeling strategies on simulation outcomes.* Medical Engineering & Physics, 2017. **47**: p. 2-12.

26. Bailey, J., N. Curzen, and N.W. Bressloff, *Assessing the impact of including leaflets in the simulation of TAVI deployment into a patient-specific aortic root.* Comput Methods Biomech Biomed Engin, 2016. **19**(7): p. 733-44.

27. Wang, Q., et al., *Simulations of transcatheter aortic valve implantation: implications for aortic root rupture.* Biomech Model Mechanobiol, 2015. **14**(1): p. 29-38.

28. Catalano, C., et al., *Computational fluid dynamics in cardiac surgery and perfusion: A review.* Perfusion, 2025. **40**(2): p. 362-370.

29. Zingaro, A., et al., *A comprehensive stroke risk assessment by combining atrial computational fluid dynamics simulations and functional patient data.* Scientific Reports, 2024. **14**(1).

30. Basri, A.A., et al., *Fluid Structure Interaction on Paravalvular Leakage of Transcatheter Aortic Valve Implantation Related to Aortic Stenosis: A Patient-Specific Case.* Comput Math Methods Med, 2020. **2020**: p. 9163085.

31. Chandran, K.B. and S.C. Vigmostad, *Patient-specific bicuspid valve dynamics: overview of methods and challenges.* J Biomech, 2013. **46**(2): p. 208-16.

32. Biffi, B., et al., *A workflow for patient-specific fluid-structure interaction analysis of the mitral valve: A proof of concept on a mitral regurgitation case.* Med Eng Phys, 2019. **74**: p. 153-161.

33. Luraghi, G., F. Migliavacca, and J.F.R. Matas, *Study on the accuracy of structural and FSI heart valves simulations.* Cardiovascular engineering and technology, 2018. **9**(4): p. 723-738.

34. Luraghi, G., et al., *On the Modeling of Patient-Specific Transcatheter Aortic Valve Replacement: A Fluid-Structure Interaction Approach.* Cardiovasc Eng Technol, 2019. **10**(3): p. 437-455.

35. Mao, W., K. Li, and W. Sun, *Fluid-Structure Interaction Study of Transcatheter Aortic Valve Dynamics Using Smoothed Particle Hydrodynamics.* Cardiovasc Eng Technol, 2016. **7**(4): p. 374-388.

36. Kemp, I., et al., *Experimental validation of the fluid-structure interaction simulation of a bioprosthetic aortic heart valve.* Australas Phys Eng Sci Med, 2013. **36**(3): p. 363-73.

37. Hsu, M.C., et al., *Dynamic and fluid-structure interaction simulations of bioprosthetic heart valves using parametric design with T-splines and Fung-type material models.* Computational Mechanics, 2015. **55**(6): p. 1211-1225.

38. Wald, S., A. Liberzon, and I. Avrahami, *A numerical study of the hemodynamic effect of the aortic valve on coronary flow.* Biomechanics and Modeling in Mechanobiology, 2018. **17**(2): p. 319-338.

39. Catalano, C., et al., *Credibility assessment of patient-specific modeling in transcatheter aortic valve implantation. I. A population-based validation of patient-specific modeling.* APL Bioeng, 2025. **9**(4): p. 046101.

40. Verstraeten, S., et al., *Generation of synthetic aortic valve stenosis geometries for in silico trials.* Int J Numer Method Biomed Eng, 2024. **40**(1): p. e3778.

41. Catalano, C., et al. *Verification and validation of transcatheter heart valve implantation in a virtual human cohort*. in *18th International Symposium on Computer Methods in Biomechanics and Biomedical Engineering*. 2023. Paris (FR).

42. Viceconti, M., et al., *In silico trials: Verification, validation and uncertainty quantification of predictive models used in the regulatory evaluation of biomedical products.* Methods, 2021. **185**: p. 120-127.

43. Scuoppo, R., et al., *Credibility assessment of patient-specific modeling in transcatheter aortic valve implantation-Part 2: Uncertainty quantification and sensitivity analysis.* APL Bioeng, 2025. **9**(4): p. 046102.

44. (ASME), T.A.S.o.M.E., *Assessing Credibility of Computational Modeling Through Verification and Validation: Application to Medical Devices, ASME V&V 40-2018,*. 2018.

45. (ASME), T.A.S.o.M.E., *Standard for Verification and Validation in Computational Solid Mechanics, ASME V&V 10-2019*. 2019.

46. Scardulla, F., et al., *Shear stress alterations in the celiac trunk of patients with a continuous-flow left ventricular assist device as shown by in-silico and in-vitro flow analyses.* J Heart Lung Transplant, 2017. **36**(8): p. 906-913.

47. Catalano, C., et al., *On the Material Constitutive Behavior of the Aortic Root in Patients with Transcatheter Aortic Valve Implantation.* Cardiovasc Eng Technol, 2024. **15**(1): p. 95-109.

48. Pasta, S., et al., *Three-dimensional parametric modeling of bicuspid aortopathy and comparison with computational flow predictions.* Artif Organs, 2017. **41**(9): p. E92-E102.

49. Catalano, C., et al., *Atlas-Based Evaluation of Hemodynamic in Ascending Thoracic Aortic Aneurysms.* Applied Sciences-Basel, 2022. **12**(1).

50. Scuoppo, R., et al., *On the accuracy of the segmentation process and transcatheter heart valve dimensions in TAVI patients.* Journal of Biomechanics, 2024. **176**.

51. Lo Giudice, A., et al., *One Step before 3D Printing-Evaluation of Imaging Software Accuracy for 3-Dimensional Analysis of the Mandible: A Comparative Study Using a Surface-to-Surface Matching Technique.* Materials, 2020. **13**(12).

52. Argüello, D., H.G.S. Acevedo, and O.A. González-Estrada, *Comparison of segmentation tools for structural analysis of bone tissues by finite elements.* 5th International Meeting for Researchers in Materials and Plasma Technology (5th Imrmpt), 2019. **1386**.

53. Szymor, P., M. Kozakiewicz, and R. Olszewski, *Accuracy of open-source software segmentation and paper-based printed three-dimensional models.* Journal of Cranio-Maxillofacial Surgery, 2016. **44**(2): p. 202-209.

54. Sankaran, S., et al., *Uncertainty quantification in coronary blood flow simulations: Impact of geometry, boundary conditions and blood viscosity.* Journal of Biomechanics, 2016. **49**(12): p. 2540-2547.

55. Eck, V.G., et al., *A guide to uncertainty quantification and sensitivity analysis for cardiovascular applications.* International Journal for Numerical Methods in Biomedical Engineering, 2016. **32**(8).

56. Bertolini, M., et al., *Evaluation of segmentation accuracy and its impact on patient-specific CFD analysis.* International Journal of Interactive Design and Manufacturing - Ijidem, 2022. **16**(2): p. 545-556.

57. Scuoppo, R., et al., *Generation of a virtual cohort of TAVI patients for in silico trials: a statistical shape and machine learning analysis.* Med Biol Eng Comput, 2025. **63**(2): p. 467-482.

58. Luraghi, G., J.F. Rodriguez Matas, and F. Migliavacca, *In silico approaches for transcatheter aortic valve replacement inspection.* Expert Review of Cardiovascular Therapy, 2021. **19**(1): p. 61-70.

59. Geronzi, L., et al., *Computer-aided shape features extraction and regression models for predicting the ascending aortic aneurysm growth rate.* Comput Biol Med, 2023. **162**: p. 107052.

60. Cosentino, F., et al., *Statistical Shape Analysis of Ascending Thoracic Aortic Aneurysm: Correlation between Shape and Biomechanical Descriptors.* J Pers Med, 2020. **10**(2).

61. Viceconti, M., et al., *Possible Contexts of Use for In Silico Trials Methodologies: A Consensus-Based Review.* IEEE J Biomed Health Inform, 2021. **25**(10): p. 3977-3982.

62. Scuoppo, R., et al., *Parametric analysis of transcatheter aortic valve replacement in transcatheter aortic valve replacement: evaluation of coronary flow obstruction.* Front Bioeng Biotechnol, 2023. **11**: p. 1267986.

63. Abbasi, M., et al., *High resolution three-dimensional strain mapping of bioprosthetic heart valves using digital image correlation.* J Biomech, 2018. **76**: p. 27-34.

64. Anam, S.B., et al., *Validating In Silico and In Vitro Patient-Specific Structural and Flow Models with Transcatheter Bicuspid Aortic Valve Replacement Procedure.* Cardiovasc Eng Technol, 2022. **13**(6): p. 840-856.

65. Sciortino, V., et al., *A Population-Based 3D Atlas of the Pathological Lumbar Spine Segment.* Bioengineering (Basel), 2022. **9**(8).

66. Bridio, S., et al., *Generation of a Virtual Cohort of Patients for in Silico Trials of Acute Ischemic Stroke Treatments.* Applied Sciences-Basel, 2023. **13**(18).

67. La Mattina, A.A., et al., *Statistical Properties of a Virtual Cohort for In Silico Trials Generated with a Statistical Anatomy Atlas.* Ann Biomed Eng, 2023. **51**(1): p. 117-124.

68. Philip, F., et al., *Aortic annulus and root characteristics in severe aortic stenosis due to bicuspid aortic valve and tricuspid aortic valves: implications for transcatheter aortic valve therapies.* Catheter Cardiovasc Interv, 2015. **86**(2): p. E88-98.

69. Yevtushenko, P., et al., *Modelling blood flow in patients with heart valve disease using deep learning: A computationally efficient method to expand diagnostic capabilities in clinical routine.* Front Cardiovasc Med, 2023. **10**: p. 1136935.

70. Bosi, G.M., et al., *Population-specific material properties of the implantation site for transcatheter aortic valve replacement finite element simulations.* Journal of biomechanics, 2018. **71**: p. 236-244.

71. Bosi, G.M., et al., *A validated computational framework to predict outcomes in TAVI.* Scientific reports, 2020. **10**(1): p. 1-11.

72. Kleinstreuer, C., et al., *Computational mechanics of Nitinol stent grafts.* J Biomech, 2008. **41**(11): p. 2370-8.

73. Pasta, S., et al., *Simulation of left ventricular outflow tract (LVOT) obstruction in transcatheter mitral valve-in-ring replacement.* Med Eng Phys, 2020. **82**: p. 40-48.

74. Plitman Mayo, R., et al., *Numerical models for assessing the risk of leaflet thrombosis post-transcatheter aortic valve-in-valve implantation.* R Soc Open Sci, 2020. **7**(12): p. 201838.

75. Pappalardo, F., et al., *Toward A Regulatory Pathway for the Use of in Silico Trials in the CE Marking of Medical Devices.* IEEE J Biomed Health Inform, 2022. **26**(11): p. 5282-5286.

76. Schruben, L.W., *Establishing the credibility of simulations.* Simulation, 1980. **34**(101-105).

77. Musuamba, F.T., et al., *Scientific and regulatory evaluation of mechanistic in silico drug and disease models in drug development: Building model credibility.* CPT Pharmacometrics Syst Pharmacol, 2021. **10**(8): p. 804-825.

78. Schwer, L.E., *An overview of the PTC 60/V&V 10: guide for verification and validation in computational solid mechanics.* Engineering with Computers, 2007. **23**(4): p. 245-252.

79. Hui, S., F. Mahmood, and R. Matyal, *Aortic Valve Area-Technical Communication: Continuity and Gorlin Equations Revisited.* J Cardiothorac Vasc Anesth, 2018. **32**(6): p. 2599-2606.

80. Velders, B.J.J., et al., *Measurement error in echocardiographic assessment of aortic stenosis: an epidemiological consideration of research methodology and clinical practice.* European Heart Journal, 2022. **43**: p. 2863-2863.

81. Ciurzynski, M., et al., *Accuracy of Doppler echocardiography in the hemodynamic assessment of pulmonary hypertension in patients with systemic sclerosis.* European Heart Journal, 2010. **31**: p. 869-870.

82. Sathananthan, J., et al., *Overexpansion of the SAPIEN 3 Transcatheter Heart Valve: An Ex Vivo Bench Study.* JACC Cardiovasc Interv, 2018. **11**(17): p. 1696-1705.

83. Finotello, A., et al., *Finite element analysis of transcatheter aortic valve implantation: Insights on the modelling of self-expandable devices.* Journal of the Mechanical Behavior of Biomedical Materials, 2021. **123**: p. 104772.

84. Calleja, A., et al., *Automated quantitative 3-dimensional modeling of the aortic valve and root by 3-dimensional transesophageal echocardiography in normals, aortic regurgitation, and aortic stenosis: comparison to computed tomography in normals and clinical implications.* Circ Cardiovasc Imaging, 2013. **6**(1): p. 99-108.

85. McElhinney, D.B., et al., *Transcatheter Tricuspid Valve-in-Valve Implantation for the Treatment of Dysfunctional Surgical Bioprosthetic Valves An International, Multicenter Registry Study.* Circulation, 2016. **133**(16): p. 1582-+.

86. Nai Fovino, L., et al., *Coronary Angiography After Transcatheter Aortic Valve Replacement (TAVR) to Evaluate the Risk of Coronary Access Impairment After TAVR-in-TAVR.* Journal of the American Heart Association, 2020. **9**(13).

87. Forrestal, B.J., et al., *Risk of Coronary Obstruction and Feasibility of Coronary Access After Repeat Transcatheter Aortic Valve Replacement With the Self-Expanding Evolut Valve: A Computed Tomography Simulation Study.* Circ Cardiovasc Interv, 2020. **13**(12): p. e009496.

88. Ribeiro, H.B., et al., *Incidence, predictors, and clinical outcomes of coronary obstruction following transcatheter aortic valve replacement for degenerative bioprosthetic surgical valves: insights from the VIVID registry.* Eur Heart J, 2018. **39**(8): p. 687-695.

89. Pasta, S., et al., *Numerical simulation of transcatheter mitral valve replacement: The dynamic implication of LVOT obstruction in the valve-in-ring case.* Journal of Biomechanics, 2022. **144**.

90. Khan, J.M., et al., *Anterior Leaflet Laceration to Prevent Ventricular Outflow Tract Obstruction During Transcatheter Mitral Valve Replacement.* J Am Coll Cardiol, 2019. **73**(20): p. 2521-2534.

91. Babaliaros, V.C., et al., *Intentional Percutaneous Laceration of the Anterior Mitral Leaflet to Prevent Outflow Obstruction During Transcatheter Mitral Valve Replacement: First-in-Human Experience.* JACC Cardiovasc Interv, 2017. **10**(8): p. 798-809.

92. Ghosh, R.P., et al., *Numerical evaluation of transcatheter aortic valve performance during heart beating and its post-deployment fluid-structure interaction analysis.* Biomech Model Mechanobiol, 2020. **19**(5): p. 1725-1740.

93. Brouwer, J., et al., *Insight on patient specific computer modeling of transcatheter aortic valve implantation in patients with bicuspid aortic valve disease.* Catheter Cardiovasc Interv, 2018.

94. Tarantini, G., et al., *Redo-Transcatheter Aortic Valve Implantation Using the SAPIEN 3/Ultra Transcatheter Heart Valves-Expert Consensus on Procedural Planning and Techniques.* Am J Cardiol, 2023. **192**: p. 228-244.

95. De Backer, O., et al., *Redo-TAVI with a balloon-expandable valve and the impact of index transcatheter aortic valve design.* EuroIntervention, 2023. **19**(9): p. 714-716.

96. Sturla, F., et al., *Impact of different aortic valve calcification patterns on the outcome of transcatheter aortic valve implantation: A finite element study.* J Biomech, 2016. **49**(12): p. 2520-30.

97. Fukui, M., et al., *Feasibility of Redo-Transcatheter Aortic Valve Replacement in Sapien Valves Based on In Vivo Computed Tomography Assessment.* Circ Cardiovasc Interv, 2023. **16**(11): p. e013497.

98. Plitman Mayo, R., et al., *Impact of BASILICA on the thrombogenicity potential of valve-in-valve implantations.* J Biomech, 2021. **118**: p. 110309.

99. Tagliari, A.P., et al., *The Use of BASILICA Technique to Prevent Coronary Obstruction in a TAVI-TAVI Procedure.* J Clin Med, 2021. **10**(23).

100. Navarra, E., et al., *Native Aortic Valve Resection Using a Novel Blade-Based Device.* Innovations (Phila), 2024. **19**(2): p. 150-155.